Research Square

Preprints are preliminary reports that have not undergone peer review.
They should not be considered conclusive, used to inform clinical practice,
or referenced by the media as validated information.

Non-additive pressure-load response to edge shaping and cavity closure on an idealised twin-girder bridge deck

Mingjin Lou
Imperial College London https://orcid.org/0009-0008-0532-3948
Yize Zhang
Monash University https://orcid.org/0009-0006-0370-7492
Ze Tao
a1434916588@outlook.com
Changchun University of Science and Technology https://orcid.org/0009-0004-0202-3641

Research Article

Keywords: Bridge-deck aerodynamics, Factorial design, Geometric interactions, Pressure-force decomposition, Unsteady Reynolds-averaged Navier–Stokes simulations

Posted Date: November 12th, 2026

DOI: https://doi.org/10.21203/rs.3.rs-11699516/v1

License: This work is licensed under a Creative Commons Attribution 4.0 International License.
Read Full License

Additional Declarations: The authors declare no competing interests.

Non-additive pressure-load response to edge shaping and cavity closure on an idealised twin-girder bridge deck

Mingjin Lou[1], Yize Zhang[2], Ze Tao[3*]

[1]Faculty of Engineering, Imperial College London, South Kensington Campus, London, SW7 2AZ, United Kingdom.
[2]Faculty of Information Technology, Monash University, Clayton, Victoria, 3800, Australia.
[3]School of Physics, Changchun University of Science and Technology, Changchun, 130022, P.R. China.

*Corresponding author: Ze Tao

Abstract Geometric modifications can reduce wind loads on bluff bridge decks, but their combined effect may differ from the sum of the individual effects because local changes can alter separation and pressure recovery on distant surfaces. We study the interactions between edge shaping and cavity closure on an idealised twin-girder bridge deck using two-dimensional unsteady Reynolds-averaged Navier–Stokes simulations with the k–ω shear-stress-transport model at a depth-based Reynolds number of 1.6×10^7. Two complete 2×2 factorial sets separate main effects from interactions. Surface-pressure integrals give the regional contributions, and the summed pressure forces are checked against the recorded pressure forces. Numerical allowances are reported separately from model error. The streamlined section carries 54% less drag than the bare one, with a numerical allowance of ±1.1 percentage points. The two edges do not act independently. On the closed section with inclined edges, curving one edge saves only about 5% of the drag, but curving both saves 53%, and 81% of that saving comes from their interaction. Almost all of this interaction acts on the trailing outer face. Opening the cavity affects lift in opposite directions for the two edge shapes: it raises lift when the edges are inclined and lowers it when they are curved, through changes in the top and underside pressures. The results show how edge and cavity changes act together and where their pressure contributions arise within the numerical model, although discrepancies in benchmark loads and reattachment limit predictions of physical load reductions.

Keywords: Bridge-deck aerodynamics, Factorial design, Geometric interactions, Pressure-force decomposition, Unsteady Reynolds-averaged Navier–Stokes simulations

List of symbols

$B_0,\ B_i$	Common reference width and physical width of section i [m]
$D,\ D_0$	Common reference depth, taken from Case 1 [m]
U_∞	Free-stream speed [m/s]
$C_d,\ C_l,\ C_m$	Drag, lift and pitching-moment coefficients
C_p	Pressure coefficient
$E_{12},\ 2E_{12}$	Factorial interaction and corresponding difference of slopes
$U,\ U_{\mathrm{loc}}$	Adopted overall and local-contrast numerical allowances
$L/B_0,\ h_w/B_0$	Normalised recirculation length and reversed-flow height
$\xi,\ \xi_w$	Leading-edge coordinate scaled by B_0; wake coordinate scaled by D_0
Re, St	Reynolds and Strouhal numbers
k	Modelled turbulent kinetic energy [m^2/s^2]
$\nu,\ \nu_t$	Molecular and modelled eddy kinematic viscosities [m^2/s]
$\overline{(\cdot)},\ (\cdot)'$	Time mean and RMS fluctuation of a coefficient [-]
$E_1,\ E_2$	Factorial main effects [-]
Co	Maximum Courant number [-]
y^+	Dimensionless wall distance [-]
$u_\tau,\ y_P$	Friction velocity [m/s] and first-cell-centre wall distance [m]
C_{pb}	Base-pressure coefficient [-]
$C_{d,p}$	Pressure-drag coefficient [-]
R_D	Drag reduction relative to Case 1 [%]
$U_{\mathrm{GCI}},\ U_{\Delta t},\ U_s,\ U_w$	Grid, time-step, statistical and window-end numerical allowances [coefficient units]
α	Angle of attack [°; radians in secants]
f_s	Vortex-shedding frequency [Hz]
p	Pressure [Pa]; apparent order in the grid-convergence analysis [-]

1 Introduction

Aerodynamic design of open twin-girder bridge decks aims to reduce wind loads and control vortex-induced vibration. These decks have two edge girders that support a composite slab, leaving an open cavity beneath it. Flow separates at the deck edges, and the shear layers form large recirculation regions around the girders and beneath the slab. This separated flow is associated with high mean drag and strong, coherent vortex shedding [1–3]. Designers add fairings, edge deflectors, skirts or enclosures to modify the flow and improve aerodynamic performance [4–6]. However, bluff-body loads depend on the coupled development of separated shear layers and surface pressure, so a local geometric change can alter forces on distant parts of the same section. Understanding this coupling is important for assessing how individual modifications and their combinations affect the overall wind loads.

Boat-tail shaping reduces the afterbody cross-section towards the base. Low-speed experiments on bodies of revolution measured substantial drag reductions with short boat-tailed afterbodies [7]. For a spanwise-extruded boat-tailed body, three-dimensional large-eddy simulations linked groove-induced separation delay to increased base pressure and reduced drag [8]. These findings led us to examine whether changing one deck edge also changes pressure on the other surfaces. The present factorial comparisons quantify how the response to one geometric change depends on the other features of the section.

The studies of open-deck fairings cited above primarily focus on vortex-induced vibration (VIV), varying one device or parameter at a time and comparing a small number of configurations through wind-tunnel tests or computational fluid dynamics (CFD) [2, 6]. These studies identify effective configurations, but seldom establish how much each fairing component contributes to the mean and fluctuating loads or whether the components act independently. Such independence cannot be assumed: closing the cavity beneath the slab changes the base pressure on which a trailing-edge fairing acts, while a leading-edge fairing changes the separated shear layer and whether it reattaches to the closed underside. Related non-additivity has also been studied for combined excitation. Tesfaye et al. [9] compared the separate and combined effects of sinusoidal motion and gust inputs, linking departures from force superposition to separated shear layers. Their study concerns interactions between inputs to a moving deck. We examine interactions between geometric features on a fixed deck. Deck equipment also limits how far benefits obtained for bare sections can be transferred to equipped decks: barriers can increase drag and alter VIV or flutter responses, depending on their porosity and the section shape [10–15].

Shape effects have been studied more systematically for closed box girders. Zheng et al. [16] developed a Kriging surrogate to predict the flutter speed of a streamlined box girder from four shape parameters, including two that define the position of the edge-fairing tip. Their analysis of variance attributed about 36% of the variance to girder depth, while each of the other parameters and each of their second- and third-order interactions accounted for 2–6%. Aero-structural design frameworks combine deck-shape design with structural requirements to minimise material volume, section weight or construction cost under flutter, buffeting or VIV constraints [17–20]. Machine-learning surrogates have also been used to predict the static instability of slotted box girders [21] and to optimise fairings on open twin-girder decks for VIV control [22]. These approaches focus on continuous shape parameterisation and aero-structural optimisation. In the cited flutter-speed analysis, the effects are evaluated using a fitted surrogate, while the present study calculates contrasts directly from a complete set of discrete flow solutions for each two-factor comparison. Installation and maintenance requirements also constrain the selection of appendages [23]; an index based on added exterior skin is used here only for auxiliary screening.

Two-dimensional unsteady Reynolds-averaged Navier–Stokes (URANS) simulations with the k–ω shear-stress-transport (SST) model [24] offer an economical way to compare bridge-deck configurations, although their accuracy depends on geometry, Reynolds number and flow regime [25, 26]. Haque et al. [27] compared URANS predictions with experiments for a pentagonal deck and related changes in overall loads to surface pressure and separated-flow patterns. The discrepancies they reported in strongly separated regions and pressure fluctuations support checking local flow features alongside integrated forces when assessing model accuracy. For the Benchmark on the Aerodynamics of a Rectangular 5:1 Cylinder (BARC), Chiarini and Quadrio [28] studied how small leading-edge corner roundings affect mean separation, reattachment and velocity profiles. Their direct numerical simulations used a depth-based Reynolds number of 3000. The reported corner sensitivity needs to be interpreted with those numerical and flow conditions in mind. More recently, Li et al. [29] combined wind-tunnel measurements and CFD to update predictions of mean bridge-deck force coefficients and examine blockage effects. Their approach calibrates predictions against measurements, while the present study separates specified geometric effects within one numerical model without matched experimental calibration. Spanwise correlation and three-dimensional wake dynamics require three-dimensional modelling [30]. Near-wall mesh quality is also critical: a few moderately skewed cells near the leading edge can change drag, lift fluctuations and the Strouhal number by more than changing the turbulence model [31]. When different geometries are meshed separately, differences in mesh quality can be mistaken for geometric effects. The skin-friction contribution to drag also requires attention, as neglecting wall shear stress has been found to underestimate the drag of a box deck by up to about 15% [32].

We study how leading-edge shape, trailing-edge shape and cavity opening produce non-additive pressure loads on an idealised twin-girder bridge deck ($B_0 = 30$ m, $D = 9.4$ m). Two complete 2×2 factorial designs share two configurations, comprising six distinct geometries. Set A independently varies the shapes of the leading and trailing edges on a closed cross-section. Set B compares the open and closed states of the cavity, using configurations with either inclined or curved edges on both sides. Comparisons among the four configurations in each design separate main effects from interactions and calculate deviations from additivity. The contribution of each region to the load variation is obtained by integrating surface pressure, and the summed regional pressure forces are checked against the independently saved pressure-force records. Each effect is compared with its estimated numerical uncertainty to determine whether it is resolved; we also check whether different assumptions about error correlation change which effects are resolved. This attribution applies only to the tested configuration sets within the numerical model used.

By comparing the results with data from the Great Belt and BARC benchmarks, it is possible to determine which physical quantities are supported by the model and which still show discrepancies with the measured results [33–35]. Additional cases with barriers and varying angles of attack examine the scope of the computed aerodynamic response. An index based on added exterior skin provides an auxiliary measure of the material demand of the tested shapes. This study focuses on aerodynamic loads on fixed deck sections. For a specified set of URANS configurations, this study makes the following three contributions:

1. A comprehensive quantitative comparison of the four configurations shows the non-additive effects of leading-edge and trailing-edge geometries on drag response, as well as the reversal phenomenon in cavity-opening lift response between inclined and curved edges.
2. Regional pressure–force integrals have been used to determine the interaction between edge shaping and drag on the outer surface of the trailing edge, and to analyse the pressure variations on the top and bottom surfaces that give rise to the lift response at the cavity opening, which are consistent with the recorded force values.
3. Segmented numerical tolerance and dependency-sensitivity checks distinguished the analytically derived interactions from those smaller effects whose interpretation depends on error correlations, whilst benchmark comparisons assessed the physical applicability of the model separately.

2 Methods

2.1 Deck geometries

The study compares five configurations of an idealised twin-girder deck. Case 1 (*Baseline*) is a bare twin-girder deck with open cavities, a width of $B_0 = 30$ m between the deck edges and an overall depth of $D = 9.4$ m (Fig. 1). Case 2 (*Encase*) encloses each beam within a trapezoidal fairing and retains the openings between the beams. Case 3 (*Enclose*) encloses the bottom and sides of the space between the beams; the enclosed airspace remains a cavity and is excluded from the computational mesh. Case 4 (*Deflect*) retains the open bottom and adds curved deflectors at both deck edges, with lips extending 1.3 m above the deck, together with a V-shaped fin beneath each girder. Case 4 has a maximum projected height of 12.3 m. Case 5 (*Streamline*) has a closed bottom and curved fairings at both edges. Its projected height is 9.4 m, and its outer-envelope width is $B_5 = 33.5$ m. The physical widths B_i are 30 m for Cases 1–3 and 33.1 m for Case 4. All configurations, including the variants, use $B_0 = 30$ m to normalise flow lengths. B_i gives the actual width of each section and is not the force reference length. Case 5 has a fore–aft symmetric outer contour. The five main configurations use the same main girders and a deck slab with a nominal thickness of 1.4 m. The rounded-corner variant described below differs at the deck edges. The deck is relatively deep, with a common width-to-depth ratio of $B_0/D = 3.19$.

Seven additional sections, listed in Table 2 and shown in Fig. 2, are used to separate the contributions of individual geometric features. The positions of the modified features are specified relative to the main girders and deck of the corresponding parent section. Set A compares specified edge shapes, including their changes in outer-envelope width. GD_ROUND is formed by rounding the convex corners of the Case 3 outer contour inward with a radius of 1 m, including the deck-edge corners. This modification changes both the local parent contour and the fairing junctions.

2.2 Factorial design

Two 2×2 factorial sets are constructed from these sections. Set A comprises the four closed sections Case 3, GA_LE, GA_TE and Case 5, with the leading-edge and trailing-edge shapes varied independently between an inclined plate and a curved fairing. Set B comprises Case 3, GB_OPEN_S, GB_OPEN and Case 5, and combines two cavity states (open or closed) with two edge shapes (inclined plates or curved fairings at both edges). For a

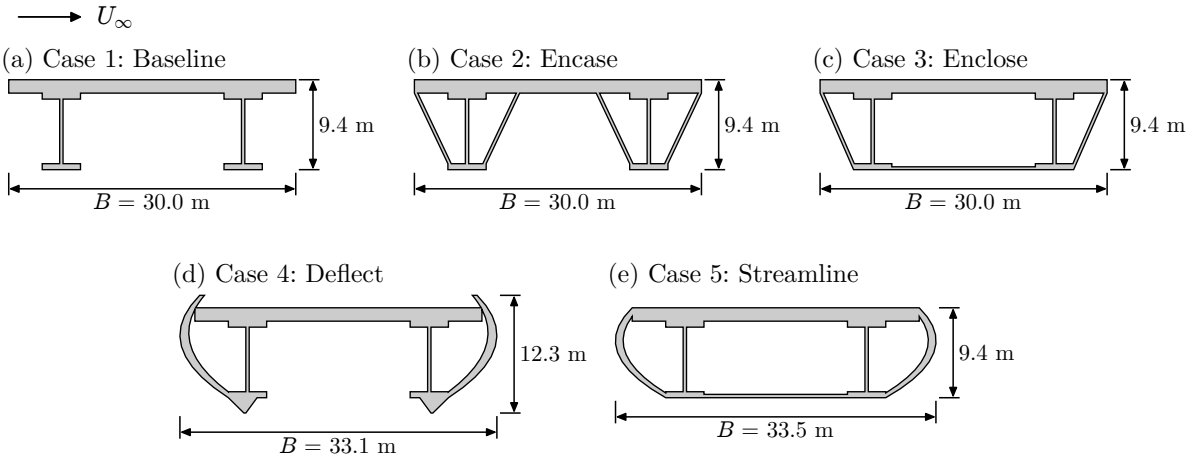


Fig. 1 The five deck sections, drawn at a common scale and aligned on the deck top. Grey: solid section; white enclosed regions: voids, not meshed. The labels B denote the physical widths B_i; the maximum projected heights are also marked; the arrow gives the positive streamwise direction. (**a**) Case 1, bare section; (**b**) Case 2, encased girders; (**c**) Case 3, closed cavity; (**d**) Case 4, edge deflectors; (**e**) Case 5, closed bottom with curved edge fairings

Table 2 Additional sections that isolate individual geometric features. LE: leading (windward) edge; TE: trailing (leeward) edge. In each name the prefix gives the group (GA and GB, factorial sets A and B; GC, Case 4 with one appendage removed; GD, the rounded variant of Case 3) and the suffix gives the change (LE or TE, the edge that is curved; OPEN, open central cavity, with _S for the inclined-plate edges of Case 3; NOLIP and NOFIN, lips or fins removed; ROUND, rounded corners)

Section	Geometry	Purpose
GA_LE	Closed section; LE curved as in Case 5, TE inclined plate as in Case 3	Factorial set A (LE × TE)
GA_TE	Closed section; LE inclined plate, TE curved	Factorial set A
GB_OPEN_S	Case 3 outer contour without bottom plate; central cavity open ($\|x\| \le 7.5$ m, up to 1.4 m below the deck surface)	Factorial set B (closure × edge shape)
GB_OPEN	Case 5 outer contour with the same open cavity	Factorial set B
GC_NOLIP	Case 4 without the deflector lips above the deck (cut at the deck surface)	Role of the deflector lips
GC_NOFIN	Case 4 without the bottom fins (cut at the bottom of the main girders)	Role of the fins
GD_ROUND	Case 3 outer convex corners rounded inward, including deck edges; $r = 1$ m ($\approx 0.11D$)	One specified rounding variant versus full edge shaping

response y (the mean coefficients C_d, C_l or C_m, the root-mean-square (RMS) lift coefficient C_l', or the Strouhal number St), each factor has two levels, coded − and +. The main effects E_1 and E_2 and the interaction E_{12} are defined as

$$\begin{aligned} E_1 &= \tfrac{1}{2}\left[(y_{+-} - y_{--}) + (y_{++} - y_{-+})\right], \\ E_2 &= \tfrac{1}{2}\left[(y_{-+} - y_{--}) + (y_{++} - y_{+-})\right], \\ E_{12} &= \tfrac{1}{2}\left[(y_{++} - y_{-+}) - (y_{+-} - y_{--})\right], \end{aligned} \tag{1}$$

where the first subscript denotes the level of the first factor and the second subscript denotes the level of the second factor. Each effect on C_d is evaluated for the pressure and viscous contributions to drag. For an unreplicated two-level factorial design, the squared-effect share $E^2/\sum E^2$ equals the corresponding share of the total sum of squares within the selected four-combination design. The comparison with the variance-based proportions reported by Zheng et al. [16] for closed box girders is qualitative because the two studies use different parameter ranges and study designs. These proportions do not constitute a test of statistical significance.

This total prediction is formulated as a linear combination of three separate responses:

$$y_{\text{add}} = y_{+-} + y_{-+} - y_{--}, \qquad y_{++} - y_{\text{add}} = 2E_{12}. \tag{2}$$

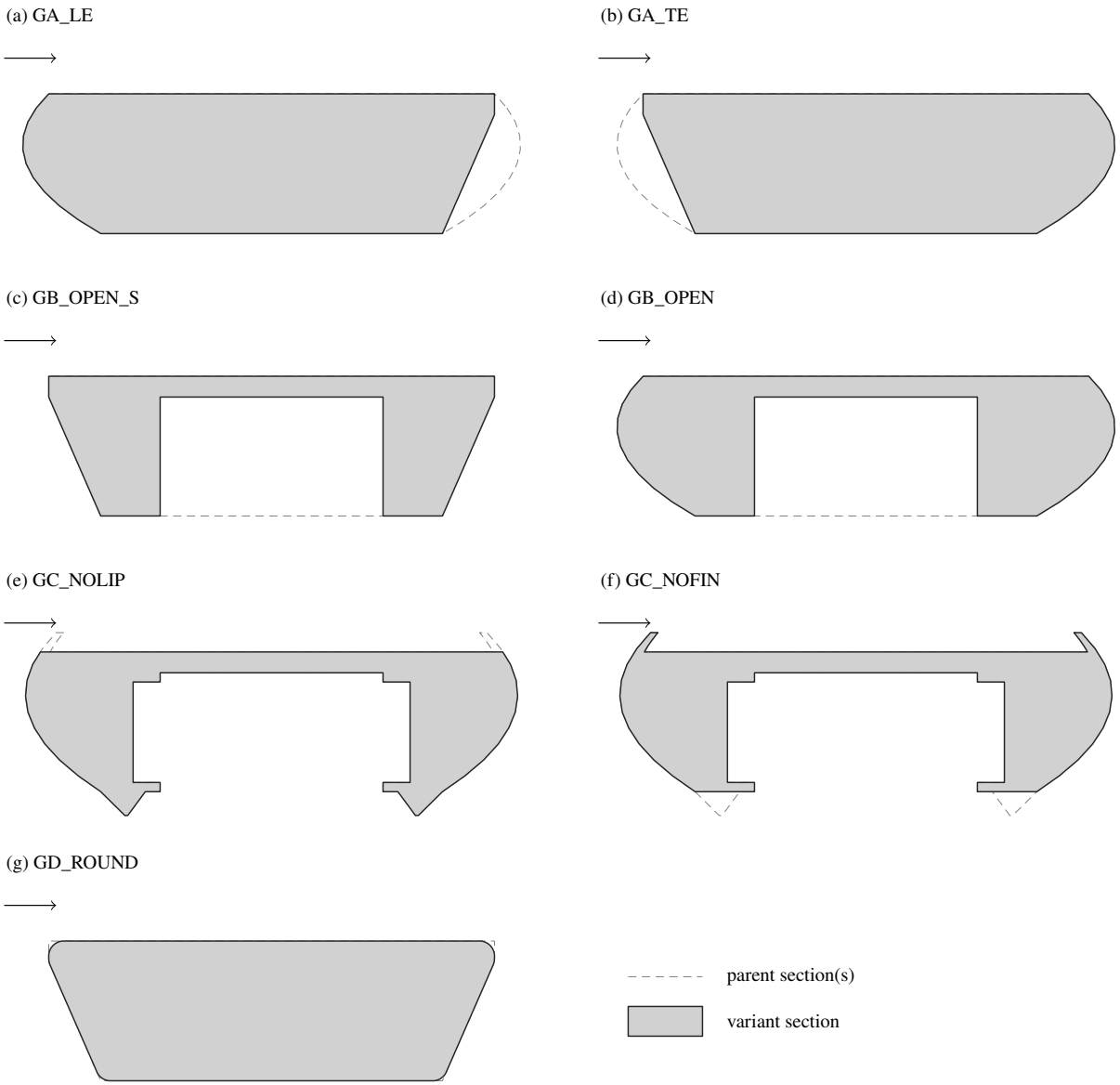


Fig. 2 Variant sections of Table 2 (solid) and the sections they are derived from (dashed), drawn at a common scale; the arrow gives the positive streamwise direction. (**a**,**b**) Factorial set A; (**c**,**d**) factorial set B; (**e**,**f**) Case 4 without its deflector lips or its bottom fins; (**g**) Case 3 with rounded corners

This prediction is an algebraic combination of three computed responses. The difference between the fourth computed response and the additive prediction is identical to $2E_{12}$, so it uses the same numerical allowance based on all four responses and the same sensitivity analysis for error correlation.

Three types of comparison are distinguished throughout the study. The overall computed drag reduction is evaluated relative to the bare section, Case 1. Set A uses the closed section with inclined edges, Case 3, as its reference and separates the change from Case 3 to Case 5 into contributions from the individual edge changes and their interaction. Set B evaluates the effect of cavity opening for each edge shape. The 54% drag reduction relative to the bare section, the 81% non-additive share of the drag reduction in set A, and the interaction share of the sum of squared factorial effects thus use different denominators.

We also examine load changes along the sequence Case 1 → Case 2 → Case 3 → GA_LE → Case 5. Girder encasement, cavity closure, leading-edge shaping and trailing-edge shaping are added one at a time in this order. If the modifications interact, the load change attributed to each modification depends on which changes have already been made. The factorial comparisons measure these interactions within the tested combinations.

2.3 Traffic barriers and angle of attack

For Cases 1, 4 and 5, we test solid barriers and barriers with a 50% open-area ratio. Both barrier types extend 1.0 m above the deck. We also simulate the same three sections without barriers at angles of attack of $-10°$, $-5°$, $0°$, $+5°$

and +10°. The two-dimensional representation of the porous barriers consists of two rails and excludes posts. For Case 4, the barriers are positioned inboard of the deflector lips, which rise 1.3 m above the deck, so the computed response includes sheltering by the lips. Forces on the barriers and the deck are recorded separately. All barrier simulations use the finer of the two local refinement levels examined. The angle-of-attack series uses a rotated inflow direction with the geometry held fixed and `freestream` boundary conditions on the outer boundaries.

These simulations examine how the bare-section findings change under the tested barrier and incidence conditions. Details of the geometry, time-step matching and local sensitivity budget are given in Appendix G.1. For the barrier comparisons, this budget does not bound residual global-grid error in the difference between simulations with and without barriers, or model error.

2.4 Governing equations and turbulence model

Air is treated as an incompressible Newtonian fluid. At $U_\infty = 25$ m/s, the Mach number is 0.07. The flow is described by the unsteady Reynolds-averaged Navier–Stokes (URANS) equations:

$$\frac{\partial \bar{u}_i}{\partial x_i} = 0, \qquad \rho\left(\frac{\partial \bar{u}_i}{\partial t} + \bar{u}_j\frac{\partial \bar{u}_i}{\partial x_j}\right) = -\frac{\partial \bar{p}}{\partial x_i} + \frac{\partial}{\partial x_j}\left[\mu\left(\frac{\partial \bar{u}_i}{\partial x_j} + \frac{\partial \bar{u}_j}{\partial x_i}\right) - \rho\,\overline{u_i' u_j'}\right]. \tag{3}$$

Here, ρ and μ are the density and dynamic viscosity. The Boussinesq hypothesis relates the Reynolds stresses to the mean strain rate:

$$-\rho\,\overline{u_i' u_j'} = \mu_t\left(\frac{\partial \bar{u}_i}{\partial x_j} + \frac{\partial \bar{u}_j}{\partial x_i}\right) - \frac{2}{3}\rho k\,\delta_{ij}. \tag{4}$$

The eddy viscosity $\mu_t = \rho\nu_t$ and turbulent kinetic energy k are obtained from the 2003 form of Menter's k–ω SST model [24, 36], implemented in OpenFOAM as `kOmegaSST`. The model solves transport equations for k and the specific dissipation rate ω:

$$\frac{\partial(\rho k)}{\partial t} + \frac{\partial(\rho \bar{u}_j k)}{\partial x_j} = \tilde{P}_k - \beta^*\rho\omega k + \frac{\partial}{\partial x_j}\left[(\mu + \sigma_k\mu_t)\frac{\partial k}{\partial x_j}\right] + S_k, \tag{5}$$

$$\begin{aligned}\frac{\partial(\rho\omega)}{\partial t} + \frac{\partial(\rho \bar{u}_j \omega)}{\partial x_j} &= \frac{\gamma\rho}{\mu_t}\tilde{P}_k - \beta\rho\omega^2 + \frac{\partial}{\partial x_j}\left[(\mu + \sigma_\omega\mu_t)\frac{\partial \omega}{\partial x_j}\right] \\ &\quad + 2(1 - F_1)\frac{\rho\,\sigma_{\omega 2}}{\omega}\frac{\partial k}{\partial x_j}\frac{\partial \omega}{\partial x_j} + S_\omega.\end{aligned} \tag{6}$$

The mean strain-rate magnitude is $S = (2\bar{S}_{ij}\bar{S}_{ij})^{1/2}$, where $\bar{S}_{ij}$ is the mean strain-rate tensor. The production of turbulent kinetic energy is $P_k = \mu_t S^2$. Its limited form, $\tilde{P}_k = \min(P_k,\, 10\beta^*\rho k\omega)$, prevents the build-up of turbulence in stagnation regions. In the ω equation, the production term is $\gamma\rho\tilde{P}_k/\mu_t$, which reduces to $\gamma\rho S^2$ when the limiter is inactive. The penultimate term in that equation is the cross-diffusion term obtained by writing the k–ε model in k–ω form.

The blending function F_1 is defined as

$$\begin{aligned}F_1 &= \tanh\left(\arg_1^4\right), \qquad \arg_1 = \min\left[\max\left(\frac{\sqrt{k}}{\beta^*\omega d}, \frac{500\nu}{d^2\omega}\right), \frac{4\rho\sigma_{\omega 2}k}{CD_{k\omega}\,d^2}\right], \\ CD_{k\omega} &= \max\left(\frac{2\rho\sigma_{\omega 2}}{\omega}\frac{\partial k}{\partial x_j}\frac{\partial \omega}{\partial x_j},\; 10^{-10}\right),\end{aligned} \tag{7}$$

where d is the distance to the nearest wall. F_1 equals one near walls and approaches zero away from them. Each model coefficient ϕ is blended as $\phi = F_1\phi_1 + (1 - F_1)\phi_2$. This gives the k–ω model in the inner part of the boundary layer and the k–ε model in the free stream and separated shear layers. The standard constants are used: $\beta^* = 0.09$, $\sigma_{k1} = 0.85$, $\sigma_{k2} = 1$, $\sigma_{\omega 1} = 0.5$, $\sigma_{\omega 2} = 0.856$, $\beta_1 = 0.075$, $\beta_2 = 0.0828$, $\gamma_1 = 5/9$ and $\gamma_2 = 0.44$.

The model also limits the eddy viscosity in adverse pressure gradients:

$$\nu_t = \frac{a_1 k}{\max(a_1\omega,\, S\,F_2)}, \qquad F_2 = \tanh\left(\arg_2^2\right), \qquad \arg_2 = \max\left(\frac{2\sqrt{k}}{\beta^*\omega d}, \frac{500\nu}{d^2\omega}\right). \tag{8}$$

Here, $a_1 = 0.31$, and the second blending function F_2 confines the limiter to boundary layers. This limiter is the main reason for the model's wide use in separated flow around bluff sections [25, 37]. URANS resolves the periodic vortex shedding that dominates the unsteady loads, while turbulent fluctuations are modelled [38].

In two-equation models, free-stream turbulence can decay between the inlet and the body [39]. Sustaining terms are added through `decayControl` to prevent this decay: $S_k = \beta^* \rho\, \omega_\infty k_\infty$ and $S_\omega = \beta \rho\, \omega_\infty^2$. In the free stream, where production and diffusion vanish, these terms balance destruction and hold k and ω at their inflow values, k_∞ and ω_∞ (Section 2.7). Near the walls, the first cell centres lie mostly within $30 \le y^+ \le 300$, where $y^+ = u_\tau y_P / \nu$ is the dimensionless wall distance, u_τ is the friction velocity and y_P is the wall distance of the first cell centre. Wall functions supply ν_t, k and ω (Section 2.7).

2.5 Aerodynamic coefficients and flow quantities

Drag, lift and pitching moment over the simulated 1 m span are normalised by the free-stream dynamic pressure, $q_\infty = \frac{1}{2}\rho U_\infty^2$:

$$C_d = \frac{F_D}{q_\infty A_{\mathrm{ref}}}, \qquad C_l = \frac{F_L}{q_\infty A_{\mathrm{ref}}}, \qquad C_m = \frac{M_y}{q_\infty A_{\mathrm{ref}} L_{\mathrm{ref}}}. \tag{9}$$

The drag force is parallel to the inflow and the lift force is normal to it, with $F_D = F_x \cos\alpha + F_z \sin\alpha$ and $F_L = -F_x \sin\alpha + F_z \cos\alpha$. The geometric coordinates x and z remain fixed, and M_y is taken about the positive spanwise axis. At $\alpha = 0$, $F_D = F_x$ and $F_L = F_z$. All sections use the same reference area, $A_{\mathrm{ref}} = 9.4$ m^2, and reference length, $L_{\mathrm{ref}} = 9.4$ m. The area is the depth D of Case 1 multiplied by the 1 m span. With these common references, the coefficients compare forces directly.

The moment reference point lies on the centre line, 1.92 m below the deck surface and 7.48 m above the bottom of the main girders. Its position relative to the girders and deck is the same for every section, and positive moment is nose up. Coefficients based on each section's own projected height are listed in Appendix B for comparison of the sections as bluff bodies of different sizes. For the reported aerodynamic coefficients, overbars denote time means and primes denote RMS fluctuations, such as C_l'. For a coefficient $C(t)$ over the accepted window $[t_1, t_2]$,

$$\overline{C} = \frac{1}{t_2 - t_1} \int_{t_1}^{t_2} C(t)\, \mathrm{d}t, \qquad C' = \left[\frac{1}{t_2 - t_1} \int_{t_1}^{t_2} \left(C(t) - \overline{C}\right)^2 \mathrm{d}t \right]^{1/2}. \tag{10}$$

The same definitions apply to the pressure coefficient, so C_p' denotes its RMS fluctuation.

The Reynolds and Strouhal numbers are defined as

$$Re = \frac{U_\infty D}{\nu}, \qquad St = \frac{f_s D}{U_\infty}. \tag{11}$$

Here, $Re = 1.6 \times 10^7$ at $U_\infty = 25$ m/s and $\nu = 1.46 \times 10^{-5}$ m^2/s. The shedding frequency f_s is calculated as the inverse of the mean interval between retained upward crossings of the lift signal. For N_s samples in the accepted window, the signal is first centred on its arithmetic mean. A centred moving average with a half-width of $\lfloor N_s/4000 \rfloor$ samples is applied when this half-width exceeds one sample. The averaging window is shortened at the record endpoints. Each crossing is assigned the time of the first non-negative sample. Starting with the first crossing, a subsequent candidate is retained only if it occurs more than half the median candidate interval after the last retained crossing. The resulting frequency is checked against the Welch spectral peak of C_l [40].

Drag is split into pressure and viscous contributions. Pressure drag is partitioned by surface region. The baseline breakdown separates the outer windward faces, outer leeward faces and cavity walls, while the factorial analysis uses the five-region partition defined in Section 4.3.1. The surface pressure coefficient is $C_p = (p - p_\infty)/q_\infty$, and the base pressure coefficient C_{pb} is the mean pressure coefficient over the outer leeward faces, weighted by their projected height and referenced to the outlet pressure. Form drag is closely related to the base-pressure deficit [41].

The recirculation length L is the streamwise extent of the region with $\overline{U}_x < 0$ downstream of the section in the time-averaged flow field. For all proposed sections and their variants, L and the wake height h_w are normalised by $B_0 = 30$ m. The near-wall streamwise coordinate is $\xi = (x - x_{\mathrm{LE},i})/B_0$, measured from the leading edge of each section. In the flow-panel annotations, B in L/B or h_w/B denotes B_0, rather than the physical width B_i. The validation geometries use their own stated benchmark widths and normalisations.

2.6 Numerical method

All simulations use OpenFOAM v2506 [42] and the PIMPLE algorithm in `pimpleFoam`. PIMPLE combines the pressure-implicit with splitting of operators (PISO) and semi-implicit method for pressure-linked equations (SIMPLE) algorithms. Each time step uses three outer corrector iterations, two pressure correctors and one non-orthogonal corrector, without under-relaxation. Time derivatives use the second-order backward scheme. The convection schemes are `bounded Gauss linearUpwind` for velocity and `bounded Gauss limitedLinear 1`

for k and ω. Gradients use `cellLimited Gauss linear 1`, and Laplacian terms use `Gauss linear limited corrected 0.5`.

The pressure equation is solved with the geometric agglomerated algebraic multigrid (GAMG) solver, using an absolute tolerance of 10^{-7} and a relative tolerance of 0.01. The relative tolerance is set to zero for the final pressure solve. The velocity, k and ω equations use `smoothSolver` with a symmetric Gauss–Seidel smoother, an absolute tolerance of 10^{-8} and a relative tolerance of 0.05. These tolerances specify the linear-solver stopping criteria; Appendix A shows the achieved residuals.

The time step is adjusted to keep the maximum Courant number (Co) at 2, subject to $\Delta t \leq 0.01$ s. This gives time steps of approximately 0.85–1.1 ms. Case 5, its angle-of-attack series and the seven variant sections in Table 2 use a maximum Courant number of 1 because Case 5 is sensitive to the time step (Section 3.1.3). For Case 5, this gives $\Delta t \approx 0.43$ ms. The factorial sets and comparisons with the variant sections use the maximum-Co 1 runs of Cases 3, 4 and 5, so all sections in these comparisons share the same time-step control. Appendix A summarises these settings.

URANS runs normally start from a steady SIMPLE solution. The reported loads use only the unsteady results. Runs that require uniform-field initialisation and the associated checks are described in Appendix G.2. The default simulation duration is 160 s; exceptions and their accepted analysis windows are listed in Appendix A.

2.7 Domain, boundary conditions and inflow

The computational domain extends from $x = -200$ m to 400 m and from $z = -200$ m to 200 m. Its boundaries lie approximately $6.2B_0$ upstream of the leading edge, $12.8B_0$ downstream of the trailing edge and $20D$ above and below the deck. At zero angle of attack, the blockage ratio based on projected height is 2.35% for Cases 1–3 and 5 and 3.08% for Case 4. Only the former satisfy the 3% guideline of Franke et al. [43]. The mesh has one cell in the spanwise direction, with `empty` conditions on the front and back boundaries (Fig. 3(a)). The boundary conditions are listed in Appendix G.3.

The inflow is uniform, with $U_\infty = 25$ m/s, a turbulence intensity of 5% and a length scale of $\ell = 0.66$ m ($0.07D$). These values give $k = 2.34$ m^2/s^2 and $\omega = 4.23$ s^{-1}, which the sustaining terms maintain from the inlet to the deck. The deck is a smooth no-slip wall, with wall functions for ν_t, k and ω [44]. The top and bottom boundaries are slip walls, and the outlet uses zero-gradient conditions for velocity and turbulence quantities.

For the angle-of-attack series, the inflow direction is rotated while the geometry remains fixed. All four outer boundaries use the inlet `freestream` conditions with the rotated velocity. This series includes its own $\alpha = 0°$ run. The effect of changing the outer boundary conditions is reported in Section 3.1.5.

2.8 Meshes

The meshes are generated with `snappyHexMesh` from a `blockMesh` background grid. The central block, spanning $-40 \leq x \leq 140$ m and $-30 \leq z \leq 40$ m, contains square cells of size Δ_0. Cell sizes in the outer blocks increase by a factor of 1.10 per cell. The deck surface and its feature edges are refined to level 5, corresponding to $\Delta_0/32$. A box around the section, spanning $-20 \leq x \leq 24$ m and $-4 \leq z \leq 14$ m, is refined to level 3. A wake box extending about $3B_0$ downstream of the section is refined to level 2. Three cells separate successive refinement levels.

Eight prism layers are added along the deck surface. The first layer is 8 mm thick, the growth ratio is 1.15 and the total thickness is approximately 0.11 m. Layers are not grown across edges sharper than 130°. The three-dimensional mesh is then reduced to the $y = 0$ plane and extruded through a 1 m span with one cell in the spanwise direction.

Cases 1, 3 and 5 each use three grids: M1 with $\Delta_0 = \sqrt{2}$ m, M2 with $\Delta_0 = 1$ m and M3 with $\Delta_0 = 1/\sqrt{2}$ m. All three grids use the same refinement levels and prism-layer dimensions to keep the near-wall treatment comparable. Near-wall sensitivity is tested separately in Section 3.1.2. Cases 2 and 4 use M2 without a separate three-grid study. The production results use M2, with a surface cell size of 0.031 m. Fig. 3 shows the M2 grids and prism layers for Cases 1 and 5.

The grids are checked for two-dimensional topology and acceptance by `checkMesh`, with maximum non-orthogonality below 65° and skewness below 4. Wall coverage is below the target in Case 2 (97.7%) and Case 4 (97.3%). GC_NOLIP also has two short gaps along straight segments. Appendix G.3 records these exceptions, mesh regeneration checks, cell counts and end-of-run y^+ values.

2.9 Sampling and uncertainty

The default analysis window is 40–160 s and contains at least 30 shedding cycles. The Case 5 angle-of-attack series and the seven variant sections are run to 120 s, with a standard analysis window of 40–120 s containing at least 28 cycles. If the cycle means still drift after 40 s, the simulation is extended or a longer initial interval is

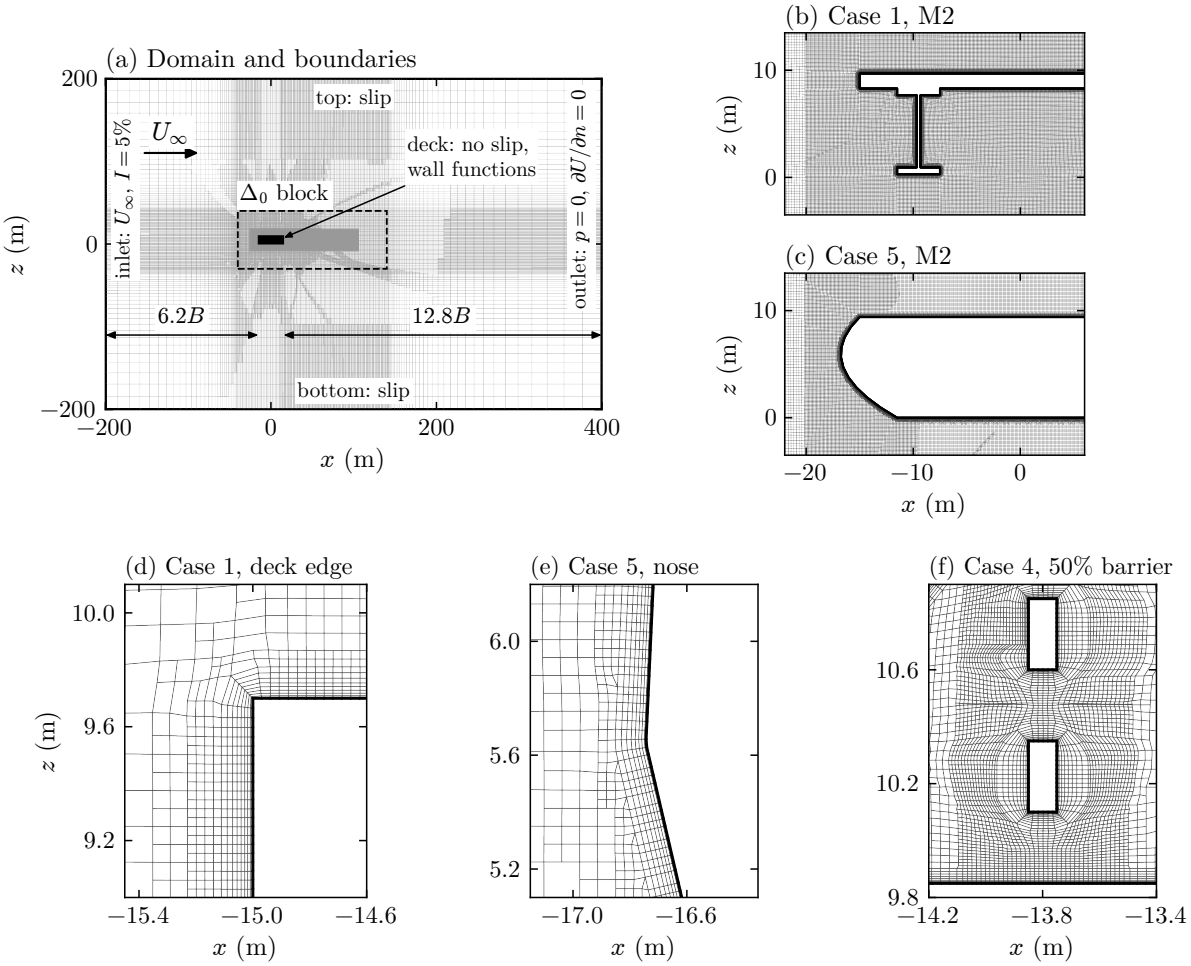


Fig. 3 Domain and grids. (a) Domain and boundary conditions (Appendix G.3), with the Case 1 M2 grid in the background; dashed: central block with cells of size Δ_0. (b, c) M2 around the windward half of Cases 1 and 5. (d, e) Prism layers at the windward deck edge of Case 1 and at the nose of Case 5. (f) Grid around the 50%-porous barrier of Case 4 at the finer refinement level used for all barrier runs (Section 2.3). In panel (a), B denotes the common width B_0 = 30 m

discarded. Appendix A lists the exceptions and their accepted windows. The shortest accepted windows contain 25 cycles for Case 4 at $\alpha = -10°$ and 23 cycles for GC_NOLIP.

Because the time step varies, all means and RMS values are calculated by time integration using the trapezoidal rule. This also applies to the block means. The statistical window is divided into four blocks, each containing the same whole number of lift cycles. The target is agreement within 1% among the block means of C_d and C_l. Cases that do not meet this target are treated as described below. Section 3.1.4 shows the sensitivity to window length.

For a mean quantity, the statistical uncertainty is $U_s = t_{0.975,3}\, s_b/\sqrt{4}$, where s_b is the standard deviation of the four block means. Two variant results require alternative estimates because a small mean or slow monotonic drift causes the block means to differ. For C_l of GD_ROUND, the difference between the two halves of the window is used, giving $U_s = 0.010$ at $C_l = -0.26$. For C_m of GB_OPEN_S, the range of the block means is used, giving $U_s = 0.0098$. These estimates are taken as conservative allowances for the two cases.

An analysis window need not contain a whole number of cycles, so its mean can depend on the start and end times. The allowance for this end effect, U_w, is the absolute difference between the mean over the full window and the mean over the complete lift cycles within it. For all reported budgets, the mean-crossing detector uses the same local averaging as the block statistics. The averaging window is shortened at the record ends, without padding. For the main and variant windows, the largest U_w is 0.011, for C_l of Case 4 over 60–120 s. The incidence and barrier records are assessed separately over their stated windows.

Spatial discretisation uncertainty is estimated from the M1, M2 and M3 solutions for Cases 1, 3 and 5 using the grid convergence index (GCI) procedure of Celik et al. [45]. For a two-dimensional grid with N_k cells, the representative cell size is $h_k = (A_{\mathrm{dom}}/N_k)^{1/2}$. The index $k = 1$ denotes the finest grid, M3; $k = 2$ denotes M2; and $k = 3$ denotes M1. The refinement ratios are $r_{21} = h_2/h_1$ and $r_{32} = h_3/h_2$. Across the three sections, r_{21} ranges

from 1.37 to 1.38 and r_{32} from 1.35 to 1.36. The apparent order p is calculated from

$$p = \frac{1}{\ln r_{21}} \left| \ln \left| \frac{\varepsilon_{32}}{\varepsilon_{21}} \right| + q(p) \right|, \qquad q(p) = \ln \frac{r_{21}^{p} - s}{r_{32}^{p} - s}, \qquad s = \operatorname{sign} \frac{\varepsilon_{32}}{\varepsilon_{21}}, \tag{12}$$

where $\varepsilon_{21} = \phi_2 - \phi_1$ and $\varepsilon_{32} = \phi_3 - \phi_2$. The fine-grid GCI is

$$\mathrm{GCI}^{21} = \frac{1.25\, e_a^{21}}{r_{21}^{p} - 1}, \qquad e_a^{21} = \left| \frac{\phi_1 - \phi_2}{\phi_1} \right|. \tag{13}$$

The ratio $R = \varepsilon_{21}/\varepsilon_{32}$ classifies the sequence as monotonic for $0 < R < 1$, oscillatory for $R < 0$ or divergent for $R > 1$. For an oscillatory or divergent sequence, the largest difference among the three solutions is used as the grid allowance. The production results use M2, so their discretisation allowance is $U_{\mathrm{GCI}} = 1.25\,|\phi_{\mathrm{ext}}^{21} - \phi_2|$, where $\phi_{\mathrm{ext}}^{21} = (r_{21}^{p}\phi_1 - \phi_2)/(r_{21}^{p} - 1)$. If the apparent order exceeds the formal order of the schemes, p is set to 2.

Cases 2 and 4 are computed only on M2. As bluff sections, they are assigned the larger relative grid uncertainty of Cases 1 and 3 for the same quantity. Case 5 is excluded from this transfer because its flow is largely attached and its small mean lift gives relative uncertainties that are unrepresentative of the bluff sections. The seven variant sections also use M2 only and follow the same rule for grid uncertainty. Their time-step uncertainty is taken as the larger relative value from Cases 3 and 5.

For each section value, the numerical allowance is $U = (U_{\mathrm{GCI}}^2 + U_{\Delta t}^2 + U_s^2 + U_w^2)^{1/2}$, where $U_{\Delta t}$ is the time-step contribution described in Section 3.1.3. The window-end term U_w is included for mean coefficients; no separate U_w is assigned to C_l' or St. The variant-section budgets use transferred relative grid and time-step contributions as engineering allowances. The large transferred allowance for C_l' is retained even when it exceeds the value itself. These combined allowances are not calibrated confidence intervals and exclude turbulence-model and two-dimensional modelling errors.

The three-grid studies use a maximum Courant number of 2. Applying their spatial contribution to production results at a maximum Courant number of 1 assumes that grid and time-step effects can be separated. This assumption has not been tested with a new three-grid series at maximum Co 1. Changes in near-wall treatment, inflow and turbulence model are reported separately from the four-component allowance U.

For an effect $E = \sum_i w_i \phi_i$, independent section errors give $U_E = (\sum_i w_i^2 U_i^2)^{1/2}$. The factorial effects in Eq. (1) have weights $w_i = \pm\frac{1}{2}$. Error correlation can increase or decrease this scale, depending on the signs of the weights and covariances. Because the covariances are unavailable, a dependence sensitivity check also uses $U_{E,\mathrm{dep}} = \sum_i |w_i| U_i$, which becomes $\frac{1}{2}\sum_i U_i$ for the factorial effects. This is the largest linear-combination scale allowed by the same marginal allowances; it does not bound unmodelled physical error. The factorial results distinguish effects that exceed this dependence scale from those that exceed only U_E. Other paired changes use independent propagation unless stated otherwise. The percentages assigned to interactions are point estimates and carry no confidence statement.

For the drag reduction from the bare to the streamlined section, $R_D = 100(1 - C_{d,5}/C_{d,1})$, first-order propagation with independent errors gives an allowance of 1.065 percentage points. Replacing the root-sum-square combination with the sum of the absolute weighted allowances gives a dependence sensitivity scale of 1.301 percentage points. Neither scale includes model error.

3 Numerical verification and benchmark comparisons

Verification assesses numerical error, while benchmark comparisons assess agreement with measurements and published results [46, 47]. Following Álvarez and Nieto [30], we examine the grid, near-wall resolution, time step and statistical window in turn (Sections 3.1.1–3.1.4). Section 3.1.5 examines sensitivity to the inflow, turbulence model and far-field conditions. These tests vary the set-up defined in Section 2. Section 3.2 then compares the results for two girders of the Great Belt East Bridge and the BARC rectangular cylinder with benchmark data.

3.1 Verification

3.1.1 Grid convergence

Table 3 lists the M1, M2 and M3 solutions for Cases 1, 3 and 5, together with the apparent order and the grid uncertainty assigned to each M2 value using the procedure in Section 2.9. The ranking of the three sections remains the same on all three grids for every quantity. Mean drag and moment converge most consistently: U_{GCI} is 0.6% for C_d and 0.8% for C_m in Case 1, 3.6% for C_d and 0.3% for C_m in Case 3, and 2.2% for C_d and 2.8% for

C_m in Case 5. Mean lift shows oscillatory convergence in Case 3 and divergence in Case 1, so its grid uncertainty is taken as the largest difference among the grids. This gives 29% for Case 3, driven by M1, although M2 and M3 differ by only 0.1%, and 4.9% for Case 1. The mean-lift grid uncertainty for Case 5 is 41%.

The lift RMS of Case 1 increases from 0.115 to 0.141 and 0.166 as the grid is refined. Its apparent order is only 0.29, giving an extrapolated value of 0.429 and $U_{\mathrm{GCI}} = 255\%$, compared with 47% when the formal order $p = 2$ is used. This quantity is not grid-converged on the tested grids. Its increase with refinement does not establish a lower bound for other sections or for the continuum solution; differences in C_l' are assessed only against the adopted numerical allowance. Under the rule in Section 2.9, Cases 2 and 4 are assigned grid uncertainties of 3.6% for C_d, 29% for C_l, 0.8% for C_m, 255% for C_l' and 12.5% for St. Unless stated otherwise, the following results use M2.

Table 3 Grid convergence of the mean coefficients, the lift RMS and the Strouhal number. Convergence: type of the M1–M2–M3 sequence, with the apparent order p for monotonic sequences (where it exceeds 2, $p = 2$ is used for ϕ_{ext} and U_{GCI}); ϕ_{ext} or basis of U: extrapolated value, or the three-grid range on which U_{GCI} is based for oscillatory and divergent sequences; U_{GCI}: discretisation uncertainty of the M2 value, in % of that value. All runs at a maximum Courant number of 2

Section	Quantity	M1	M2	M3	Convergence (p)	ϕ_{ext} or basis of U	U_{GCI} (%)
Case 1	C_d	1.276	1.284	1.283	Oscillatory	Three-grid range	0.6
	C_l	1.355	1.388	1.423	Divergent	Three-grid range	4.9
	C_m	0.874	0.869	0.866	Monotonic (2.59)	0.863	0.8
	C_l'	0.115	0.141	0.166	Monotonic (0.29)	0.429	255.4
	St	0.134	0.138	0.141	Monotonic (0.72)	0.152	12.5
Case 3	C_d	1.199	1.244	1.242	Oscillatory	Three-grid range	3.6
	C_l	0.675	0.522	0.522	Oscillatory	Three-grid range	29.4
	C_m	0.811	0.838	0.839	Monotonic (10.70)	0.840	0.3
	C_l'	0.662	0.751	0.770	Monotonic (5.26)	0.790	6.4
	St	0.167	0.168	0.170	Divergent	Three-grid range	2.0
Case 5	C_d	0.607	0.620	0.626	Monotonic (3.35)	0.631	2.2
	C_l	0.189	0.272	0.314	Monotonic (2.32)	0.361	41.1
	C_m	0.335	0.339	0.345	Divergent	Three-grid range	2.8
	C_l'	0.293	0.357	0.355	Oscillatory	Three-grid range	18.0
	St	0.200	0.215	0.215	Oscillatory	Three-grid range	7.2

3.1.2 Near-wall resolution

Changing the first-layer thickness from 8 mm to 5 or 20 mm changes mean drag by less than 2% in Cases 1 and 5. The mean lift of Case 5 is more sensitive, changing by −23% with a first-layer thickness of 5 mm and by +4.9% with 20 mm. In the 20 mm test, the layer count and growth ratio also change to preserve the total prism-layer thickness. This comparison tests the near-wall configuration as a whole. Appendix G.4 gives the full results and wall-resolution distributions. All production sections retain the same wall-function treatment.

3.1.3 Time step

Cases 1, 3, 4 and 5 were repeated on M2 with the maximum Courant number reduced from 2 to 1. For Case 1, the changes are small: +0.04% in C_d, −0.44% in C_l, −0.23% in C_m and −0.01% in St. In Cases 3 and 4, C_d, C_m, C_l' and St change by less than 0.4%. The mean lift of Case 3 rises by 2.5%, from 0.522 to 0.535, almost entirely through the pressure contribution of the top face; that of Case 4 changes by −0.2%.

Case 5 is more sensitive to the time step. Reducing the maximum Courant number from 2 to 1 lowers C_d by 4.95% and C_l' by 22%, raises C_l by 19.4%, and changes St by only −0.4%. The recirculation length increases from 7.75 to 8.75 m. A further run uses a maximum Courant number of 0.5. Between Courant numbers of 1 and 0.5, C_d, C_l' and the fluctuating moment change by at most 0.5%, C_m by −1.3% and St by −0.8%. The mean pressure on the leeward face remains unchanged. Mean lift falls by 5.5%, from 0.325 to 0.307, mainly through pressure changes on the bottom plate and top face. This change is 28–44 times the statistical uncertainty of the means and cannot be explained by sampling error. In all three runs, the largest Courant number occurs in the same cell: the first wall cell below the windward lower corner.

Case 5 uses a maximum Courant number of 1 in the production calculations (Section 2.6), and Section 4 shows the results from this run. The difference between Courant numbers of 1 and 0.5 defines its time-step uncertainty, $U_{\Delta t}$: 5.5% for C_l and at most 1.3% for the other quantities. For Cases 1, 3 and 4, $U_{\Delta t}$ is the difference between Courant numbers of 2 and 1; Case 2 is assigned the larger value from Cases 1 and 3. The grid study and other

sensitivity tests for Case 5 in this section use a maximum Courant number of 2. They are assessed relative to the Case 5 run at the same Courant number, and the relative grid uncertainties in Table 3 are applied to the production values at a Courant number of 1.

The production calculations use a maximum Courant number of 2 for Cases 1–4 and 1 for Case 5, its angle-of-attack series and the variant sections. The factorial sets and variant comparisons also use the runs of Cases 3 and 4 at a Courant number of 1, so these comparisons share the same time-step control (Section 2.6).

3.1.4 Statistical convergence

Appendix E shows the running means, RMS values and Strouhal number for all five sections. Following the residual-based approach of Álvarez and Nieto [30], the change caused by adding one shedding cycle is expressed as $\mathrm{res}_n = 100\,|\phi_n - \phi_{n-1}|/|\phi|$. Here, ϕ_n is calculated from the start of the accepted window to the end of the nth complete shedding cycle, while ϕ uses the full accepted window. The Strouhal number is based on the mean period of the complete cycles included. The normalisation and cycle-by-cycle extension of the window are specific to this analysis.

Over the last ten cycles, the residual remains below 0.04% for all seven quantities in all five sections. The 5% line is a reference from the cited study, not an independent accuracy bound. We retain the windows defined in Section 2.9 and Appendix A, with the remaining sampling error represented by U_s and U_w. These checks assess whether the sampled statistics remain stable over the accepted windows.

3.1.5 Inflow, turbulence model and far-field conditions

Case 5 has lower drag than Case 1 under all tested changes in inlet turbulence, sustaining terms, Reynolds number, turbulence closure and far-field conditions. The size of the reduction depends on the model: at a maximum Courant number of 2, it is 52% with SST and 63% with realizable k–ε. The latter model almost suppresses shedding on both sections. Lower inlet turbulence strongly changes the lift fluctuations of Case 1, while reducing the velocity also changes y^+. These comparisons do not define a model-error bound.

Using `freestream` outer boundaries at zero angle of attack changes drag by at most 0.16% in Cases 1, 4 and 5. Each incidence comparison uses a zero-angle reference with the same boundary conditions. Appendix G.5 gives the settings, accepted windows and changes in individual coefficients.

3.2 Benchmark comparisons

We compare the numerical set-up with published measurements and benchmark results for two closed box sections of the Great Belt East Bridge and the BARC rectangular cylinder. The box sections test the wall-function approach at full-scale Reynolds numbers, as used for the deck calculations. BARC tests the turbulence model on a sharp-edged section at a Reynolds number with extensive wind-tunnel and numerical data. Unless stated otherwise, these runs use the solver, schemes, time-step control and M2 grid parameters of the deck calculations, including a surface cell size of 0.031 m.

3.2.1 Great Belt East Bridge suspension-span girder

The suspension-span section is reconstructed from Larsen [33], with $B = 31.0$ m and $D = 4.4$ m. It is computed at $\alpha = -4°$, $0°$ and $+4°$, with $Re_D \approx 7.5 \times 10^6$. Deck equipment is not included in the model. We also test a second bottom width because the source drawing does not clearly specify this dimension. The original paper does not state how the coefficients are normalised. For this comparison, we assume that the drag coefficient uses D, the lift coefficient uses B and the moment coefficient uses B^2. Table 4 shows a difference of 2–3% between the computed and measured central lift slopes. The computed moment slope is 24–55% higher than the measurements. At zero angle of attack, the computed drag is less than half the measured value, and the lift offset is about 0.3–0.4. This comparison cannot directly validate the model because the geometry, flow conditions and deck equipment differ from those in the experiments. Appendix G.6 gives the full settings and describes the nonlinearity of the lift curve.

3.2.2 Great Belt approach-span girder

The approach-span section of Schewe and Larsen [34], with $B = 25.8$ m and $D = 7.0$ m, is computed at $Re_D = 10^7$ and 0.3% inlet turbulence. The computed drag coefficient of 0.761 and Strouhal number of 0.176 differ from the experimental high-Reynolds-number plateaux of 0.60 and 0.22. Flow along the bottom plate remains separated, while the experiments show reattachment (Fig. 4(b)). Increasing inlet turbulence to 5% does not recover reattachment. The wall-resolved run did not reach the averaging interval and is not used in the comparison. This discrepancy directly affects the interpretation of the deck comparisons: delayed reattachment behind sharp corners could overstate the computed benefit of streamlining. The present runs do not bound the size of this error.

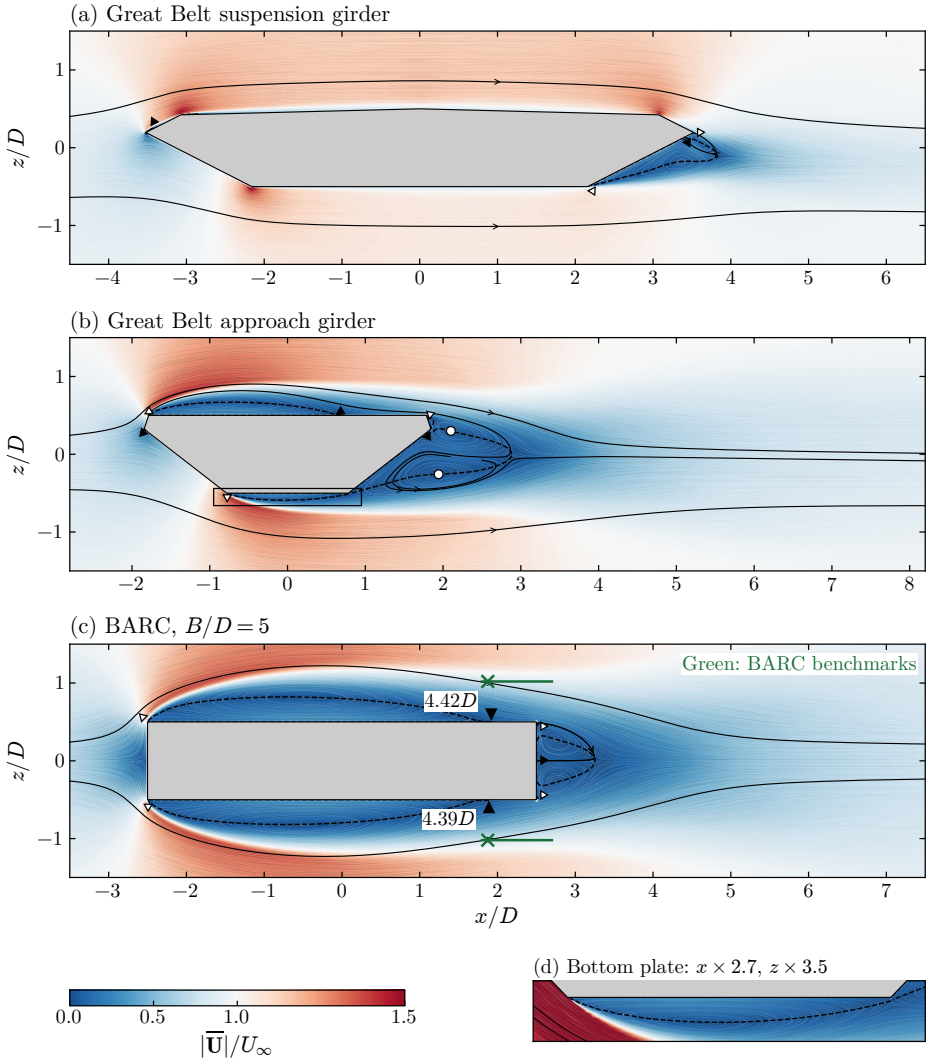


Fig. 4 Mean validation flow over 40–160 s: (a) Great Belt suspension girder at $\alpha = 0°$; (b) approach girder; (c) BARC; (d) bottom plate of (b), with magnifications stated in the panel. Colour shows speed. Arrows show mean streamlines. Dashed lines show $\overline{U}_x = 0$, and circles show vortex centres. Small triangles show where the near-wall flow changes sign. A sign change is treated as reattachment only if a reversed-flow region is present upstream. In (c), black triangles show computed reattachment at $4.42D$ and $4.39D$ from the leading edge. The green bars show the numerical spread of $2.25D \pm 0.45D$ from the centre, and the green crosses show the wind-tunnel location of $1.875D$, both reported by Bruno et al. [35]. The benchmark markers are shifted in the normal direction for visibility. Their streamwise positions are unchanged. Coordinates are relative to the centre of each section

3.2.3 BARC rectangular cylinder

The BARC rectangle, with $B/D = 5$, is computed at $Re_D = 4 \times 10^4$ and 0.3% inlet turbulence. We found that the resolution near the wall was $y^+ \approx 1$–2, whilst retaining the wall function boundary conditions. The drag coefficient was 1.080 and the Strouhal number was 0.119; the reattachment positions were all within the range reported in Bruno et al. [35]. The reattachment positions are also close to those observed in wind tunnel measurements (Fig. 4(c)). However, the drag values here are approximately 3% higher than the measured range, and the RMS value of lift, 0.780, exceeds the reported experimental value of approximately 0.4. This comparison shows agreement for selected quantities in a different near-wall and Reynolds-number regime; it does not validate the wall-function deck comparisons. Appendix G.6 gives the full pressure and reattachment results.

3.2.4 Scope of the benchmark evidence

The benchmarks show response- and regime-dependent agreement (Table 4). For BARC at $y^+ \approx 1$–2, mean drag, Strouhal number and mean reattachment length fall within the spread of the numerical benchmark contributions. For the Great Belt suspension-span girder, the computed lift slope is within 2–3% of the measured value. Larger

Table 4 Benchmark cases: computed and measured coefficients. GB-S: Great Belt East Bridge suspension-span girder (1:80 section model / 1:300 taut-strip model); GB-A: approach-span girder; BARC: average ± standard deviation of the numerical contributions and range of the wind-tunnel data (WT) summarised by Bruno et al. [35], all coefficients on D. Slopes per radian, computed from the runs at ±4°; the +4° run is averaged over 150–240 s

Case	Quantity	Reference	Present
GB-S	$C_{d,0}$ (on D)	0.57 / 0.59	0.273
	$C_{l,0}$ (on B)	0.067 / −0.050	0.350
	$\mathrm{d}C_l/\mathrm{d}\alpha$	4.37 / 4.41	4.51
	$C_{m,0}$ (on B^2)	0.028 / 0.013	0.032
	$\mathrm{d}C_m/\mathrm{d}\alpha$	1.17 / 0.93	1.45
GB-A	C_d (on D)	0.60 ($Re_D \geq 2\times10^6$)	0.761
	St	0.22 ($Re_D > 4\times10^5$; prototype 0.21)	0.176
BARC	C_d	1.074 ± 0.129; WT 0.94–1.05	1.080
	St	0.109 ± 0.015; WT 0.105–0.132	0.119
	C_l'	0.65 ± 0.37; WT ≈ 0.4	0.780

discrepancies occur in the loads at zero angle of attack and in the moment slope (Section 3.2.1). For the approach-span girder, the model overpredicts drag and fails to reproduce reattachment along the bottom plate (Section 3.2.2). The two comparisons test different aspects of model performance. Section 5.3 discusses what these discrepancies mean for interpreting and transferring the geometric contrasts found in this study.

4 Results

4.1 Mean and fluctuating loads

Table 5 shows the time-averaged coefficients, lift RMS and Strouhal number for the five sections on M2, together with their numerical allowances. All runs show periodic vortex shedding after the initial transient, and the accepted windows contain 43–68 shedding cycles. Fig. 5 shows the mean flow around each section, while Fig. 6 compares the instantaneous wakes of Cases 1 and 5 at a lift maximum. Appendix F gives the corresponding wake snapshots and instantaneous turbulence-model fields for all five sections. The lift spectra in Appendix H.6 contain one shedding frequency and its harmonics, with no second independent peak. The spectral peak found by parabolic interpolation differs by no more than 0.0003 from the Strouhal number obtained from upward crossings.

Full streamlining (Case 5) reduces computed drag by 54% relative to Case 1. Mean lift and moment fall to 23% and 39% of their Case 1 values, while the Strouhal number rises from 0.138 to 0.214. The edge deflectors of Case 4 leave mean drag and lift almost unchanged, lower the moment by 17% and increase lift RMS by about a factor of four. Encasing the girders (Case 2) reduces drag by 1.3%, mean lift by 9% and moment by 13%. Closing the cavity (Case 3) reduces drag by only 3.1%, but lowers mean lift to about 38% of its Case 1 value. The moment changes little, the Strouhal number rises to 0.168, and lift RMS is about five times that of Case 1.

When the numerical allowances of two sections are treated as independent, only the drag reduction of Case 5 is resolved. The reductions of Cases 2–4, at 1.3–3.1%, are smaller than their allowances of about 3.5 percentage points (Table 5). The mean-moment changes in Cases 2, 3 and 4 are resolved, as are the lower mean lift and higher Strouhal number of Case 3, and the lower mean lift and moment and higher Strouhal number of Case 5. The mean-lift change in Case 2 and the Strouhal-number changes in Cases 2 and 4 are unresolved. Because the lift RMS of Case 1 is not grid-converged (Section 3.1.1), only the increase in Case 3 exceeds the adopted allowance. The increases in Cases 4 and 5 exceed the allowance only when the formal order $p = 2$ is used; that in Case 2 remains unresolved under either treatment.

4.2 Pressure distributions and drag breakdown

Table 6 divides mean pressure drag among the outer windward faces, outer leeward faces and, for open sections, the cavity walls between the girders. Appendix H.6 gives the surface-pressure distributions, and Fig. 5 shows the mean flow. The base pressure coefficient C_{pb} is the mean pressure coefficient on the outer leeward faces, weighted by their projected height. The recirculation length L is measured from the trailing edge to the downstream end of the region with negative mean streamwise velocity in the wake.

Pressure accounts for almost all the drag of the five sections. The viscous contribution is slightly negative for the four sharp-edged sections, at −0.02% to −0.29% of total drag. Wall shear beneath the separated shear layers on the top and bottom faces points upstream. For Case 5, whose rounded edges keep the flow attached over a longer

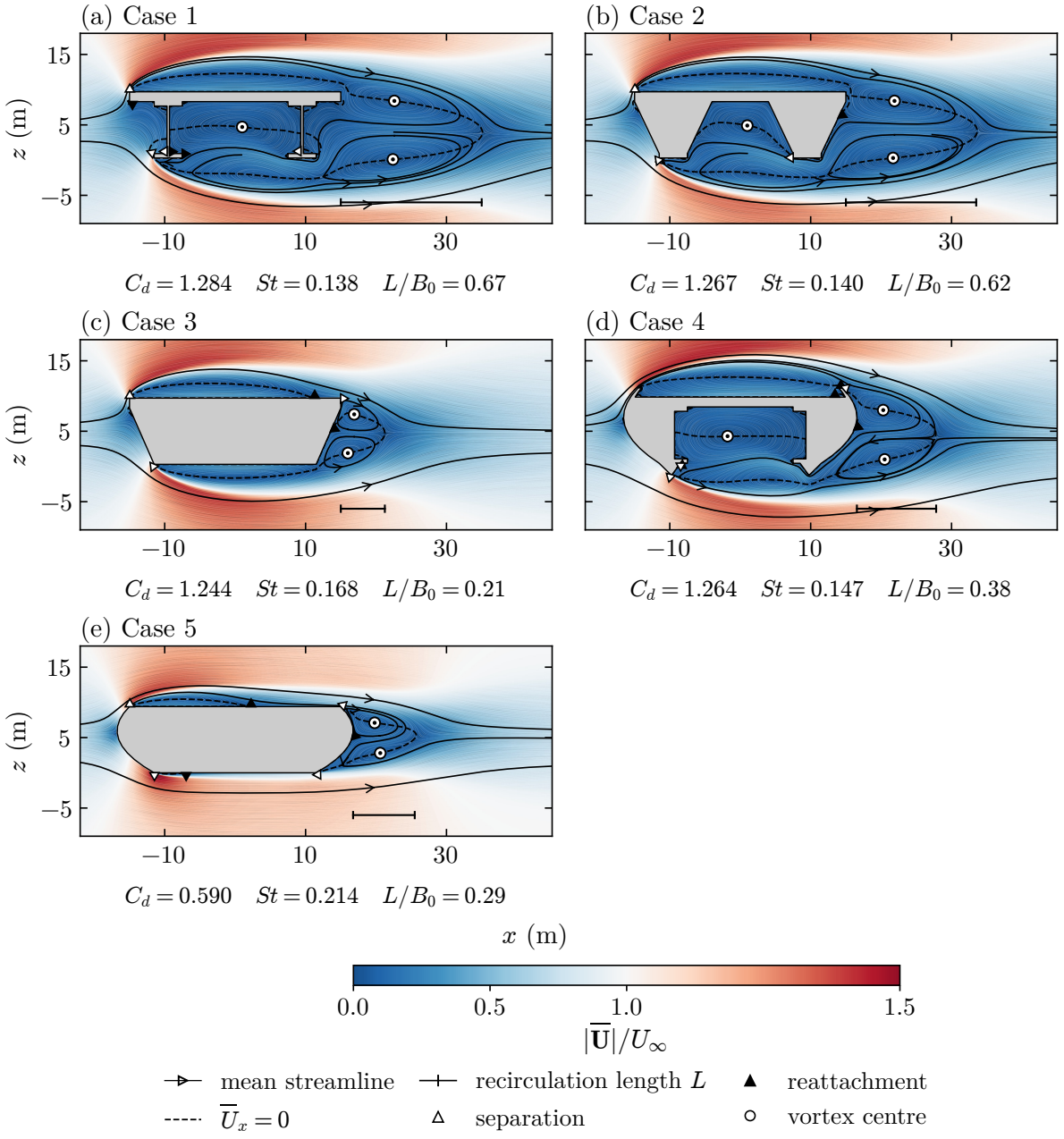


Fig. 5 Time-averaged flow around the five sections on M2 (40–160 s; Case 5 at a maximum Courant number of 1). Colour: velocity magnitude; texture: line-integral convolution of the mean velocity; arrows: mean streamlines. The shared colour scale is piecewise linear, centred on $|\overline{\mathbf{U}}|/U_\infty = 1$. Dashed: $\overline{U}_x = 0$; bracket: recirculation length L, measured from the most downstream point of each section; open and filled triangles: candidate separation and reattachment indicators on the outer faces, from the sign of the mean tangential velocity in the wall-adjacent cells; circles: centres of the mean recirculating regions in the cavity and wake. The strips below the panels give C_d and St of Table 5 (Case 2 over 100–250 s) and L/B_0, where $B_0 = 30$ m

distance, the viscous contribution is +0.85%. The drag reduction from Case 1 to Case 5 comes entirely from pressure drag, which falls from 1.286 to 0.585, a reduction of 54.5%. These viscous contributions are obtained with the common wall-function treatment.

In the open sections, suction within the cavity is nearly uniform (Appendix H.6). It pulls the windward girder downstream and the leeward girder upstream. These contributions cancel to within 0.02 in Cases 1 and 2 and 0.06 in Case 4, so the cavity contributes little to net drag. The outer windward pressure-drag contribution falls from 0.82 in Case 1 to 0.71 in Case 3, 0.54 in Case 4 and 0.22 in Case 5. From Case 1 to Case 5, the pressure-drag coefficient $C_{d,p}$ decreases by 0.702, and the total drag coefficient decreases by 0.694. The windward faces

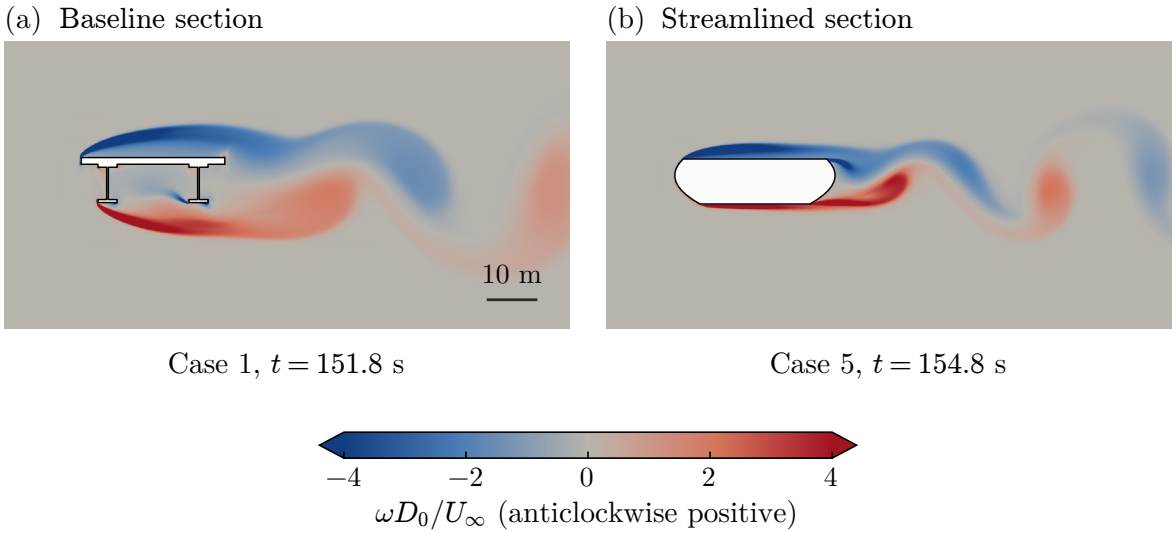


Fig. 6 Instantaneous spanwise vorticity $\omega D_0/U_\infty$ around (a) the baseline and (b) the streamlined section. Each snapshot is taken at a lift maximum within 144–160 s on M2. The maximum Courant number is 2 for Case 1 and 1 for Case 5. Both panels use the same spatial scale and colour limits, −4 and +4, with D_0 = 9.4 m. Red indicates anticlockwise vorticity and blue indicates clockwise vorticity

Table 5 Time-averaged force and moment coefficients, root-mean-square lift and Strouhal number on M2 at $\alpha = 0°$ and $Re = 1.6 \times 10^7$, all based on $A_{\text{ref}} = 9.4$ m^2, $L_{\text{ref}} = 9.4$ m and the moment point of Section 2.5. R_D: drag reduction relative to Case 1. Case 5 at a maximum Courant number of 1 (Section 3.1.3). The second row of each section gives the numerical allowance $\pm U$ of the value above it (Section 2.9): the root-sum-square of the grid (U_{GCI}), time-step ($U_{\Delta t}$), statistical (U_s) and window-end (U_w) contributions, with no window-end term for C_l' and St. For example, the drag coefficient of Case 1 is 1.284 ± 0.008. For R_D the allowances of the two drag coefficients are combined as independent

Section	C_d	C_l	C_m	C_l'	St	R_D (%)
Case 1 (Baseline)	1.284	1.388	0.869	0.141	0.138	0 (ref.)
	±0.008	±0.068	±0.007	±0.360[a]	±0.017	–
Case 2 (Encase)	1.267	1.260	0.758	0.180	0.140	1.3
	±0.045	±0.372	±0.007	±0.459[a]	±0.018	±3.6
Case 3 (Enclose)	1.244	0.522	0.838	0.751	0.168	3.1
	±0.045	±0.154	±0.004	±0.048	±0.003	±3.5
Case 4 (Deflect)	1.264	1.395	0.721	0.579	0.147	1.5
	±0.045	±0.410	±0.006	±1.478[a]	±0.018	±3.6
Case 5 (Streamline)	0.590	0.325	0.340	0.279	0.214	54.1
	±0.013	±0.135	±0.011	±0.050	±0.016	±1.1

[a] With the formal order $p = 2$: ±0.066, ±0.085 and ±0.272 for Cases 1, 2 and 4 (Section 3.1.1).

account for 85% of the pressure-drag reduction and the leeward faces for 17%; removing the cavity contribution offsets 2%. The rounded, blunt nose confines the stagnation pressure to a small area and causes the flow field to flow around its upper and lower edges, thereby creating a strong suction force in this region. The values 0.82 and 0.22 represent the integral values of the pressure and drag contributions on the windward side; they are not area-averaged pressure coefficients.

Case 5 has the lowest drag and the highest base pressure. Its base-pressure coefficient is −0.36, compared with −0.48 for Case 1, an increase of 0.12. The higher base pressure agrees with the relation between base pressure and bluff-body drag discussed by Roshko [41]. From Case 1 to Case 5, the integrated windward pressure-drag contribution decreases by 0.60. The pressure budget shows that most of the total drag reduction comes from the windward surface. The leeward surface contributes a smaller part. Among the four sharp-edged sections, Case 3 has the shortest recirculation region ($L/B_0 = 0.21$) and the lowest base pressure (−0.54). This combination is consistent with the relation between formation length and base pressure discussed by Roshko [48]. It still has the lowest drag of these four sections because its windward pressure-drag contribution is lower: 0.71, compared with 0.81–0.82 in Cases 1 and 2. Drag differs by only about 3% among the four sections and depends on the combined windward and leeward contributions. In Case 4, the deflectors reduce the windward contribution, but their greater projected height of 12.3 m increases the leeward suction contribution. The two changes nearly cancel.

The resolved pressure RMS peaks near the upper trailing edge, although the peak occurs on different wall faces in different geometries (Appendix H.6). In Case 3, it lies on the vertical leeward slab edge; in Case 4, it lies on the deck top just inboard of the deflector lip. The maxima for Cases 1–5 are 0.14, 0.16, 0.42, 0.27 and 0.21. The surface-averaged C'_p values are 0.03, 0.04, 0.15, 0.09 and 0.04, following the same ranking as lift RMS in Table 5. In Cases 3 and 4, pressure RMS is high across the leeward half of the section. These RMS values describe the resolved, mainly periodic pressure fluctuations; modelled turbulent pressure fluctuations are excluded.

Table 6 Breakdown of the mean drag on M2 (40–160 s; Case 2 over the same interval, whose C_d differs from that of Table 5 by less than 0.1%). Pressure drag of the outer windward faces, the outer leeward faces and the faces inside the cavity, as contributions to C_d; viscous drag in % of C_d; base pressure C_{pb} relative to the outlet pressure (relative to the upstream static pressure it is lower by 0.02 to 0.04); recirculation length L in units of B_0 = 30 m, resolved to ±0.25 m

Section	C_d	Windward	Leeward	Cavity	Viscous (%)	C_{pb}	L/B_0
Case 1	1.284	0.82	0.48	−0.01	−0.19	−0.48	0.67
Case 2	1.267	0.81	0.48	−0.02	−0.17	−0.48	0.62
Case 3	1.244	0.71	0.54	–	−0.29	−0.54	0.21
Case 4	1.264	0.54	0.66	0.06	−0.02	−0.50	0.38
Case 5	0.590	0.22	0.36	–	+0.85	−0.36	0.29

4.3 Factorial decomposition

Table 7 gives the section values and numerical allowances. Table 8 shows which effects pass the dependence sensitivity check and which are resolved only under independent errors, while Fig. 7 shows the two principal interactions. All four corners of both factorial sets use a maximum Courant number of 1 and an averaging window of 40–120 s, except GA_LE, which uses 60–120 s (Section 2.9). Case 3 enters these comparisons with C_d = 1.248, rather than the value of 1.244 in Table 5.

Table 7 Variant-section results at maximum Courant number 1. Window: the interval of simulated time over which the statistics are averaged; the start-up transient before it is discarded. It is 40–120 s, except for GA_LE (start-up transient until about 55 s) and GC_NOLIP (mean lift settling with a time constant of about 20 s), which use 60–120 s (Table 10). Case 4 is listed at both windows, so that each of its two removals is compared with it over the same interval. Parentheses give the numerical allowance U of Section 2.9, not a confidence interval. All force coefficients use D_{ref} = 9.4 m and the common moment centre

Section	Window (s)	C_d	C_l	C_m	C'_l	St
Case 3	40–120	1.248 (0.045)	0.534 (0.158)	0.840 (0.005)	0.753 (0.048)	0.167 (0.003)
GA_LE	60–120	1.189 (0.043)	0.094 (0.029)	0.458 (0.007)	0.796 (2.033)	0.216 (0.027)
GA_TE	40–120	1.180 (0.042)	0.878 (0.263)	0.807 (0.013)	0.889 (2.271)	0.161 (0.020)
Case 5	40–120	0.590 (0.013)	0.326 (0.135)	0.339 (0.011)	0.278 (0.050)	0.214 (0.015)
GB_OPEN_S	40–120	1.155 (0.042)	1.110 (0.332)	0.804 (0.016)	0.294 (0.752)	0.153 (0.019)
GB_OPEN	40–120	0.587 (0.021)	−0.627 (0.188)	0.422 (0.007)	0.391 (0.998)	0.201 (0.025)
GD_ROUND	40–120	0.632 (0.023)	−0.260 (0.079)	0.471 (0.007)	0.383 (0.979)	0.238 (0.030)
Case 4	60–120	1.265 (0.045)	1.382 (0.407)	0.726 (0.007)	0.578 (1.476)	0.147 (0.019)
GC_NOLIP	60–120	1.089 (0.039)	1.241 (0.372)	1.297 (0.020)	0.374 (0.956)	0.151 (0.019)
Case 4	40–120	1.264 (0.045)	1.386 (0.408)	0.723 (0.006)	0.579 (1.479)	0.147 (0.019)
GC_NOFIN	40–120	0.783 (0.028)	0.146 (0.044)	−0.021 (0.003)	0.466 (1.190)	0.167 (0.021)

In set A, the reduction in drag calculated when both edges are designed to be curved is significantly greater than when only one edge is designed to be curved. Taking the baseline values from Case 3 as an example, designing

only the leading edge as a curved edge (GA_LE) reduces the C_d value from 1.248 to 1.189; designing only the trailing edge as a curved edge (GA_TE) reduces it to 1.180. These changes are all point estimates. The reduction achieved by GA_LE is less than its independent contrast tolerance (approximately 0.062), and the reduction on either side does not exceed the sum of the tolerances for both corners (approximately 0.09) . When both edges are curved (Case 5), C_d drops to 0.590, whereas the additive prediction according to Eq. (2) should be 1.121.

The two main drag effects are almost equal, at −0.325 and −0.334 respectively. The interaction term of −0.266 exceeds the numerical tolerance adopted and is of the same order of magnitude as the main effects. Of the 0.659 reduction observed from Case 3 to Case 5, the changes in the leading edge and trailing edge account for 0.059 and 0.068 respectively. Their non-additive contribution accounts for the remaining 0.531, with a point estimate of approximately 81%. With Case 3 as the baseline, this fraction is $(-2E_{12})/(C_{d,3} - C_{d,5}) = 0.8064$, calculated from the unrounded coefficients in the set A windows. Because the numerator and denominator share corner values, the interaction is assessed using the four-corner allowances. Thus, 81% measures the non-additive fraction of the Case 3-to-Case 5 drag reduction, whereas 25% measures $E_{12}^2/(E_1^2 + E_2^2 + E_{12}^2)$, the interaction share of the sum of squared effects across set A (Table 8, Section 2.2).

Table 8 Main effects and interactions (Eq. (1)), independent allowance U_E, dependence sensitivity scale $U_{E,\mathrm{dep}}$, and shares (%): E_1^2, E_2^2 and E_{12}^2 as percentages of $E_1^2 + E_2^2 + E_{12}^2$, in that order, which compare the sizes of the two main effects and the interaction. Set A: factor 1 leading edge, factor 2 trailing edge (− inclined, + curved). Set B: factor 1 cavity (− closed, + open), factor 2 edges (− inclined, + curved). Windows are listed in Table 7. Bold: $|E| > U_{E,\mathrm{dep}}$; dagger: $U_E < |E| \leq U_{E,\mathrm{dep}}$

Set	Response	E_1	E_2	E_{12}	U_E	$U_{E,\mathrm{dep}}$	Shares
A	C_d	**−0.325**	**−0.334**	**−0.266**	0.038	0.072	37/39/25
A	$C_{d,p}$	**−0.334**	**−0.333**	**−0.265**	0.038	0.072	38/38/24
A	C_l	**−0.496**	0.289†	−0.056	0.168	0.292	74/25/1
A	C_m	**−0.425**	**−0.076**	**−0.043**	0.009	0.017	96/3/1
A	C_l'	−0.284	−0.191	−0.327	1.524	2.201	36/16/48
A	St	**0.051**	−0.004	0.003	0.019	0.033	99/1/0
B	C_d	−0.048†	**−0.613**	0.045†	0.033	0.060	1/99/1
B	$C_{d,p}$	−0.047†	**−0.619**	0.048†	0.033	0.060	1/99/1
B	C_l	−0.188	**−0.972**	**−0.765**	0.217	0.406	2/60/37
B	C_m	**0.023**	**−0.442**	**0.059**	0.010	0.019	0/98/2
B	C_l'	−0.173	−0.189	0.285	0.626	0.924	20/24/55
B	St	−0.014	**0.048**	0.001	0.018	0.032	8/92/0

For C_l', replacing the observed order by $p = 2$ gives $(U_E, U_{E,\mathrm{dep}}) = (0.283, 0.445)$ for set A and $(0.120, 0.211)$ for set B. This is a sensitivity calculation, not the adopted budget. For $C_{d,p}$, the relative grid, time-step and statistical terms from total drag are transferred in proportion to the pressure-drag magnitude; these rows do not constitute independent convergence tests of the pressure component.

The leading-edge shape also has the largest effect on the mean moment and the Strouhal number. It accounts for 96% of the sum of squared effects for C_m and is the only factor with a resolved effect on St (+0.051). Curving the leading edge lowers mean lift ($E_1 = -0.50$), while curving the trailing edge raises it ($E_2 = +0.29$). The trailing-edge effect exceeds the independent allowance of 0.168 but not the dependence sensitivity scale of 0.292. The lift interaction is unresolved.

In set B, the point estimates show that opening the cavity changes drag more with inclined edges than with curved edges. Opening the bottom of Case 3 (GB_OPEN_S) lowers C_d from 1.248 to 1.155, a reduction of 7.5%. The open variant of Case 5 (GB_OPEN) has nearly the same drag as the closed section, at 0.587 compared with 0.590, within the numerical allowance. Edge shape accounts for 99% of the sum of squared effects for C_d and 98% for C_m. The main effect of cavity opening and its interaction with edge shape are small, at −0.048 and +0.045 in C_d. Both exceed the independent allowance of 0.033 but remain below the dependence sensitivity scale of 0.060. Whether they are resolved depends on the assumed error correlation.

In mean lift, the effect of cavity opening depends on edge shape. Opening the cavity approximately doubles the lift of the inclined-edge section, from 0.53 to 1.11, but reverses the sign for the curved-edge section, changing C_l from +0.33 to −0.63. The lift interaction, $E_{12} = -0.765$, exceeds both the independent allowance $U_E = 0.217$ and the dependence sensitivity scale $U_{E,\mathrm{dep}} = 0.406$ (Table 8); the main effect of opening exceeds neither. The interaction is resolved under the adopted four-corner numerical budget; the near-wall sensitivity results are reported separately in Section 3.1.2. Applying the inclined-edge opening increment to the closed curved-edge section would predict $C_l = +0.903$, compared with its computed open-section value of −0.627. The difference of −1.530 is the interaction contrast $2E_{12}$.

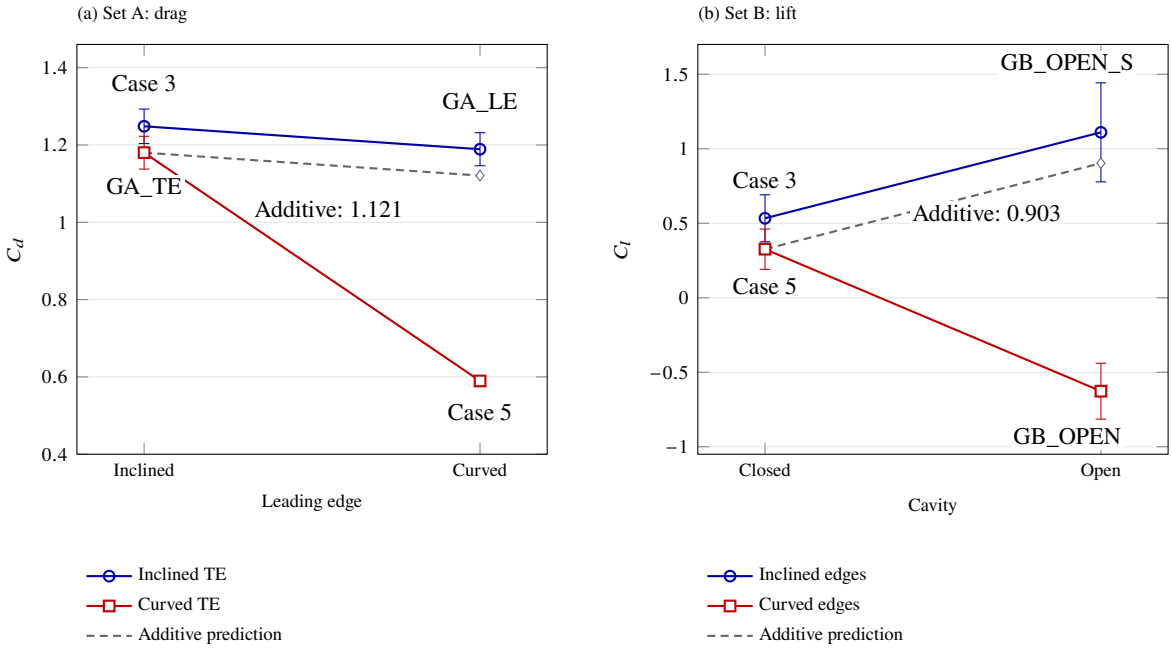


Fig. 7 Computed interactions and additive predictions for drag in set A (a) and lift in set B (b). Blue circles and red squares show the four computed configurations in each panel. The bars give the section allowances $\pm U$ from Table 7; they are not confidence intervals. The grey dashed line applies the change along the blue line to the starting value of the red line. Its diamond gives the additive prediction from Eq. (2), rather than an additional simulation result. Subtracting the diamond value from the red endpoint gives $2E_{12}$: -0.531 in (a) and -1.530 in (b). The diamond has no independent error bar. The contrast uses the shared corner values and the dependence sensitivity check in Table 8. Lines join only the two tested levels of each factor

In both sets, the effects on C_d come almost entirely from pressure. The viscous part of each effect has a magnitude below 0.01. No effect on lift RMS is resolved when the Case 1 grid uncertainty is applied to the variant sections. With the formal order $p = 2$ and independent errors, the leading-edge effect and interaction in set A exceed their numerical allowances. All three effects in set B also exceed their allowances. When error dependence is included in the sensitivity check at $p = 2$, only the set B interaction exceeds the corresponding scale. Section 5.2 compares the effect shares obtained here with those reported by Zheng et al. [16] for closed box girders.

4.3.1 Pressure-force partition

We integrate wall pressure over five surface regions to determine where the two principal interactions occur. Fig. 8 shows the drag contributions for set A. The regions are the horizontal top, external bottom plate, cavity walls where present, leading outer surface and trailing outer surface. Each wall face is counted once, including the short vertical faces at the slab edges. All sections use the same rule for defining the upstream reference pressure. Appendix C explains the integration and the recovery of means for the selected time windows. The integrated pressure forces differ from the independently saved pressure-force histories by no more than 1.3×10^{-5} in coefficient units. The regional contributions are point estimates. The total-load allowances in Table 7 do not give separate uncertainty bounds for each region.

Set A: drag compensation between the two edges.

Curving only the leading edge reduces its pressure-drag contribution from 0.679 to 0.197. At the same time, the trailing contribution increases from 0.573 to 0.986, leaving only a small net drag reduction in GA_LE. With both edges curved, the leading contribution is 0.204 and the trailing contribution is 0.380. The pressure-drag interaction is −0.26543. The leading outer surface contributes +0.00131, and the trailing outer surface contributes −0.26674. The horizontal faces have no streamwise projected area. The viscous interaction is −0.00020, and the total interaction is −0.26562.

Changing the leading edge gives a large local drag reduction, but almost all of the non-additive reduction comes from the trailing surface. These results describe different comparisons. The interaction is calculated as a difference of differences among the four configurations in set A. The windward contribution in Section 4.2 describes the overall change from Case 1 to Case 5. The two comparisons use different baselines and pressure references for their regional contributions, as explained in Appendix C.

Fig. 9 shows how the pressure changes on the different surfaces. GA_LE and Case 5 both have curved leading edges and similar pressure distributions over much of the top and bottom plates. Their trailing-surface pressures differ: suction is stronger in GA_LE over most of that surface. The profiles include the value at every wall face,

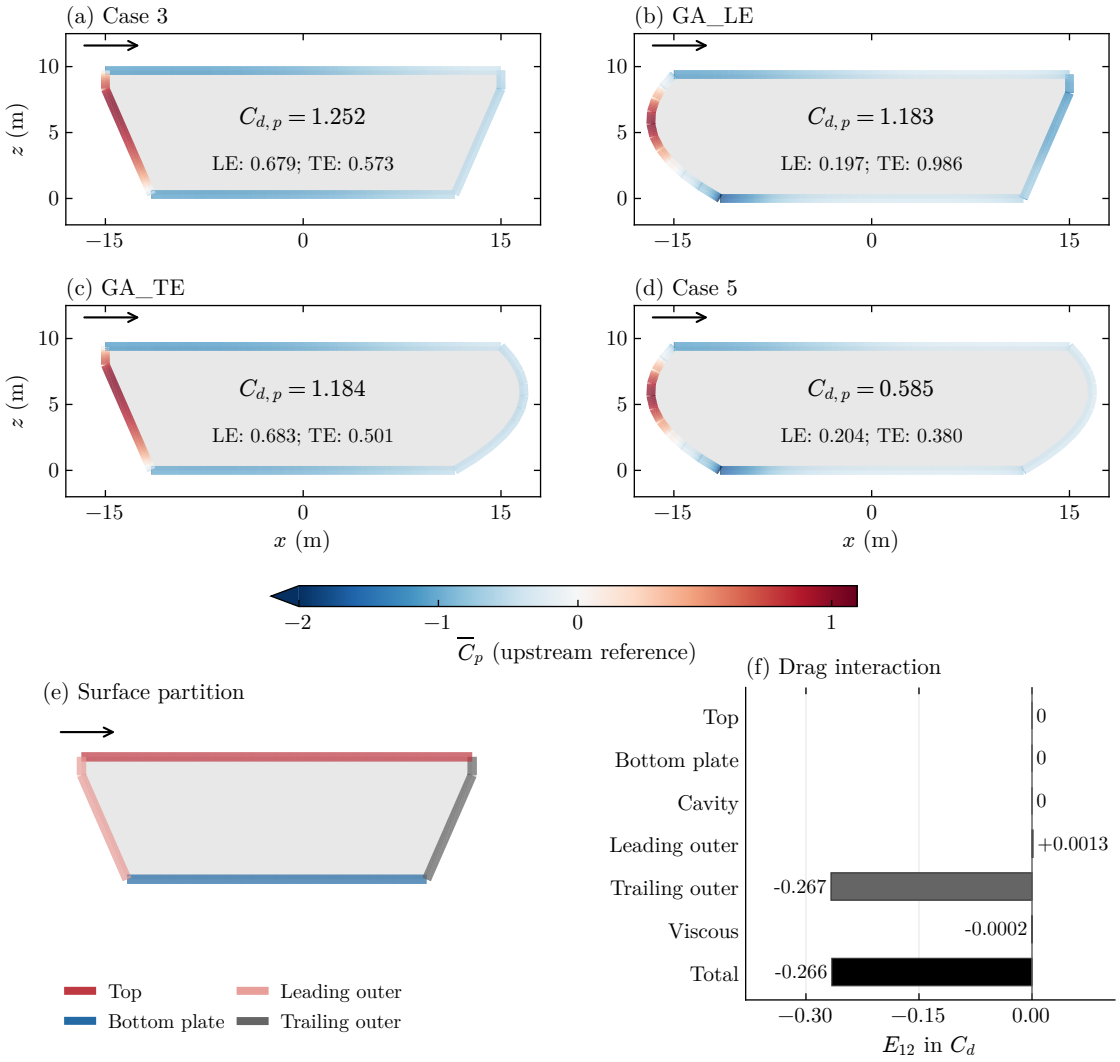


Fig. 8 Set A pressure accounting. (a–d) Wall $\overline{C}_p$ and pressure drag, including the leading (LE) and trailing (TE) outer-surface contributions. Columns change the leading edge and rows the trailing edge. The common colour scale saturates below -2; the minimum is -5.07, and all integrals use the unclipped values. (e) Exhaustive surface partition, illustrated on Case 3. (f) Signed regional contributions to E_{12}, the viscous remainder and the total from the force histories. There are no cavity walls in this closed set. All sections use M2 and maximum Courant number 1, over 40–120 s except GA_LE (60–120 s). Arrows indicate the inflow direction. No regional uncertainty bars are assigned

including extrema at corners and changes in face direction. We use the integrated forces to calculate the regional contributions. The individual extrema have not been checked separately for local mesh convergence. All profiles use the common 60–120 s window. Appendix C gives the resulting change in the integrated interaction.

Fig. 10 uses the same four-configuration layout as the pressure budget. The reversed-flow heights in GA_LE, GA_TE and Case 5 are similar, at 6.3–6.5 m, despite their different drag values. Reversed-flow height alone cannot explain these differences. The compensation between surface contributions can be determined from the pressure profiles and integrals, but not from the flow contours alone.

The downstream profiles in Appendix D show a narrower wake deficit for Case 5 than for Case 3. However, the centre-region velocity in Case 5 is still lower at the last sampled station, one reference depth downstream of its trailing extremity. The smaller wake width does not coincide with a higher centre-region velocity at that location.

Set B: lift redistribution on opening the cavity.

Fig. 11 separates the lift reversal into pressure changes on the remaining and newly exposed surfaces. Opening Case 5 changes the bottom-plate contribution by +0.849, adds a cavity-wall contribution of −1.570, changes the top contribution by −0.278, and changes the two outer-surface contributions together by +0.045. The net pressure change is −0.954, and the viscous change is +0.00086. Together, these account for the lift change from +0.326 to

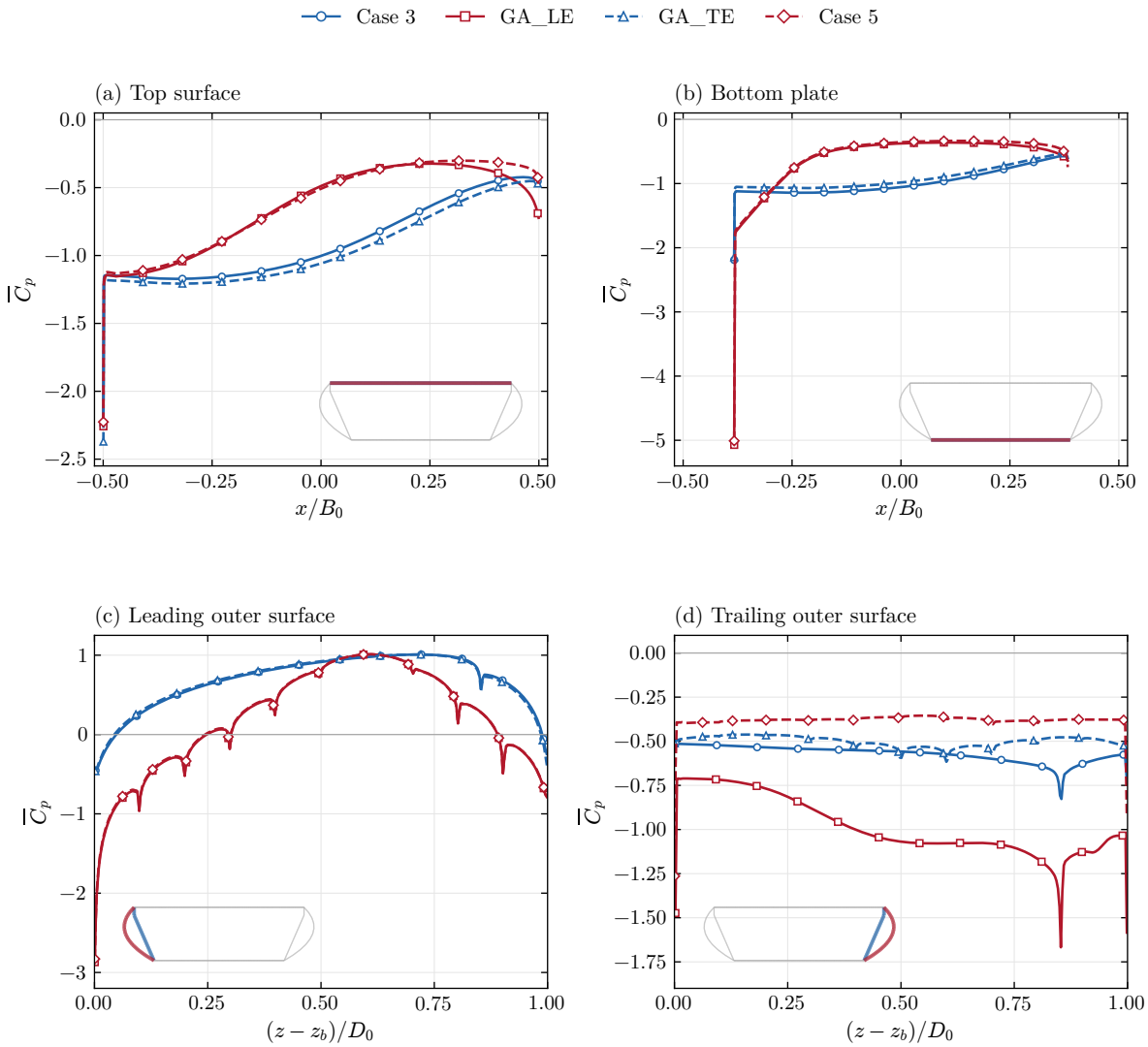


Fig. 9 Mean wall-pressure profiles for the four corners of set A, on M2 at maximum Courant number 1, all recovered over 60–120 s. (a,b) Top and bottom plate versus x/B_0; (c,d) leading and trailing outer surfaces versus local height $(z - z_b)/D_0$, including the short vertical slab-edge faces. Here $B_0 = 30$ m and $D_0 = D = 9.4$ m; z_b is each section's external bottom elevation. Blue/red denote inclined/curved leading edges, and solid/dashed lines denote inclined/curved trailing edges. The insets show the sampled surfaces on the actual Case 3 and Case 5 outlines. The outlines are aligned vertically for display. The curves connect all wall-face values without smoothing. Symbols are shown at selected faces only. The upstream pressure reference is defined in Appendix C. All profiles show the computed time-mean pressure

−0.627. The combined bottom-plate and cavity contribution is −0.720. The lift reversal combines the force on the newly exposed cavity walls with the removal of bottom-plate pressure and changes on the remaining surfaces.

Across all four corners, the pressure contribution to the lift interaction is −0.76545: −0.22452 from the top, −0.43985 from the bottom plate, −0.10134 from the cavity walls and +0.00026 from the two outer surfaces together. Adding the viscous interaction of +0.00048 gives the total interaction of −0.76497.

Changing the pressure reference or the surface partition changes the regional integrals. A constant pressure shift does not change their sum over the complete surface. Using the same 60–120 s window for all configurations changes the total drag interaction by 0.04% and the total lift interaction by 0.56% (Appendix C). The force accounting remains consistent across the surface partitions and averaging windows checked here.

4.4 Individual appendages

The supplementary tests examine corner rounding, lips and fins separately (Table 7). Rounding the convex corners of Case 3 with $r = 1$ m gives $C_d = 0.632$. This achieves about 94% of the drag reduction obtained from Case 3 to Case 5. Only one radius is tested, and the change also modifies the deck-edge contour. Removing the fins from Case 4 reduces drag by 38%. Removing its lips reduces drag by 14% but increases the moment about the stated reference point. None of the changes in lift RMS is resolved under the adopted allowances. Appendix H.1 gives

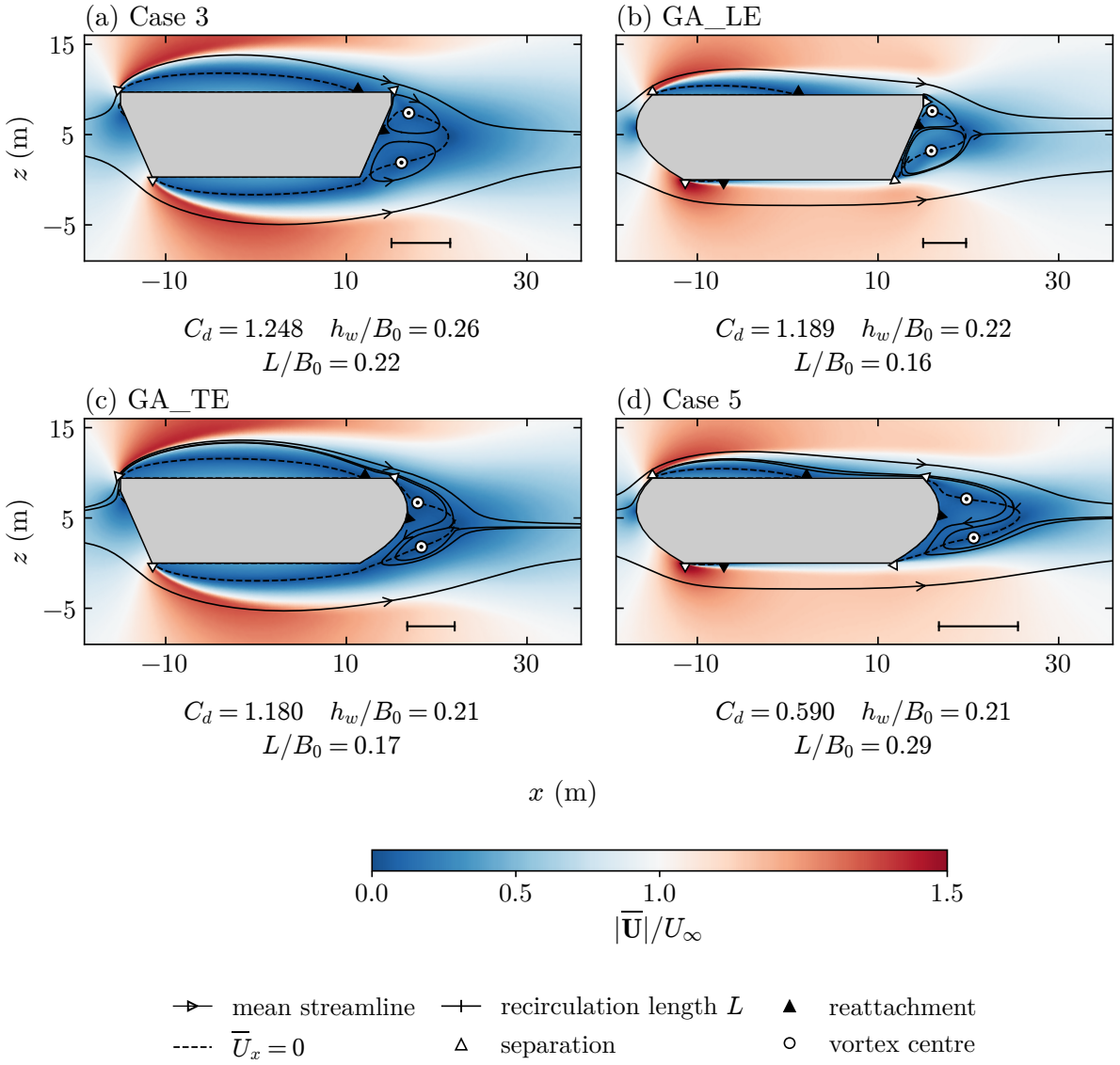


Fig. 10 Mean flow for the four configurations in set A, computed on M2 with a maximum Courant number of 1. The averaging window is 40–120 s, except for GA_LE, which uses 60–120 s. The left and right columns have inclined and curved leading edges. The top and bottom rows have inclined and curved trailing edges. All panels use the same colour scale for mean speed. Arrows show selected mean streamlines, and dashed lines show $\overline{U}_x = 0$. Open triangles show candidate separation points, and filled triangles show candidate reattachment points, identified from near-wall sign changes. Circles show mean vortex centres. Brackets show the recirculation length L. Below each panel are C_d, h_w/B_0 and L/B_0, where h_w is the reversed-flow height and B_0 = 30 m. The quantities are defined as in Fig. 5

the differences over matched time windows and the sequential comparison, whose step contributions depend on the order of the changes.

4.5 Configuration dependence

We also test how the loads change with angle of attack and traffic barriers. Case 5 has a lower drag point estimate at every angle tested. Its drag reduction is 54% at zero angle of attack, but the difference is unresolved at +10°. At negative and zero angles of attack, the time-step pairs at each angle give larger allowances than transferring only the fine-step result at zero angle would give (Appendix H.2). Cases 1 and 4 have no time-step checks away from zero angle of attack. The 5° spacing is too coarse to resolve local derivatives or determine aeroelastic stability.

With the same barriers fitted to Cases 1 and 5, the computed drag advantage of Case 5 is 40.4% for solid barriers and 46.4% for 50%-porous barriers. The two porosities produce opposite lift responses in Case 5, while the deflector of Case 4 shelters its barrier. These point estimates apply to the tested arrangements in a two-dimensional model that omits posts and spanwise flow. The local with-minus-without-barrier budget does not establish cancellation of global error or an uncertainty interval for the drag ratios (Appendix H.3). The exterior-skin screening index is retained only as an auxiliary calculation in Appendix H.5.

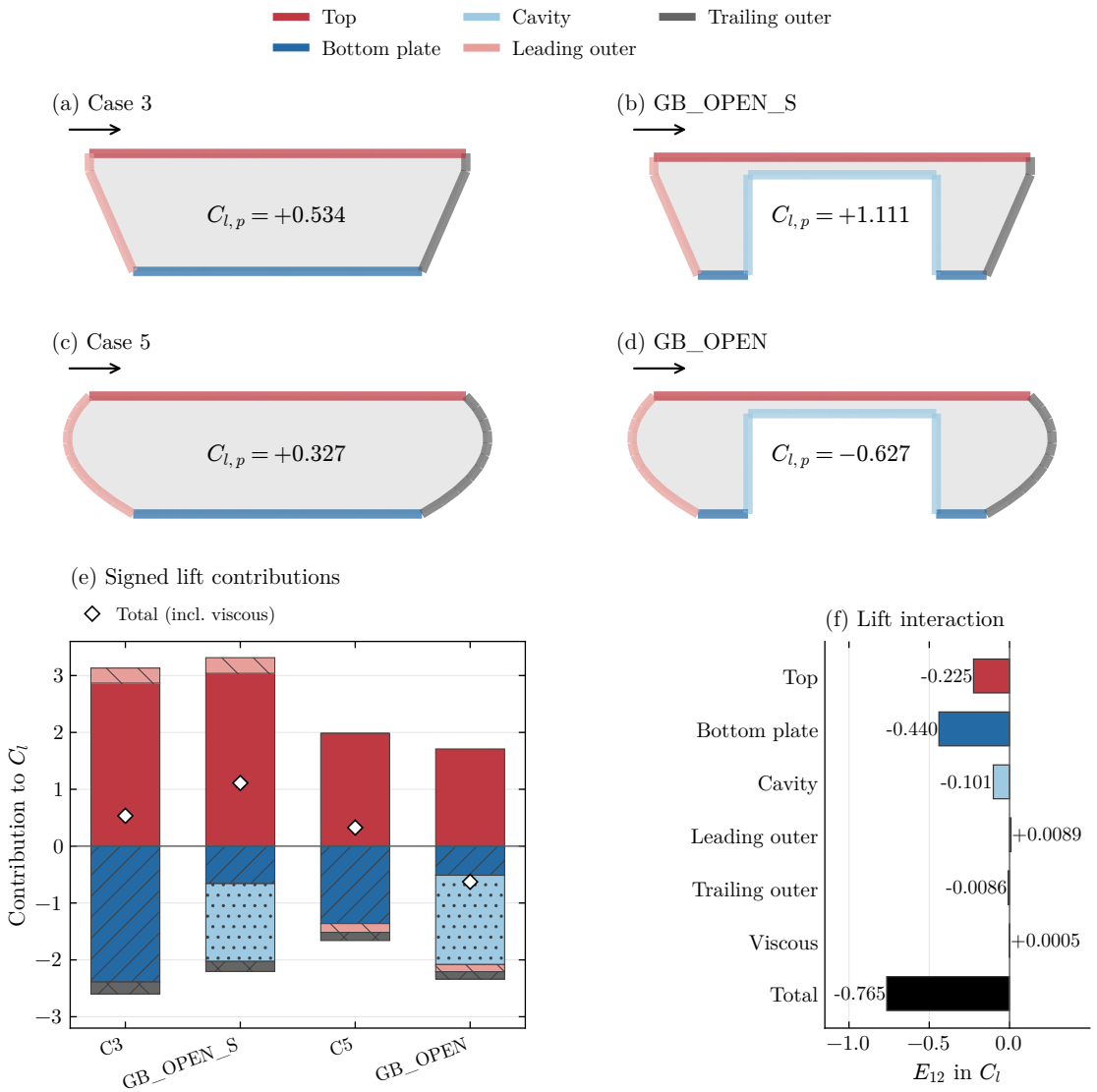


Fig. 11 Lift contributions for set B on M2 with a maximum Courant number of 1, averaged over 40–120 s. Panels (a–d) show the surface regions and integrated pressure lift. The columns compare closed and open cavities, and the rows compare the two edge shapes. In (e), positive and negative pressure contributions are stacked separately. Diamonds show total lift, including the small viscous contribution. Panel (f) gives the regional lift interactions, viscous contribution and total interaction. A region absent from a configuration contributes no force. No pressure is assigned to the open aperture. All configurations use the same upstream pressure-reference definition. The regional values describe the computed force distribution and have no independent uncertainty estimates

5 Discussion

5.1 How the appendages change the flow

Local load changes can be isolated from the total load by applying factorial comparisons and pressure integrals. In set A, curving the leading edge reduces windward pressure drag, but much of this reduction is offset by stronger trailing-surface suction when the trailing edge remains inclined. Curving both edges avoids the increase in trailing-surface drag. Most of the drag interaction comes from the trailing outer surface. In the separate comparison between Cases 1 and 5, most of the drag reduction comes from the windward surface. The set A interaction and the Case 1-to-Case 5 comparison use different baselines and pressure partitions.

Wake height alone does not explain the drag interaction in Fig. 10. The wake-height arguments of Roshko [41, 48] describe general bluff-body trends. Here, the surface-pressure integrals are needed to explain the interaction. The downstream profiles in Appendix D also show that a narrower velocity deficit does not necessarily mean faster recovery of the minimum wake velocity.

In set B, opening the curved-edge section exposes cavity walls and changes the flow over the remaining surfaces. The bottom-plate and cavity contributions to the lift change add to −0.720. The top surface contributes a

further −0.278. Both the underside and the top surface contribute to the lift reversal. The shear layer entering the open cavity is consistent with these computed pressure changes. Appendix H.4 gives further flow observations for all appendages.

5.2 Relation to previous interaction and rounding studies

Non-additivity has already been reported in bridge aerodynamics. Tesfaye et al. [9] showed departures from the superposition of motion- and gust-induced forces, while Zheng et al. [16] separated the effects of continuous shape parameters on flutter speed. The present study adds direct geometric contrasts from complete four-combination sets and accounts for these contrasts through a regional pressure-force budget that closes against the recorded forces. Zheng et al. [16] found that each second- and third-order interaction accounted for 2–6% of the flutter-speed variance; here the interaction accounts for 25% of the sum of squared effects for drag in set A and 37% for lift in set B (Table 8).

Chiarini and Quadrio [28] used mean-flow topology and velocity profiles to study small corner roundings of the BARC section at $Re_D = 3000$. Here, surface-pressure profiles and regional force integrals connect local flow changes to differences in total load. The $r = 1$ m variant provides a discrete comparison with the parent section. Geometry, Reynolds number and turbulence treatment differ from the BARC study, so the comparison concerns the connection between local flow changes and integrated loads.

5.3 Scope and limitations

The pressure-force analysis gives the surface contributions to load changes within the two-dimensional URANS configuration sets tested here. Applying these results to physical decks depends on how well the model predicts separation and reattachment. The approach-span discrepancy in Section 3.2.2 is one limitation. Tests of all four configurations under matched conditions would check the magnitude, sign and surface location of each factorial interaction. Tests of Cases 1 and 5 would check the overall drag reduction. The numerical allowances include grid and time-step sensitivities transferred from selected sections. These allowances describe the numerical sensitivities in the adopted budget. They do not include turbulence-model error or its correlation between geometries.

The simulated flow is uniform along the span. The model does not include spanwise decorrelation or three-dimensional structures in the cavity and wake [30, 49, 50]. The wall-function comparisons test how near-wall treatment changes separation on curved surfaces. The uniform inflow supplies modelled turbulence. It does not resolve large-scale turbulent motions that can affect reattachment [51]. The barriers are also represented as uniform along the span [12]. The tested deck is relatively deep. The comparisons use discrete shape levels and a single rounding radius. The results concern aerodynamic loads on fixed sections.

Near-wall tangential-velocity sign changes are flow-topology indicators. A windward sign change can mark stagnation; identifying reattachment additionally requires an upstream reversed-flow region. The regional pressure budgets identify the surfaces contributing to the computed interactions, defining the load components to examine in matched validation.

6 Conclusions

This study examined how edge shaping, cavity closure and other appendages change the wind loads on an idealised open twin-girder bridge deck, using two-dimensional URANS simulations with the k–ω SST model at $Re = 1.6 \times 10^7$. Five sections, from the bare deck (Case 1) to a fully streamlined closed section (Case 5), were complemented by seven variant sections that complete two 2×2 factorial sets and three single-feature variants. Integration of wall pressure over the meshed surfaces partitioned the pressure-force changes in the two factorial sets by surface region. The integrated pressure-drag and pressure-lift coefficients agreed with the recorded pressure-force histories to within 1.3×10^{-5}. Reported load coefficients and Strouhal numbers are accompanied by numerical allowances combining grid, time-step and statistical contributions, with a window-end contribution included for mean coefficients. The set-up was assessed against two girders of the Great Belt East Bridge and the BARC rectangular cylinder. The main findings are as follows.

1. Full streamlining reduces the drag of the bare deck by 54% (±1.1 percentage points), lowers the mean lift and moment to 23% and 39% of their baseline values and raises the Strouhal number from 0.138 to 0.214. The reduction comes from a decrease in pressure drag, with the windward faces accounting for 85% of the pressure-drag reduction. The rounded nose confines stagnation pressure to a small region and turns the flow around the edges, where strong suction develops, while the base pressure rises by only 0.12.
2. Encasing the girders, closing the cavity or adding edge deflectors changes the drag of the bare deck by at most 3.1%. Closing the cavity (Case 3) reduces the mean lift to about 38% of its baseline value and raises the lift

RMS about fivefold; the deflectors (Case 4) lower the moment by 17% and raise the lift RMS about fourfold. Under the adopted numerical allowances, neither the drag changes in Cases 2–4 nor the lift-RMS increase in Case 4 is resolved. The lift-RMS increase in Case 3 exceeds its allowance.

3. Relative to the closed section with inclined edges, curving either edge alone gives a point estimate of about 5% drag reduction. Curving both edges gives about 53%. These reductions are not additive: non-additivity accounts for an estimated 81% of the combined reduction. The drag interaction exceeds the numerical allowance calculated for independent errors and the dependence sensitivity scale. The trailing outer surface accounts for almost all of this interaction. Curving the leading edge alone reduces its pressure-drag contribution from 0.679 to 0.197. With the trailing edge still inclined, the trailing contribution rises from 0.573 to 0.986 and offsets most of that reduction. With both edges curved, the leading contribution is 0.204 and the trailing contribution is 0.380.
4. Opening the cavity increases the mean lift from 0.534 to 1.110 with inclined edges. With curved edges, it reverses the mean lift from +0.326 to −0.627. For the curved-edge section, the bottom-plate and cavity contributions to the lift change add to −0.720. The top surface contributes a further −0.278. The outer surfaces and viscous forces give smaller contributions. For drag in set B, edge shape accounts for 99% of the sum of squared factorial effects.
5. Among the single-feature variants, rounding the convex corners of Case 3 with $r = 1$ m gives about 94% of the drag reduction obtained from Case 3 to Case 5. Removing the bottom fins of Case 4 reduces its drag by 38%. Removing its deflector lips reduces drag by 14% and increases the moment.
6. The benefit of streamlining depends on incidence and on the deck equipment. Relative to Case 1, the drag of Case 5 is 57% lower at −5°, 54% at 0°, 36% at −10° and 26% at +5°; at +10° the three sections reach almost the same drag ($C_d = 1.70$–1.77). At +10°, the drag difference between Cases 1 and 5 is unresolved under the adopted screening allowances. With the same traffic barriers on both sections, the drag advantage is 40.4% for solid and 46.4% for 50%-porous barriers. These barrier drag-reduction ratios are point estimates for the tested two-dimensional arrangements.
7. The drag ordering of the bare and streamlined sections is the same under changes in inlet turbulence, sustaining terms, Reynolds number, turbulence closure and far-field conditions; the realizable k–ε model gives a larger reduction than SST (63% against 52%, both at a maximum Courant number of 2). On the benchmarks, the set-up reproduces the mean drag, Strouhal number and reattachment length of the BARC rectangle within the spread of the numerical contributions to the benchmark, and the lift slope of the Great Belt suspension-span girder to within 2–3%. For that girder it overestimates the moment slope by 24–55% and gives less than half of the measured drag at 0° and a mean lift of 0.35 instead of nearly zero; on the approach-span girder the bottom-plate flow stays separated, with a drag of 0.761 and a Strouhal number of 0.176 against the measured 0.60 and 0.22.

These results show that the parts of a fairing on an open twin-girder deck should be assessed together rather than one at a time: much of the local drag reduction from a curved leading edge is offset when the trailing edge remains inclined; curving both edges avoids this offset. Complete factorial sets and a surface-pressure budget that closes against the recorded forces directly identify the contributions to these geometric interactions. This approach can also be applied to other bluff sections. A wind-tunnel test of the four corners of set A would provide the matched experimental counterpart of the computed trailing-edge interaction.

Statements and Declarations

Funding

This research received no external funding.

Competing interests

The authors declare no competing interests.

Author contributions

Mingjin Lou: research design, simulations, data analysis, software, and writing. Yize Zhang: simulations and writing. Ze Tao: supervision and manuscript revision. All authors approved the manuscript and its submission.

Data availability

The data that support the findings of this study are available from the corresponding author upon reasonable request.

Appendix A Simulation input summary

Tables 9–11 summarise the simulation settings, run durations and accepted force and field windows (Section 2.9).

We checked the saved solver logs for seven distinct runs over their accepted time windows. These runs cover the comparison between the bare and streamlined sections and both factorial sets. At each time step, the final pressure solve had a residual no greater than 10^{-7}. The maximum final residual was 6.22×10^{-9} for velocity and 4.36×10^{-9} for k, ω. After the final pressure solve, the largest local continuity error recorded in the logs was 2.41×10^{-14}. All linear solves in these windows took 57 iterations or fewer. These checks do not estimate the remaining PIMPLE iteration error in the computed loads.

Table 9 Settings of the deck simulations

Parameter	Value	Note
Solver	OpenFOAM v2506, `pimpleFoam`	Incompressible, transient
Turbulence model	k–ω SST	With `decayControl` ($k_\infty = 2.34\ \mathrm{m^2/s^2}$, $\omega_\infty = 4.23\ \mathrm{s^{-1}}$)
Time scheme	`backward`	Second order
Convection	`bounded Gauss linearUpwind` (U); `bounded Gauss limitedLinear 1` (k, ω)	
Gradients; Laplacian	`cellLimited Gauss linear 1`; `Gauss linear limited corrected 0.5`	
PIMPLE	3 outer corrector iterations, 2 pressure correctors, 1 non-orthogonal corrector	No under-relaxation
Linear solvers	GAMG: p tolerance 10^{-7}, relative tolerance 0.01 (final: 0); `smoothSolver`: U, k, ω tolerance 10^{-8}, relative tolerance 0.05	Configured stopping criteria; symmetric Gauss–Seidel smoother
Time step	$\mathrm{Co}_{\max} = 2$, $\Delta t \leq 0.01$ s	$\Delta t \approx 0.85$–1.1 ms; $\mathrm{Co}_{\max} = 1$ for Case 5, its angle-of-attack series and the variant sections
Initial field	Steady SIMPLE solution, 6000 iterations	Not used for results; uniform inflow state for the runs listed in Section 2.6
Duration; averaging	160 s; from 40 s	Angle-of-attack series of Case 5 and variant sections: 120 s; exceptions in Table 10
Inflow	$U_\infty = 25$ m/s, $I = 5\%$, $\ell = 0.66$ m	$Re = 1.6 \times 10^7$
A_{ref}, L_{ref}	9.4 m^2, 9.4 m	All sections
Moment point	Centre line, 1.92 m below the deck surface	All sections; positive nose up

Table 10 Runs with a longer duration or a later statistical window than the standard schedule. The standard window is 40–160 s, or 40–120 s for the Case 5 series at different angles of attack and the variant sections

Run	Duration (s)	Window (s)	Reason
Case 2	250	100–250	Cycle means still drifting after 40 s
Case 1, $\alpha = +5°$	160	60–160	Cycle means still drifting after 40 s
Case 5, 20 mm first layer	160	80–160	Drag still rising at 40 s
GA_LE	120	60–120	Start-up transient until about 55 s
GC_NOLIP	120	60–120	Mean lift settling with a time constant of about 20 s
Case 5, $\alpha = 0°$, angle-of-attack series	120	60–120	Drag settling slowly after the uniform start
Case 4, $\alpha = -10°$	320	160–320	Wake changed state within the first 160 s
Case 1, inflow intensity 1.6% and without sustaining terms	320	160–320	Still drifting at 160 s
Great Belt suspension-span girder, $\alpha = +4°$	240	150–240	Forces oscillating with a period of two time steps until about 145 s

Table 11 Force and field averaging windows for the repeated main and variant sections. All times are in seconds. The primary and variant runs use the M2 grid with slip conditions at the top and bottom boundaries. Runs at different angles of attack use free stream boundary conditions on all four outer boundaries. Each series uses its own reference run at 0° with the same boundary conditions (Section 2.7). The force averaging windows for these runs are given in Table 10, and the field averaging windows in Appendix H.2. The table shows which comparisons use the same geometry and which use the same data

Data group	Maximum Co	Force window	Field window
Primary Cases 1, 3, 4	2	40–160	40–160
Primary Case 2	2	100–250	40–160
Primary Case 5	1	40–160	40–160
Matched parents and variants, except below	1	40–120	40–120
GA_LE, GC_NOLIP	1	60–120	60–120
Case 4 parent for GC_NOLIP	1	60–120	40–120
Barriers (fields shown for Cases 1, 5)	2	40–160	40–160
Case 1 porous-barrier field	2	40–160	40–150

The force comparison for GC_NOLIP uses its parent over 60–120 s. The parent flow panel uses 40–120 s. For Case 5, the barrier reference runs use maximum Courant numbers of 1 or 0.5, as listed in Appendix H.3. The primary flow and pressure panels for Case 2 use the earlier field window. Agreement in mean drag does not establish stationarity of every field quantity. The additional field panels for the angle and barrier tests are qualitative flow diagnostics. The quantitative pressure closure uses the factorial runs.

Appendix B Coefficients based on the projected height

Table 12 gives the mean forces and coefficients normalised by each section's maximum projected height H_i.

Table 12 Projected height H_i, mean forces per metre span on M2 and coefficients based on H_i at $\alpha = 0°$ ($C_{d,H} = C_d D/H_i$, $C_{l,H} = C_l D/H_i$)

Section	H_i (m)	$\bar{F}_x$ (N/m)	$\bar{F}_z$ (N/m)	$C_{d,H}$	$C_{l,H}$
Case 1	9.4	4 639	5 016	1.284	1.388
Case 2	9.4	4 579	4 553	1.267	1.260
Case 3	9.4	4 494	1 886	1.244	0.522
Case 4	12.3	4 568	5 041	0.966	1.066
Case 5	9.4	2 131	1 173	0.590	0.325

Appendix C Wall-pressure closure and matched windows

We integrate the stored wall values of `pMean` with the mesh face area vectors. Pressure is not interpolated from cell centres to the wall. With kinematic pressure $p_k = p/\rho$ and $\boldsymbol{S}_f$ directed out of the fluid into the body, the regional coefficient vector is

$$\boldsymbol{C}_{p,R} = \frac{1}{\frac{1}{2}U_\infty^2 A_{\mathrm{ref}}} \sum_{f \in R} (\overline{p}_{k,f} - \overline{p}_{k,\infty}) \boldsymbol{S}_f, \qquad A_{\mathrm{ref}} = 9.4\,\mathrm{m}^2 \tag{C1}$$

for the 1 m span. The reference pressure is the arithmetic mean of stored cell values satisfying $x_{\mathrm{cell}} < \min(x_{\mathrm{cell}}) + 20$ m and $|z_{\mathrm{cell}} - 5\,\mathrm{m}| < 20$ m. All six sections use the same selection rule with the corresponding time window. Top faces have both endpoints at the slab top. Bottom faces have both endpoints at the external bottom elevation. Both checks use a tolerance of 2×10^{-5} m. In open sections, the cavity contains the inner walls at $|x| \le 7.5$ m and the slab underside. Other outer faces are assigned to the leading ($x < 0$) or trailing ($x \ge 0$) side. The maps in Fig. 11 include every wall face once.

The `fieldAverage` counters record about 20 s of averaging at 60 s and 80 s at 120 s. The offsets from the nominal 40 s start are 0.00043–0.00058 s, and the counters differ by 60 s. They confirm that averaging continued across restarts. We recover the 60–120 s mean as $(T_{120}\overline{p}_{120} - T_{60}\overline{p}_{60})/(T_{120} - T_{60})$, where $\overline{p}_t$ is the saved cumulative mean and T_t is its accumulation duration. Both fields use the same mesh. Force records are merged by their actual time ranges and integrated with the trapezoidal rule and interpolated endpoints. The result is divided by $\frac{1}{2}\rho U_\infty^2 A_{\mathrm{ref}}$, with $\rho = 1.23$ kg/m^3 and $U_\infty = 25$ m/s.

Tables 13 and 14 give the comparison with pressure-force records and the common-window check. The largest absolute difference is 1.26×10^{-5} across the accepted and common windows. The sum of the regional integrals differs from the full surface integral by no more than 6×10^{-15}. Adding a constant to the pressure leaves the full integral unchanged to rounding accuracy. Using the outlet pressure as the reference changes the set A trailing interaction from −0.2667 to −0.2596. The complete pressure interaction is unchanged. The pressure reference must be stated with the regional values. These accounting residuals do not estimate discretisation or model uncertainty.

Table 13 Wall-pressure closure over the accepted windows. $C_{d,p}$ and $C_{l,p}$ are the integrated wall values. The difference Δ is the wall integral minus the time-averaged pressure-force record, in units of 10^{-6}

Section	Window (s)	$C_{d,p}$	$C_{l,p}$	$10^6\Delta C_{d,p}$	$10^6\Delta C_{l,p}$
Case 3	40–120	1.251931	0.534139	−3.86	−5.37
GA_LE	60–120	1.183334	0.095241	−0.16	−12.55
GA_TE	40–120	1.183984	0.879139	−2.61	+0.43
Case 5	40–120	0.584533	0.327244	+0.02	−1.23
GB_OPEN_S	40–120	1.156763	1.111002	−2.01	+0.05
GB_OPEN	40–120	0.585764	−0.626795	−0.66	−3.24

Table 14 Changes in the principal total-force interactions when all runs use a common window. The accepted windows are those in Table 7. The last column gives the absolute change relative to the magnitude from the accepted window; it is not an uncertainty estimate

Interaction	Accepted	60–120 s	Change (%)
Set A, C_d	−0.265622	−0.265512	0.041
Set B, C_l	−0.764970	−0.769225	0.556

Appendix D Set A wake profiles

Fig. 12 shows mean streamwise velocity at $\xi_w = (x - x_{\mathrm{TE}})/D_0$. Here, x_{TE} is the physical trailing extremity of each section and $D_0 = D = 9.4$ m. Height is measured relative to $z_m = (z_t + z_b)/2$. We obtain the profiles by linear interpolation of the stored cell-centre means. All sample points are downstream of the solid and inside the domain. The windows match the accepted mean-flow comparisons: 40–120 s, except for GA_LE, which uses 60–120 s. These fields were not recovered over a common window, as the wall-pressure profiles were. No separate numerical or statistical uncertainty is estimated for the profiles. At $\xi_w = 1$, the minimum $\overline{U}_x/U_\infty$ is about 0.17 for Case 3 and 0.03 for Case 5. These local values do not determine the integrated wake momentum deficit or the distance needed for wake recovery.

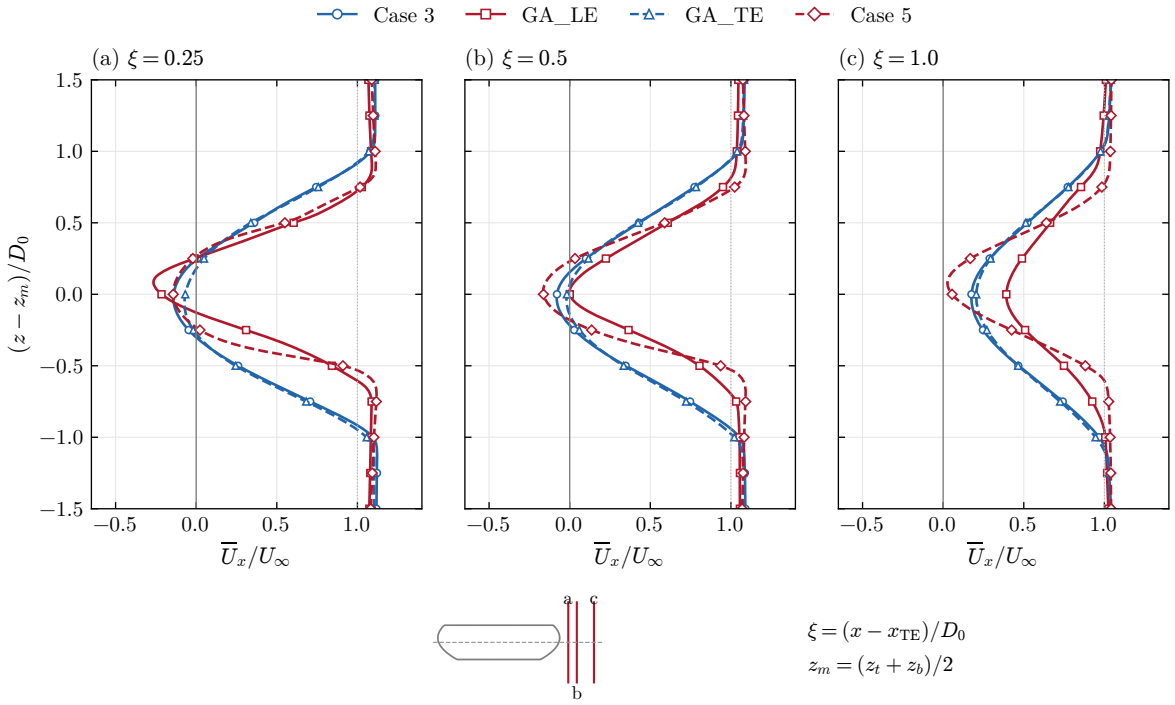


Fig. 12 Mean streamwise-velocity profiles for set A on M2 with a maximum Courant number of 1. The stations are (a) $\xi_w = 0.25$, (b) $\xi_w = 0.5$ and (c) $\xi_w = 1$. The labels ξ in the figure denote ξ_w as defined here. The inset shows the stations for Case 5; each section uses its own x_{TE} and mid-height. Colours and line styles follow Fig. 9. Lines show linear interpolation of the stored mean fields, with symbols at selected points. The averaging window is 40–120 s, except for GA_LE, which uses 60–120 s. These are descriptive CFD comparisons; experimental profiles and profile uncertainty bars are not shown

Appendix E Statistical convergence of all five sections

Figs. 13–14 give the seven running statistics and residuals defined in Section 3.1.4. The accepted windows contain 43 complete lift cycles for Case 1, 55 for Case 2, 53 for Case 3, 46 for Case 4 and 68 for Case 5. Each running-value axis includes the initial change within the accepted window. Residuals below 10^{-4}% are not truncated. The captions give the averaging windows and line conventions.

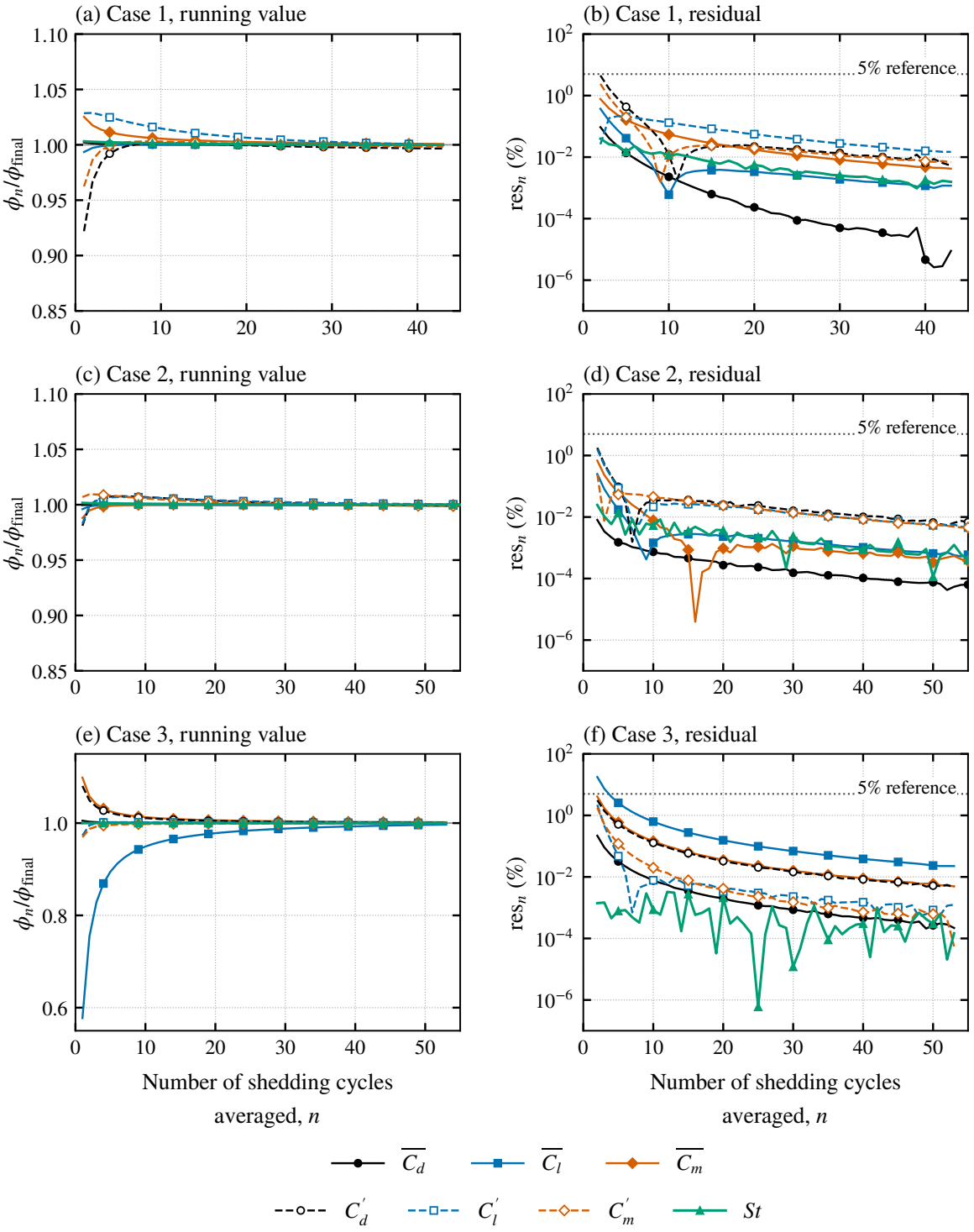


Fig. 13 Statistical convergence for Cases 1–3 on M2. The left panels show running statistics divided by their values over the full window. The right panels show cycle-increment residuals. The windows are 40–160 s for Cases 1 and 3 and 100–250 s for Case 2. All panels use the same symbols and colours

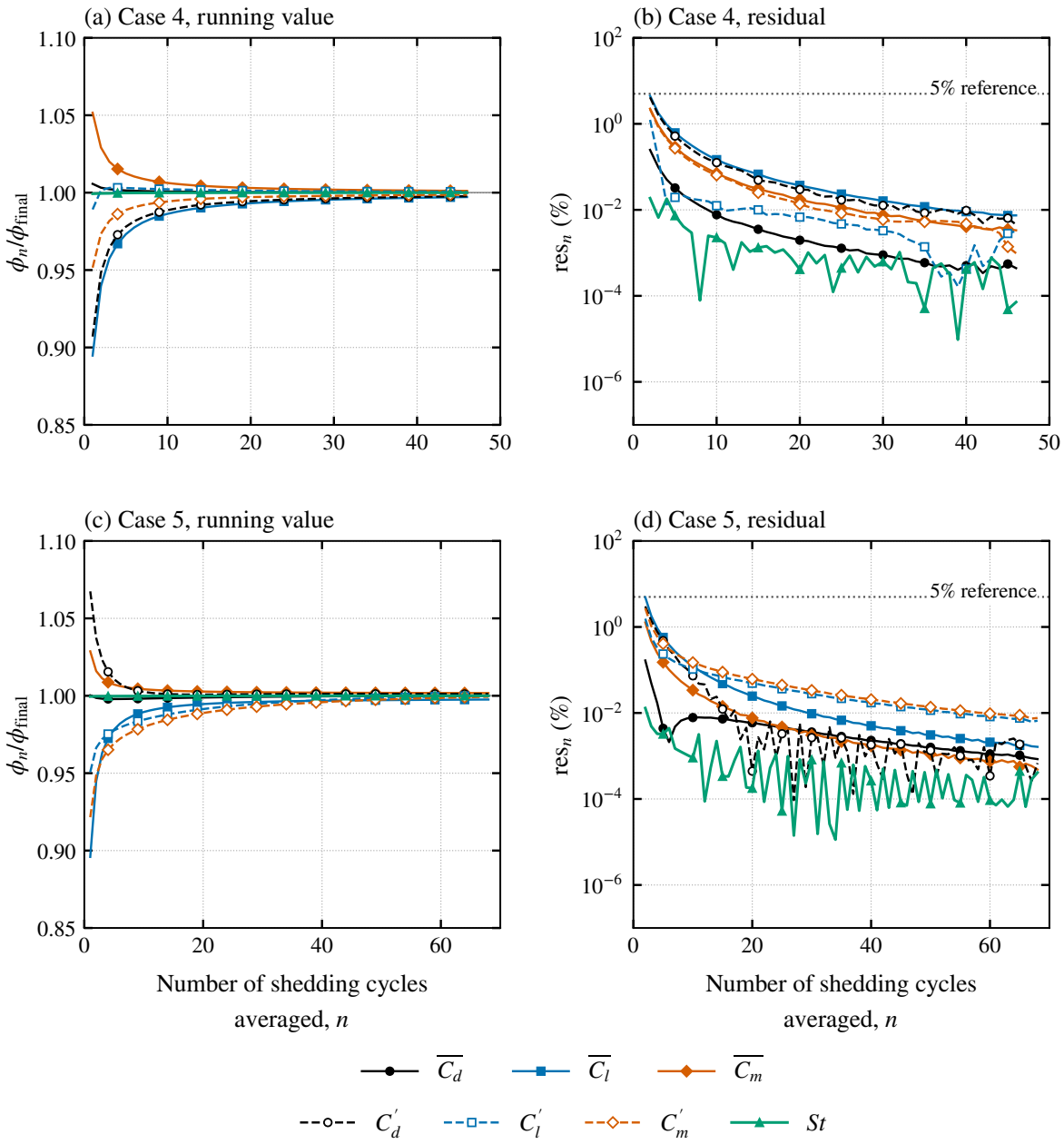


Fig. 14 Statistical convergence for Cases 4 and 5 on M2 over 40–160 s; Case 5 uses a maximum Courant number of 1. The left panels show running statistics divided by their full-window values. The right panels show cycle-increment residuals, including the small variations in Strouhal number. Definitions and line conventions follow Fig. 13

Appendix F Instantaneous wake contours

Figs. 15–16 show the instantaneous near-wake vorticity and SST model fields. The captions specify the snapshot selection, normalisation and time-step settings.

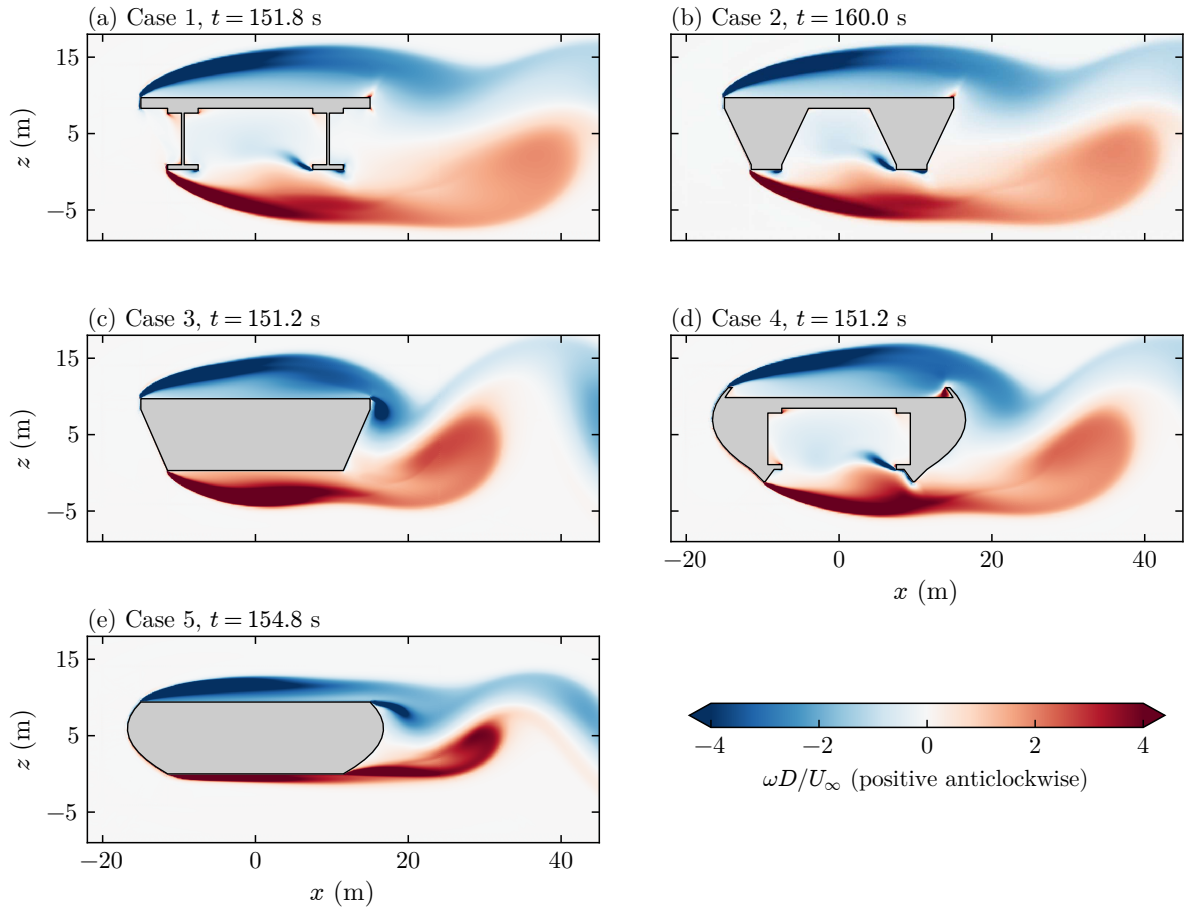


Fig. 15 Instantaneous spanwise vorticity $\omega D_0/U_\infty$ in the near wake of all five sections on M2. Each snapshot is taken at a lift maximum within 144–160 s, at the time given in the panel. The maximum Courant number is 1 for Case 5 and 2 for Cases 1–4. Colour limits and the sign convention follow Fig. 6

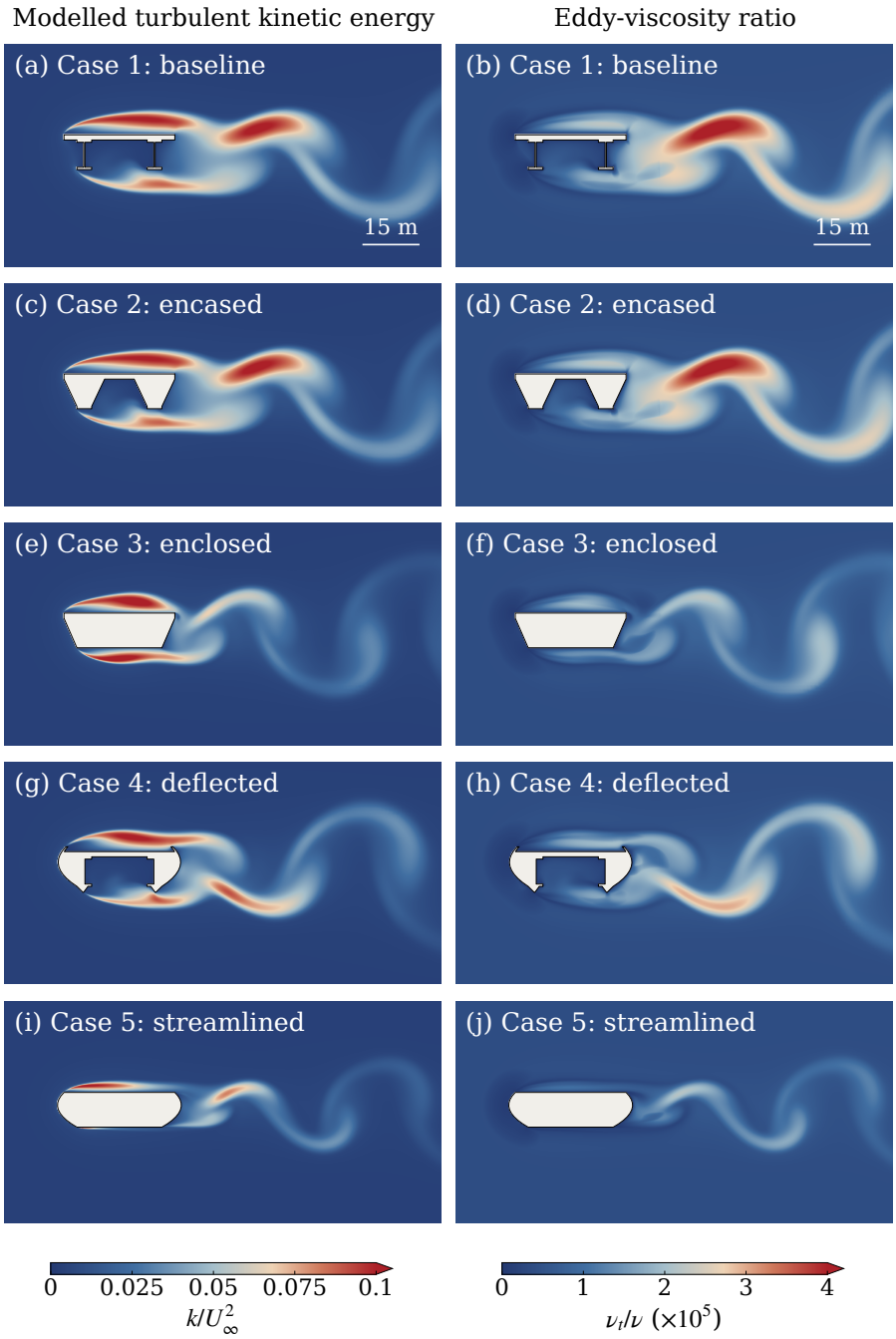


Fig. 16 Instantaneous SST model fields at $t = 160$ s for the five baseline sections. Rows show Cases 1–5. The left column (a,c,e,g,i) gives modelled turbulent kinetic energy k/U_∞^2, and the right column (b,d,f,h,j) gives the eddy-viscosity ratio ν_t/ν. Each column uses the same colour scale for all cases. The upper limits are 0.10 for k/U_∞^2 and 4×10^5 for ν_t/ν; triangles on the colour bars indicate saturation. All panels use the same spatial scale and M2 grid level. The maximum Courant number is 2 for Cases 1–4 and 1 for Case 5. The snapshots use the same simulation time, but they are not matched by shedding phase or averaged over time. Modelled k excludes the energy of the resolved URANS fluctuations

Appendix G Modelling and benchmark details

G.1 Barrier geometry and paired sensitivity budget

We add traffic barriers to Cases 1, 4 and 5 to check whether their load ranking changes. The barrier height is $H = 1.0$ m above the deck, the minimum vehicle-parapet height in the Design Manual for Roads and Bridges (DMRB) standard CD 377 Revision 4 (2021) [52]. Two porosities are modelled: a solid barrier and a porous barrier with an open-area ratio of 50%, typical of the barriers tested by Nicese et al. [12], Đuranović et al. [26] and López-Nuñez et al. [13]. In the two-dimensional model the porous barrier consists of two rails of height $0.25H$ separated by gaps of $0.25H$, with the lowest $0.25H$ open; posts are not represented. We chose this opening arrangement because Đuranović et al. [26] reported little sensitivity to opening count at fixed porosity. The two-dimensional

open-area ratio is not established as equivalent to that of a three-dimensional barrier with posts. The rail thickness (0.10 m) and the setback from the deck edge (0.15 m) are modelling choices. On Cases 1 and 5 the barriers stand at the deck edges; on Case 4 they stand inboard of the edge deflector, whose lip already rises 1.3 m above the deck, so that the barrier is partly sheltered. The Case 4 results include the shelter provided by the deflector lip and apply to this barrier arrangement as a whole. The barrier is a separate wall patch, so that its forces and those of the deck are reported separately.

Because the gaps between the rails (0.25 m) are only about twice the prism-layer thickness, each barrier grid is checked for gap cells, layer coverage, barrier y^+ and the quality limits of Section 2.8. Further local refinement on porous Case 1 changed total drag by 2% and barrier drag by 14%; all barrier runs use the finer level. For each of the six barrier configurations, the absolute difference between its coarser and finer local grids (refinement levels 5 and 6, denoted RL5 and RL6) over 40–80 s gives U_{mesh}. The exception is St for porous Case 1: its 40–80 s crossing estimate is unstable, so the available 40–160 s pair is used. These allowances cover local refinement. They do not estimate the error from the unchanged global grid. Where layers do not cover the barrier (most of the solid barrier of Case 5), viscous force is below 0.05% of barrier drag and 1.5% of barrier lift. This small direct viscous contribution does not bound the pressure or separation error caused by missing layers.

For $E = \phi_{\mathrm{with}} - \phi_{\mathrm{without}}$, the local sensitivity budget is $U_{\mathrm{loc}} = (U^2_{\mathrm{mesh}} + U^2_{\Delta t} + U^2_s + U^2_w)^{1/2}$. For Cases 1 and 4, $U_{\Delta t}$ is the bare-section difference between maximum Courant numbers 2 and 1 over 40–160 s; the procedure for Case 5 is given below. For this paired contrast, $U^2_s = U^2_{s,\mathrm{with}} + U^2_{s,\mathrm{without}}$ and $U^2_w = U^2_{w,\mathrm{with}} + U^2_{w,\mathrm{without}}$, with each term computed over its own 40–160 s force record using Section 2.9. The statistical terms are combined independently; this assumption does not imply cancellation of spatial or model error. No separate endpoint term is assigned to C'_l or St. An effect above U_{loc} exceeds the sensitivities tested here. This alone does not bound the remaining error. This budget does not estimate the remaining global-grid error in the paired difference. Using M2 for both runs does not demonstrate that this error cancels. It is neither a confidence interval nor a total numerical or model-error bound.

The fine cells around the barrier also limit the time step. Cases 1 and 4 with barriers are compared with the runs without barrier at the same maximum Courant number of 2. For bare Case 5, the largest Courant number occurs at the windward lower corner. At this corner it falls to 1.24 with the solid barrier and 0.46 with the porous barrier. We compare the solid-barrier runs with the bare runs at a maximum Courant number of 1. The porous-barrier runs use the bare reference at 0.5. The Case 5 baseline time-step allowance uses the absolute bare-section difference between maximum Courant numbers 1 and 0.5 over 40–160 s. For the solid barrier it is the larger of that difference and 0.2365 times the bare-section difference between 2 and 1. The second value is an unvalidated linear interpolation in the corner Courant number, based on the sampled value 1.2365 at 40 s. On Case 5 the change of grid level also changes the time step, so its U_{mesh} contains part of the time-step effect. Adding U^2_{mesh} to $U^2_{\Delta t}$ may count part of the time-step response twice. These terms are not independently measured error sources.

Cases 1, 4 and 5 without barriers are also computed at angles of attack $\alpha = -10°$, $-5°$, $0°$, $+5°$ and $+10°$ (positive nose up) by rotating the inflow.

G.2 Initialisation and run duration

Except for the runs identified below, initialisation uses a steady SIMPLE solution on the same mesh with the same schemes [53]. These steady solutions do not converge for the bluff sections (the lift of Case 1 oscillates by more than twice its mean), so they are used only as initial fields and no result is taken from them. In a few runs with `freestream` outer boundaries, the steady wake carried an eddy viscosity several times the inflow value, or a peak of k, to the outlet. The transient runs then diverged early and developed large reversed flow through the outer boundaries. These runs (Case 1 at $\alpha = -5°$, Case 4 at $\alpha = \pm 5°$, the Great Belt suspension-span girder at $+4°$ and the approach-span girder with 5% inflow turbulence; Section 3.2) were restarted from a uniform field equal to the inflow state, with all other settings unchanged. The control-grid run of the suspension-span girder also uses a uniform inflow start. Its run from the steady field developed pressure oscillations with a period of two time steps. The entire Case 5 angle-of-attack series uses the same uniform start. For Case 1 at $\alpha = 0°$, both starts were tested: the mean coefficients differ by less than 0.25%, and C'_l differs by 1.8%. Unless stated otherwise in Section 2.9, each run covers 160 s of physical time. On 16 CPU cores, a run on M2 at a maximum Courant number of 1 took about 9–13 h of wall-clock time for 120 s of physical time.

G.3 Boundary conditions and mesh acceptance details

Tables 15 and 16 list the boundary conditions and grid statistics.

Table 15 Fluid properties and boundary conditions of the deck simulations

Boundary	Variable	Condition
Fluid	ρ, ν	1.23 kg/m^3, 1.46×10^{-5} m^2/s
Inlet	U	`freestreamVelocity`, 25 m/s
Inlet	p	`freestreamPressure`
Inlet	k, ω	`freestream`, 2.34 m^2/s^2, 4.23 s^{-1} ($I = 5\%$, $\ell = 0.66$ m)
Outlet	U; p	`zeroGradient`; `freestreamPressure` ($p_\infty = 0$)
Outlet	k, ω	`zeroGradient`
Deck	U	`noSlip`
Deck	ν_t, k, ω	`nutkWallFunction`, `kqRWallFunction`, `omegaWallFunction`
Top, bottom	U; p, k, ω	`slip`; `zeroGradient`
All outer, angle-of-attack series	all	as inlet, with $\mathbf{U}_\infty = U_\infty(\cos\alpha, 0, \sin\alpha)$
Front, back	all	`empty`

Table 16 Grid statistics at the end of each run. N_c is the number of cells, $\theta_{\max}$ the maximum non-orthogonality and $s_{\max}$ the maximum skewness. The table also gives the area-weighted mean and 95th percentile of y^+, with area fractions $A_{>300}$ for $y^+ > 300$ and $A_{<30}$ for $y^+ < 30$

Section, grid	N_c	$\theta_{\max}$ (°)	$s_{\max}$	$\overline{y^+}$	y^+_{95}	$A_{>300}$	$A_{<30}$
Case 1, M2	157 427	52.4	2.31	103	199	0.6%	5.5%
Case 2, M2	141 627	58.0	2.31	134	200	0.1%	0
Case 3, M2	132 190	43.4	2.31	183	240	0.4%	0
Case 4, M2	151 390	58.7	2.31	138	255	3.2%	4.3%
Case 5, M2	131 243	35.8	1.05	202	300	5.7%	0
Case 1, M1	86 650	46.4	2.35	105	195	0.7%	2.7%
Case 3, M1	71 553	42.8	2.34	181	233	0.5%	0
Case 5, M1	71 383	32.8	1.09	195	295	5.2%	0
Case 1, M3	294 049	58.2	2.02	103	187	0.7%	6.2%
Case 3, M3	249 876	53.8	1.99	184	245	0.8%	0
Case 5, M3	248 558	47.3	1.01	202	301	6.2%	0
GA_LE, M2	131 939	44.7	2.29	221	300	5.9%	0
GA_TE, M2	131 948	44.7	2.29	176	234	0.4%	0
GB_OPEN_S, M2	146 088	46.5	2.30	130	212	0.1%	1.3%
GB_OPEN, M2	144 780	46.5	2.30	187	297	4.9%	0.2%
GC_NOLIP, M2	149 890	58.7	2.31	136	241	2.2%	2.9%
GC_NOFIN, M2	151 811	56.8	3.23	151	290	4.3%	3.5%
GD_ROUND, M2	132 124	26.6	0.40	211	275	4.3%	0

The target mesh checks are listed below; the exceptions retained in this study are described afterwards. All points must lie on the two spanwise planes. The number of `empty` faces must equal twice the number of cells. The mesh must pass `checkMesh`, with maximum non-orthogonality below 65° and maximum skewness below 4. We also check the prism layers face by face, because the `snappyHexMesh` summary can hide local layer collapse. A wall face counts as layered when the wall-normal height of its cell is at most 1.5 times the first-layer thickness. The target is coverage of at least 98% of the wall length and complete coverage of every straight wall segment. Faces within 0.22 m of a corner are excluded from the straight-segment check. This check uses the first cell and does not establish the quality of the full prism-layer stack. Run in parallel, `snappyHexMesh` is not deterministic: identical inputs can give slightly different grids, and the layers collapse in different places. A grid that fails the layer check is regenerated with unchanged parameters, up to three times. The first M3 grid of Case 1 had no layers on 8.9% of the wall, on the leeward girder; it was regenerated, and all M3 results of Case 1 are from the regenerated grid. An analysis of the surface pressure on the unlayered faces of the first grid gives local contributions of 1.4% of mean drag and 0.2% of mean lift. These do not bound the global pressure-field response to missing layers. The M2 grids of Cases 2 and 4 were used before the layer check was introduced. Their layer coverage is 97.7% for Case 2 and 97.3% for Case 4. The gaps, each 0.2–0.3 m long, lie at concave girder corners and remained after three regenerations. These grids are retained. The GC_NOLIP grid has layers on 98.3% of the wall. Two gaps, 0.19 and 0.31 m long, lie at the same concave corners as in Case 4 and leave 99.5% of the straight segments layered. Three regenerations reproduced these gaps exactly, so this grid is also retained. Grid statistics and source

identifiers are retained in the post-processing records. The wall distance is reported at the end of each run, with a target of $30 \leq y^+ \leq 300$. Table 16 summarises the grids. The non-orthogonality and skewness limits are met, but the y^+ target is not met on every face. In Case 1, $y^+ < 30$ over 2.7–6.2% of the wall area, at girder corners and beneath the slab. In Case 4, the corresponding area is 4.3%, and one face reaches $y^+ = 1878$. No wall faces in Cases 2, 3 and 5 have $y^+ < 30$. The area with $y^+ < 30$ ranges from 0.2–3.5% for GB_OPEN, GB_OPEN_S, GC_NOLIP and GC_NOFIN. These mesh statistics are given for each section because mesh quality can affect the computed loads [31].

G.4 Near-wall configuration sensitivity

Fig. 17 shows y^+ around Cases 1 and 5 on M2. On Case 1 it lies between 30 and 300 on most of the wall; it falls below 30 in the concave corners of the girders and under the slab, and it exceeds 300 only at the windward edge of the slab and at the windward lower flange, where it reaches 568. On Case 5 it exceeds 300 on the lower windward fairing, with a maximum of 423 at its lower knuckle, and near the upper windward corner, and it is nowhere below 30.

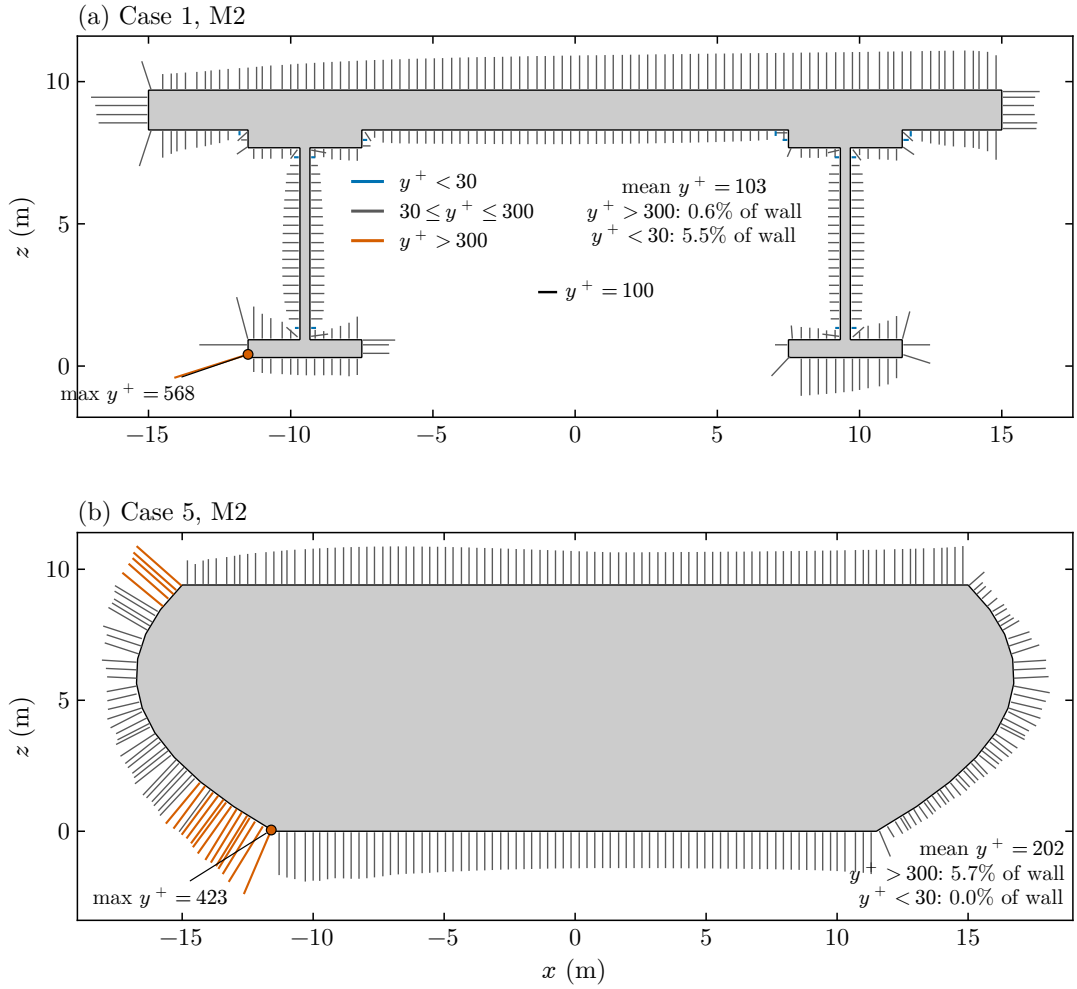


Fig. 17 Wall distance y^+ at the first cell centre for Case 1 (a) and Case 5 (b) on M2, at $t = 160$ s and a maximum Courant number of 2. Values are averaged in 0.3 m bins and drawn normal to the wall, with length proportional to y^+. Grey shows $30 \leq y^+ \leq 300$, blue $y^+ < 30$ and orange $y^+ > 300$. The dot shows the largest value on a single face. Wall-length fractions are listed in Table 16

Because the prism layers are the same on all three grids, the sensitivity to the wall treatment is tested separately by changing the first-layer thickness on Cases 1 and 5 to 5 mm and 20 mm instead of 8 mm. The nominal target means are about 50 and 200; the achieved means are 60 and 299 for Case 1 (103 on M2), and 115 and 573 for Case 5 (202 on M2). The eight-layer stack did not fit into the concave corners with a 20 mm first layer. We used four layers with an expansion ratio of 1.215 for this configuration. The total layer thickness is 0.110 m, approximately the same as on the baseline grids. This is a near-wall configuration test: the first-cell height, layer count and growth ratio change together. For Case 1, the 5 mm grid changes C_d by −0.02%, C_l by −0.17%, C_l' by +1.2% and St by

+0.2%. On the 20 mm grid, the changes are −0.32% in C_d, +0.64% in C_l, −1.2% in C_l' and 0.0% in St. Case 1 shows little sensitivity to these tested near-wall configurations. On Case 5, the faces with $y^+ > 300$ lie in attached, accelerating flow. Viscous drag accounts for 0.83% of the total drag on M2 and 0.85% at maximum Courant number 1 (Section 4.2). For Case 5, the 5 mm grid changes C_d by +1.7%, C_l' by −7.3% and St by −6.3%. The changes on the 20 mm grid are −1.3%, −5.9% and −0.4% for C_d, C_l' and St. The 20 mm run is averaged from 80 s because drag was still rising at 40 s. Its mean lift increases with the first-layer height, from 0.209 to 0.272 and 0.285 (−23% and +4.9%). The mean lift of Case 5 is particularly sensitive to grid resolution, time step and near-wall treatment (Sections 3.1.1 and 3.1.3). Because the drag of both sections changes by less than 2%, the 8 mm first layer is kept for all sections, with the y^+ values of Table 16.

G.5 Inflow, closure and far-field sensitivity details

G.5.1 Inflow turbulence, sustaining terms and Reynolds number

Cases 1 and 5 were repeated in three separate tests: an inflow turbulence intensity of 1.6% instead of 5%, no sustaining terms, and $U_\infty = 5$ m/s ($Re = 3.2 \times 10^6$). For Case 5, switching off the sustaining terms lowers C_l' by 18.8% and St by 6.5%, while C_d and C_l change by −1.6% and +2.5%. The run with an inflow intensity of 1.6% gives nearly the same coefficients as the run without the sustaining terms (within 0.6% in C_d, 1.5% in C_l', 0.1% in St and 4% in C_l). With the sustaining terms, the turbulence intensity remains at 5.0% one deck width upstream of the leading edge. Without them, it decays from the inlet to 2.7% at that location. Both the run with 1.6% inlet intensity and the run without sustaining terms expose the deck to less turbulence than the baseline. The two runs of Case 1 were still drifting at 160 s; they were extended to 320 s and averaged over 160–320 s. Their drag changes by only −0.2% (1.6% intensity) and −1.6% (no sustaining terms), but the shedding is much weaker: C_l' falls by 44% and 80%, St by 4.3% and 13.5% and C_l by 7% and 13%. The mean lift of the 1.6% run was still decreasing slowly at 320 s (block means from 1.308 to 1.280) and is taken as 1.29 ± 2%. The drag of both sections changed by no more than 1.6% in these tested intensity and sustaining-term configurations, while their shedding changed much more, particularly for Case 1. The comparisons of C_l' and St in Section 4 use the common inflow specified in Section 2.7. At $U_\infty = 5$ m/s (mean y^+ 41 instead of 202) C_d of Case 5 rises by 2.7%, and C_l, C_l' and St fall by 14.8%, 5.4% and 5.9%, while the coefficients of Case 1 change by less than 0.7% (mean y^+ 19).

G.5.2 Turbulence model and far-field condition

Cases 1 and 5 were repeated with the realizable k–ε model [54]. Other models in the k–ε family have been applied to rectangular sections [55]. With this model, vortex shedding in Case 5 almost disappears and C_l' falls from 0.357 to 0.002. Only a weak peak remains near $St \approx 0.23$. We do not use this peak as a reliable estimate of the shedding frequency. The recirculation length grows from 7.75 to 14.5 m. Its C_d, C_l and C_m change by −25%, +120% and −32% (both models over 40–80 s). For Case 1, C_d changes by only −1.9% (80–160 s), but the shedding again almost disappears ($C_l' = 0.008$), the recirculation length grows from 20.0 to 32.5 m, and the mean lift and moment fall by 38% and 36% (100–160 s). Both were still decreasing slowly, the lift by about 0.15% per 10 s, so their converged values may be about 1% lower. Both comparisons are at a maximum Courant number of 2. The order of the two sections in drag is the same with both models, and the drag reduction of Case 5 relative to Case 1 is 63% with the realizable k–ε model and 52% with SST. On both sections the realizable model gives a longer and almost steady wake. The mean lift, lift fluctuations and Strouhal number depend strongly on the turbulence closure. Section 4 compares all sections using the same SST configuration. We replace the slip top and bottom boundaries and the zero-gradient outlet with the `freestream` conditions used in the angle-of-attack series. At $\alpha = 0°$, the changes for Case 1 are +0.07% in C_d, +0.56% in C_l, −0.26% in C_l' and +0.06% in St. For Case 4, they are +0.16% in C_d, +0.36% in C_l, +0.62% in C_l' and +0.05% in St. For Case 5, they are +0.12% in C_d, −2.0% in C_l, +0.80% in C_l' and −0.01% in St. The angle-of-attack results in Section 4.5 use the $\alpha = 0°$ reference with the same boundary conditions.

The drag ordering of Cases 1 and 5 is unchanged in these tests. All sections use the baseline inflow, turbulence model and boundary conditions. Comparisons of C_l' and St are limited to runs with the same settings.

G.6 Benchmark geometry, settings and detailed comparisons

G.6.1 Suspension-span girder

The closed box girder (section H9.1 in Larsen [33]; $B = 31.0$ m, $D = 4.4$ m) is digitised from the dimensioned half-section and the main particulars given in that paper: bottom-plate half-width 9.5 m, top-deck crossfall 2.5%, nose tip 3.06 m above the bottom plate. Railings, crash barriers and guide vanes are not included in the model. Because the half-section sketch is not drawn exactly to scale, a variant with a bottom-plate half-width of 9.0 m,

as labelled in the sketch, is also computed at $\alpha = 0°$. The section is computed at $\alpha = -4°$, $0°$ and $+4°$ (positive nose up) with $U_\infty = 25$ m/s ($Re_D \approx 7.5 \times 10^6$), an inflow turbulence intensity of 5% and `freestream` far-field boundaries. The grid has 137 851 cells (about 141 cells per D and 992 per B on the surface), a maximum non-orthogonality of 64.8° and a maximum skewness of 0.98. To obtain this, the prism layers are not grown across edges sharper than 120° instead of 130° near the sharp nose. A control run on the 130° grid at $\alpha = 0°$ gives 3.6% lower C_d, 3.3% higher C_m and 4.5% lower C_l', while C_l and St differ by less than 1%. The computed C_d, C_l and C_m at 0° and the slopes $\mathrm{d}C_l/\mathrm{d}\alpha$ and $\mathrm{d}C_m/\mathrm{d}\alpha$ from the ±4° runs are compared in Table 4 and Fig. 18 with the 1:80 section-model and 1:300 taut-strip results of Larsen [33]. That paper does not state how the coefficients are normalised. For this comparison, we assume that C_d uses D, C_l uses B and C_m uses B^2. The computed coefficients are converted using these reference lengths. The experimental turbulence intensity is not stated. The simulations use a uniform mean inflow with 5% modelled turbulence. This difference limits the comparison. Compared with the 9.5 m section, the 9.0 m variant has 8.5% lower C_d and 29% lower C_l'. The differences in C_l, C_m and St are below 2%. The digitisation change has a much larger effect on drag and lift RMS than on the other quantities. The computed lift slope over ±4° is 4.51 per radian, 2–3% above the measured values. The moment slope is 1.45, exceeding the two measured estimates by 24% and 55%. The computed lift curve is nonlinear over this range. Its slope is 5.49 between −4° and 0° and 3.53 between 0° and +4°. The moment slope is nearly constant. The drag at 0° is less than half of the measured value, and the lift at 0° is 0.35 instead of nearly zero. The models were tested in turbulent flow. From the description in the paper, they appear to include the deck equipment that is not included here. These differences may contribute to the load discrepancies. Larsen does not state the angle range used to determine the measured slopes. Agreement in lift slope depends on the angle range used for comparison. The central lift-slope estimate agrees with the measurements, but the moment slope does not. This comparison does not validate the absolute loads. In the mean flow at 0° (Fig. 4(a)) the top and bottom faces stay attached, and reversed flow at the wall is found only behind the leeward lower inclined web.

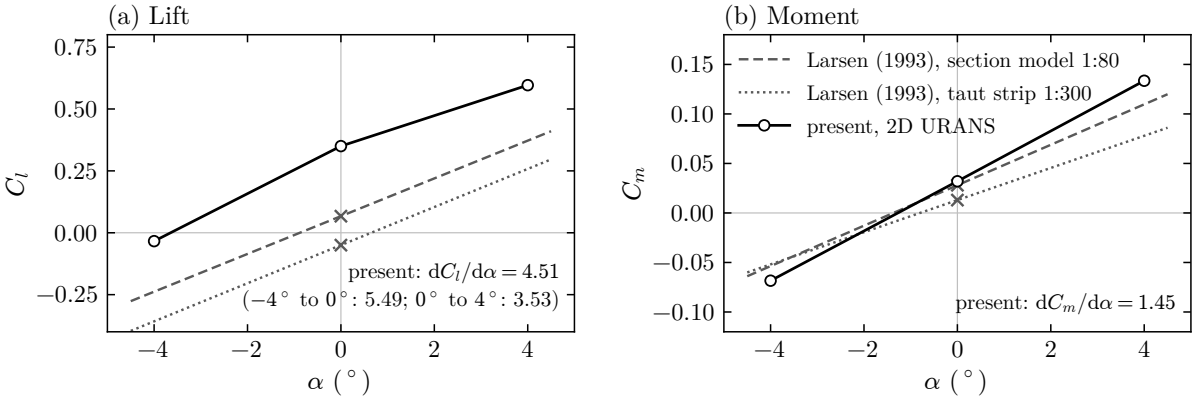


Fig. 18 Mean lift (a) and moment (b) of the Great Belt East Bridge suspension-span girder (GB-S) against angle of attack. Circles show the present computations: the −4° and 0° runs are averaged over 40–160 s, and the +4° run over 150–240 s. Dashed lines show the 1:80 section-model results, and dotted lines show the 1:300 taut-strip results of Larsen [33]. These lines are reconstructed from the reported values at 0°, shown by crosses, and the reported slopes; the source does not give the measured curves. The experimental normalisation is not stated. For this comparison, we assume that C_l uses B and C_m uses B^2. Slopes are per radian

G.6.2 Approach-span girder

The trapezoidal approach-span box ($B = 25.8$ m, $D = 7.0$ m) is digitised from the scale drawing of Schewe and Larsen [34] (uncertainty about ±0.1 m). Handrails and crash barriers are not included, as in the high-pressure wind-tunnel model. The wind screen, shown as optional in the drawing, is also not included. The section is computed at $\alpha = 0°$ and $Re_D = 1.0 \times 10^7$ with $U_\infty = 20.9$ m/s and `freestream` far-field boundaries. The inlet turbulence intensity is 0.3%, below the reported test-section limit of 0.4%. A separate sensitivity run uses 5%. The grid has 133 474 cells, a maximum non-orthogonality of 41.6° and a maximum skewness of 1.69. The 1:250 model tests had a blockage of about 4.7%. The Strouhal number, $St = fD/U_\infty$, rises from 0.18 below $Re_D = 8 \times 10^4$ to a plateau of 0.22 above 4×10^5. The drag coefficient C_d falls from a maximum of 0.68 to a plateau of 0.60 from $Re_D \approx 2 \times 10^6$. Its reference length is presumed to be D because the source does not state the normalisation. A prototype value of $St = 0.21$ was observed at $Re_D \approx 8.6 \times 10^6$ [34]. The highest test Reynolds number was 4×10^6, so the comparison at 10^7 assumes that the plateau continues, which the prototype value supports for St. The computed $C_d = 0.761$ and $St = 0.176$ do not reproduce the plateau: C_d exceeds even the low-Reynolds-number maximum, and St is close to the low-Reynolds-number value of 0.18. The computed wide wake resembles the

reported low-Reynolds-number flow more closely than the measured high-Reynolds-number flow. This similarity concerns the flow pattern and does not identify a transition state. The mean near-wall flow is consistent with that comparison (Fig. 4(b)). The flow stays attached on the windward web and separates at its corner with the bottom plate. It does not reattach on the bottom plate, where near-wall flow is reversed over 99.8% of the surface. On the leeward web, reattachment occurs only near the upper corner. This is the low-Reynolds-number pattern described by Schewe and Larsen [34], while at high Reynolds number they found the shear layer reattaching on the bottom plate, which narrows the wake. With wall functions (mean y^+ of 167 on the windward web and 174 on the bottom plate) the computation does not reproduce this reattachment; a possible reason is that the model underestimates the mixing in the separated shear layer. At an inflow intensity of 5%, C_d and St change by only −0.5% and −1.4% (to 0.757 and 0.174), and the bottom plate stays separated over its whole length, again with reversed near-wall flow over 99.8% of its surface. With wall functions on this grid, increasing the inflow intensity from 0.3% to 5% did not restore bottom-plate reattachment. A wall-resolved run, on a grid with a 0.03 mm first layer and prism layers on 91% of the wall, was started to test this further. In most time steps, the pressure equation did not reach its tolerance within the iteration limit. On 32 cores, the run advanced by only about 0.3 s of simulated time per hour. It was stopped at 2.2 s, before the averaging interval, and no result from this run is used. The deck sections show the same pattern: the long faces downstream of sharp corners on Cases 1 and 3 do not reattach, while on Case 5, with rounded fairings, the bottom plate reattaches at $x/B = 0.33$. If the model delays reattachment behind sharp corners at full-scale Reynolds number, as it appears to do on the approach span, it overestimates the drag of the bluff sections more than that of Case 5, and the drag reductions in Section 4 may be overstated. The size of this effect cannot be estimated from the present runs. The present tests do not separate the effects of wall treatment, dimensionality, turbulence closure and benchmark mismatch.

G.6.3 BARC rectangle

The rectangular cylinder with $B/D = 5$ and sharp corners [35] is modelled with $D = 4$ m and $B = 20$ m. To reach the benchmark Reynolds number, $Re_D = U_\infty D/\nu = 4 \times 10^4$, the kinematic viscosity is set to $\nu = 2.5 \times 10^{-3}$ m^2/s at $U_\infty = 25$ m/s. The 5:1 rectangle is sensitive to Reynolds number in this range [56]. On the BARC M2 mesh, the 8 mm first layer gives $y^+ \approx 1$–2. The calculation retains the wall-function boundary conditions for ν_t, k and ω. The inflow turbulence intensity is 0.3% (free-stream eddy-viscosity ratio $\nu_t/\nu \approx 13$) and the far-field boundaries are slip walls. The domain extends $47.5D$ upstream of the leading edge, $97.5D$ downstream of the trailing edge and about $50D$ above and below the section (blockage 1.0%). Following the benchmark, the force coefficients are based on D, and $St = fD/U_\infty$.

The mean drag, the Strouhal number, the lift RMS and the mean pressure on the side faces are compared with the wind-tunnel ranges and numerical statistics in the benchmark summary. The computed $C_d = 1.080$ and $St = 0.119$ lie within one standard deviation of the average of the numerical contributions (1.074 ± 0.129 and 0.109 ± 0.015). St is inside the wind-tunnel range of 0.105–0.132, and C_d is 3% above the upper end of the measured range of 0.94–1.05. The lift RMS, $C_l' = 0.780$, is also inside the numerical spread (0.65 ± 0.37); like the numerical average, it is well above the single wind-tunnel value of about 0.4, a discrepancy reported for the benchmark as a whole.

The computed side-face statistics are averaged over 40–160 s and combined between the upper and lower faces in bins of width $0.05D$. Comparison with the benchmark pressure distributions [35] focuses on profile shape, fluctuation levels and reattachment location. On the side faces the mean C_p, taken relative to the inlet pressure, stays near −0.87 up to $1.5D$ from the leading edge and then recovers to about −0.25 at the trailing edge, the plateau followed by recovery seen in the benchmark measurements. The mean reattachment distance is $4.40D$ from the leading edge, or $1.90D$ downstream of the section centre (Fig. 4(c)). The upper-face distance is $4.42D$, and the lower-face distance is $4.39D$. In this coordinate, the benchmark gives $2.25D \pm 0.45D$ for the numerical contributions and $1.875D$ for the one wind-tunnel measurement (both marked in Fig. 4(c)), so the present value lies within the numerical spread and close to the measurement. The root-mean-square pressure coefficient is about 0.06 near the leading edge, compared with the approximate upstream-side experimental level of 0.05 reported in the benchmark discussion. It falls to a minimum of 0.010 about $2D$ from the leading edge, as in the RANS contributions, and peaks at 0.188 at 3.7–3.8D, just upstream of reattachment, where the measured fluctuations also peak.

Appendix H Engineering tests and additional diagnostics

The mean flow around the factorial and variant sections is shown in Figs. 10 and 19 and discussed in Section 5.1.

H.1 Detailed single-feature and sequential comparisons

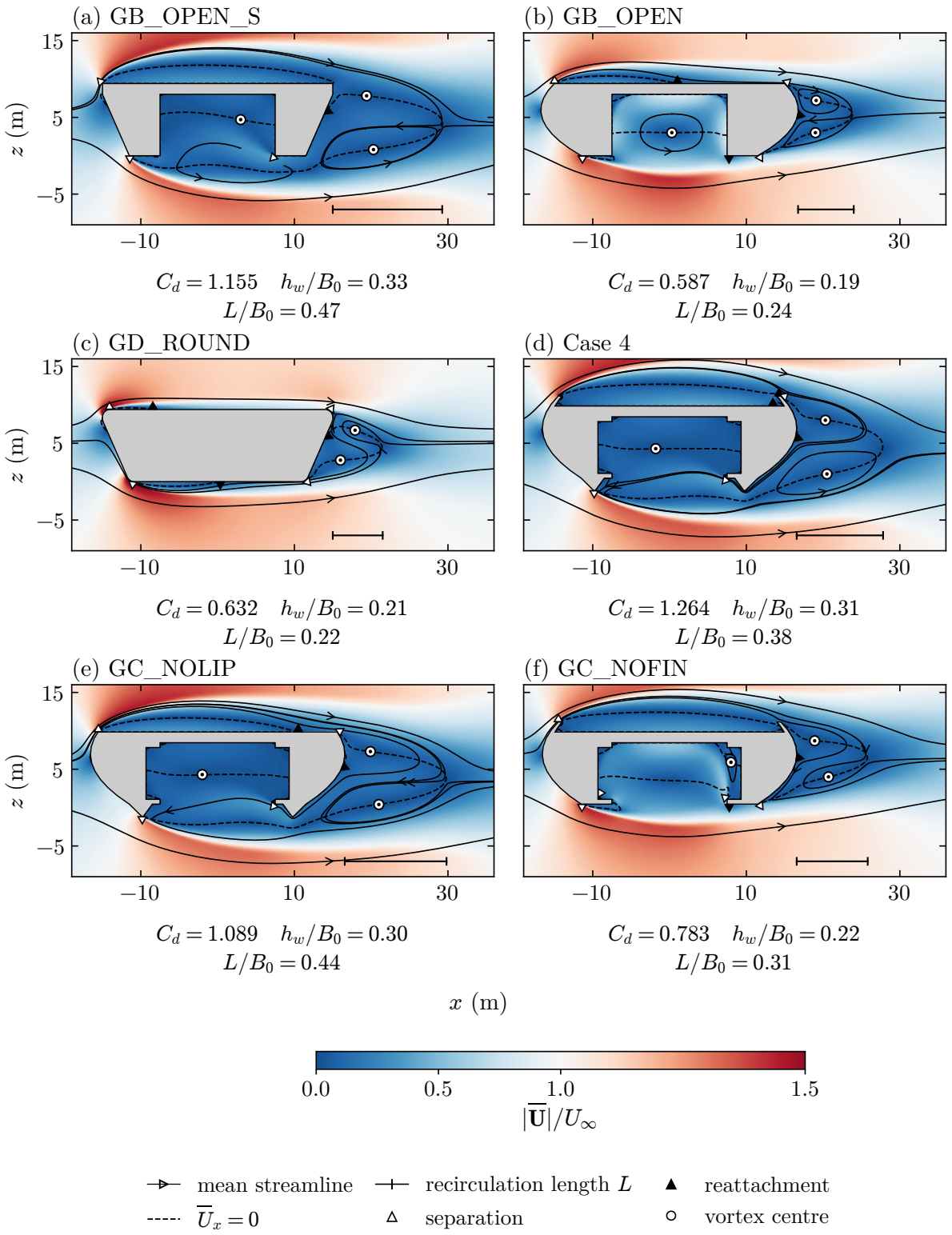


Fig. 19 Mean flow around the open-cavity, rounded-corner and Case 4 variant sections. Scale, symbols and quantities follow Fig. 10. All runs use M2 and a maximum Courant number of 1. The averaging window is 40–120 s, except for GC_NOLIP, which uses 60–120 s. Case 4 is shown over 40–120 s. Its matched force statistics over 60–120 s for the GC_NOLIP comparison are listed separately in Table 7

The sequence Case 1 → Case 2 → Case 3 → GA_LE → Case 5 adds girder encasement, cavity closure, a curved leading edge and a curved trailing edge in turn. The C_d values are 1.284 for Case 1, 1.267 for Case 2, 1.248 for

Case 3, 1.189 for GA_LE and 0.590 for Case 5. Relative to the Case 1 drag, the four steps give changes of −1.3%, −1.5%, −4.6% and −46.7% in that order. Cases 1 and 2 use a maximum Courant number of 2, with averaging windows of 40–160 s for Case 1 and 100–250 s for Case 2. The other sections use the settings in Table 8. With the uncertainties of the two ends combined as independent, only the last step is resolved. Almost the whole reduction occurs in the step that completes streamlining. Set A shows that this large step includes the interaction between the two edges and cannot be assigned to the trailing-edge main effect alone. If the trailing edge were curved first, curving the leading edge last would give the large change of −0.590. The viscous part of the drag changes only in the step to GA_LE (+0.009).

Rounding the convex corners of Case 3 with a radius of 1 m (GD_ROUND) lowers C_d from 1.248 to 0.632, which is approximately 94% of the reduction obtained with the curved fairings of Case 5. Its drag is 7% above that of Case 5: 0.632 ± 0.023 compared with 0.590 ± 0.013. Its mean lift changes sign to −0.26, compared with +0.53 for Case 3 and +0.33 for Case 5. Its Strouhal number is 0.238, the highest of all sections at $\alpha = 0°$. On the rounded corners y^+ exceeds 300 on 4.3% of the wall area, up to 485, with the near-wall treatment discussed for Case 5 (Section 5.3).

Removing the deflector lips (GC_NOLIP) or the bottom fins (GC_NOFIN) of Case 4 shows that the two parts act differently on the mean loads (both compared with Case 4 at a maximum Courant number of 1 over the same window). Without the fins, drag falls by 38%, from 1.264 to 0.783 ± 0.028, with $E = -0.481 \pm 0.053$. This drag is 39% below that of Case 1. The mean lift falls from 1.39 to 0.15, and the mean moment falls from 0.72 to −0.02, both approaching zero. The fins add 1.6 m, or 13%, to the projected height. The 38% drag change is the response of the complete section, including changes in the pressure field; it is not a direct force per unit area on the removed fins. Without the lips, which rise 1.3 m above the deck, the drag falls by 14% ($E = -0.175 \pm 0.060$) and the moment rises from 0.73 to 1.30 ($E = +0.571 \pm 0.022$), while the change of the mean lift (−0.14) is not resolved. Neither part accounts for the rise in C_l' from Case 1 to Case 4: removing the lips lowers C_l' from 0.578 to 0.374 and removing the fins from 0.579 to 0.466, but neither change is resolved, even with the formal order of the scheme in the grid uncertainty ($U = 0.32$ and 0.35), and the Strouhal number changes by less than its uncertainty in both cases. As in the factorial sets, the changes of C_d are pressure changes; the viscous drag of the three sections is below 0.001 in magnitude.

H.2 Incidence response and flow fields

Fig. 20 shows the mean loads and the lift RMS of Cases 1, 4 and 5 between $\alpha = -10°$ and +10°, and the finite-interval lift and moment secants are reported below. The comparison uses the $\alpha = 0°$ runs with `freestream` far-field boundaries (Section 3.1.5). Cases 1 and 4 were computed with a maximum Courant number of 2, Case 5 with a maximum Courant number of 1. The 0° run of Case 5, started from a uniform field, agrees with the run of Table 5 to within 0.2% in C_d and 1.9% in C_l. The time-step sensitivity of Case 5 varies with the angle: between Courant numbers of 2 and 1 its drag changes by −12% at −10°, −5% at 0° and +0.2% at +10° when both members use the accepted window of Fig. 20. For Cases 1 and 4 the mean coefficients change by less than 0.5% between these Courant numbers at 0° (Section 3.1.3), but this was not checked at incidence.

For the mean-load check, we apply the relative grid allowance at zero angle of attack to the value at each angle. Case 1 uses its own relative allowance. Case 4 uses the larger allowance from Cases 1 and 3, and Case 5 uses its own. Cases 1 and 4 also transfer their relative time-step contributions at zero angle of attack. For Case 5, the adopted $U_{\Delta t}$ is the larger of that transferred contribution and the absolute change between its existing maximum-Co 2 and maximum-Co 1 runs at the same angle and over the same accepted window. Combining this with U_{GCI}, U_s and U_w gives the screening allowance U_α in Table 17. Using only the transferred time-step term would give $U_\alpha(C_d) = 0.027$ at −10°, versus 0.169 when the observed angle-matched change is included. The corresponding moment allowance rises from 0.039 to 0.224. At 0°, this rule gives $U_\alpha(C_d) = 0.033$. There is no maximum-Co 0.5 run in this `freestream` series. The time-step contribution is the change of 0.030 between maximum Courant numbers 2 and 1 over 60–120 s, used here as a conservative screening value. In the slip-boundary series of Section 3.1.3, C_d changes by a similar 4.95% between these Courant numbers; the smaller allowance of Case 5 in Table 5 (±0.013) comes from the finer pair of that series, maximum Courant numbers of 1 and 0.5 over 40–160 s. The two allowances refer to different boundary conditions, time-step pairs and windows. The larger allowances include the observed time-step sensitivity. They do not establish time-step convergence in the angle-of-attack runs. No measured error bound is available for transferring the spatial allowance or for the untested time-step sensitivity of Cases 1 and 4 away from zero angle of attack. The lift-RMS curves describe the computed values only. Block scatter alone does not provide a complete numerical allowance for them.

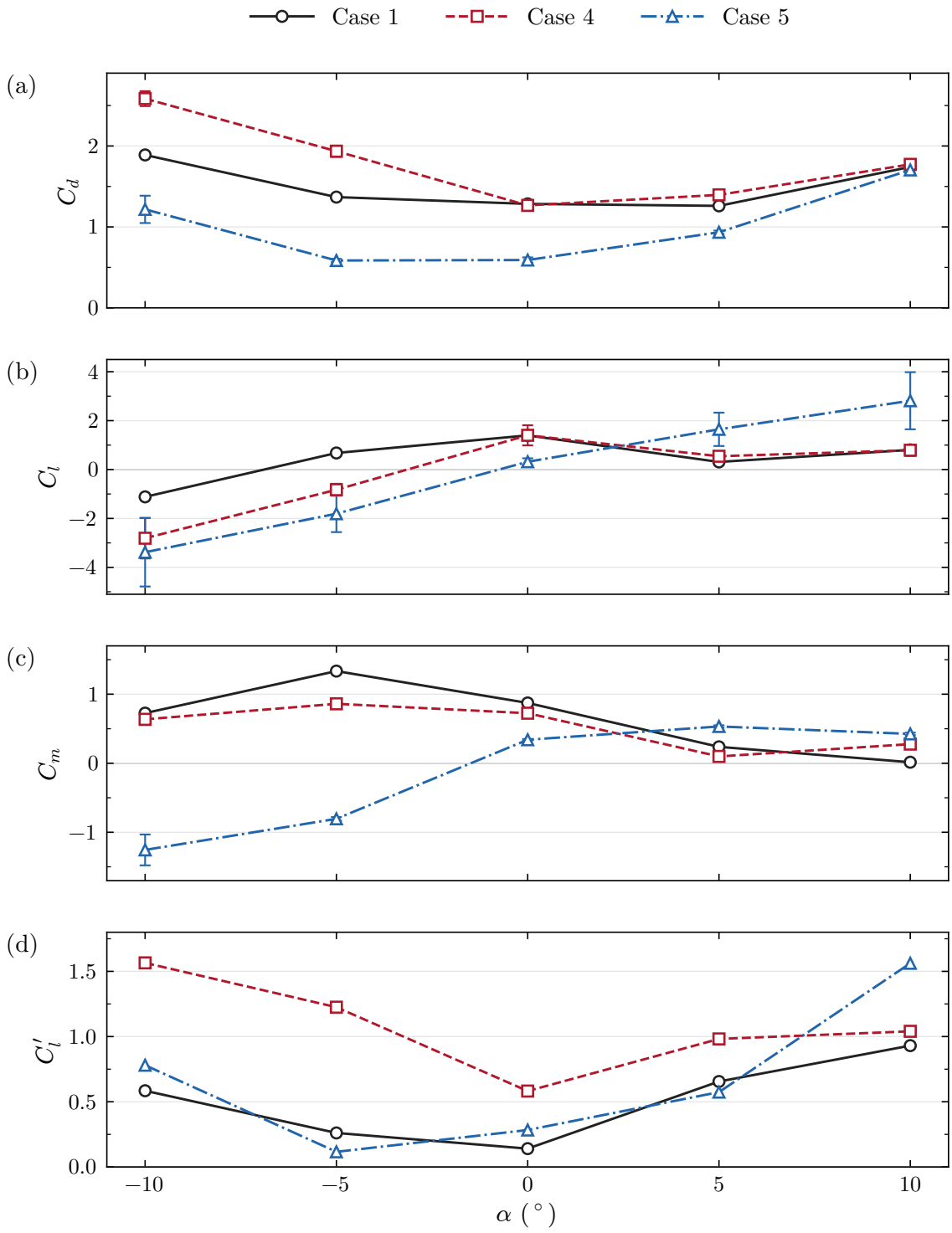


Fig. 20 Mean drag (a), lift (b) and moment (c) coefficients and lift RMS (d) for Cases 1, 4 and 5 at different angles of attack. Positive angles are nose up, and all runs use `freestream` outer boundaries. Cases 1 and 4 use a maximum Courant number of 2 and a 40–160 s window, except for Case 1 at +5° (from 60 s) and Case 4 at −10° (160–320 s). Case 5 uses a maximum Courant number of 1 and a 40–120 s window, with the 0° window starting at 60 s. Bars in (a–c) give the adopted screening allowances $\pm U_\alpha$ for all three sections. Table 17 lists the Case 5 values. These allowances are not confidence intervals or model-error bounds. Panel (d) describes the computed lift RMS; no complete RMS budget is available. Symbols show the computed angles, and straight segments are visual guides

Table 17 Mean-load screening for Case 5 at different angles of attack. Values use the maximum-Co 1 runs and the windows in Fig. 20. Parentheses give U_α, which combines transferred spatial sensitivity, the larger of the transferred and angle-matched time-step contributions, block scatter and the window-end term. These are numerical sensitivity allowances, not confidence intervals or model-error bounds

α (°)	C_d (U_α)	C_l (U_α)	C_m (U_α)
−10	1.217 (0.169)	−3.381 (1.402)	−1.255 (0.224)
−5	0.585 (0.020)	−1.807 (0.753)	−0.805 (0.025)
0	0.591 (0.033)	0.319 (0.142)	0.340 (0.011)
5	0.934 (0.021)	1.645 (0.682)	0.533 (0.017)
10	1.704 (0.038)	2.814 (1.168)	0.425 (0.018)

Full streamlining gives a lower drag point estimate at each sampled angle, but the difference is not resolved at +10° and its size depends strongly on incidence (Fig. 20(a)). Relative to Case 1, the drag of Case 5 is lower by 54% at 0°, 57% at −5°, 36% at −10° and 26% at +5°. At +10° the three sections have almost the same drag (C_d = 1.70–1.77), and Case 5 differs from Case 1 by less than its own screening allowance (C_d = 1.704, U_α = 0.038, against 1.741). The drag of Case 5 is lowest between −5° and 0° and rises steeply on the nose-up side. The deflectors of Case 4, which leave the drag unchanged at 0°, raise it above that of Case 1 at every other angle: by 37% and 41% at −10° and −5°, 11% at +5° and 2% at +10°. The last percentage is a point-estimate difference, not a separately resolved effect.

The lift curves of the two bluff sections have their maximum near 0° (Fig. 20(b)). Between 0° and +5°, the mean lift falls from 1.40 to 0.31 in Case 1 and to 0.54 in Case 4. For both sections, the lift secant is positive between −5° and 0° and negative between 0° and +5° (Table 18). Between +5° and +10°, lift rises again, reaching 0.80 in Case 1 and 0.79 in Case 4. Over 0° to +5° the finite-interval indicator $H_{\text{sec}} = \Delta C_l/\Delta\alpha + C_d(0°)$ is negative (−11.1 and −8.5, with $\Delta\alpha$ in radians); over ±5° it is −0.8 for Case 1 and +9.1 for Case 4. The 5° spacing does not resolve a local Den Hartog criterion. These static-load secants do not establish galloping susceptibility or onset. The lift of Case 5 rises monotonically over the whole range, with a slope of 19.8 per radian over ±5° with the common depth-based force normalisation. Its H_{sec} is positive for the three listed intervals (20.4 over ±5°). The moment slope changes sign with streamlining (Fig. 20(c)). For Cases 1 and 4, it is negative on both sides of 0°; the secants over ±5° are −6.3 per radian for Case 1 and −4.4 for Case 4. The moment change opposes a nose-up rotation. For Case 5, the secant over ±5° is +7.7, and the computed moment about the specified reference point increases up to +5°. A static moment secant about this reference point does not determine aeroelastic stability.

Table 18 Finite-interval lift and moment secants from Fig. 20, with angle increments in radians, and the static-load indicator $H_{\text{sec}} = \Delta C_l/\Delta\alpha + C_d(0°)$. The ±5° and ±10° rows span the corresponding negative and positive endpoints. Coefficients use D as defined in Eq. (9). The entries are point estimates of secants, not local derivatives with established uncertainty. They do not determine a local stability criterion

Quantity	**Interval**	Case 1	Case 4	Case 5
$\Delta C_l/\Delta\alpha$	−5° to 0°	8.2	25.5	24.4
	0° to +5°	−12.4	−9.8	15.2
	±5°	−2.1	7.8	19.8
	±10°	5.5	10.3	17.7
$\Delta C_m/\Delta\alpha$	−5° to 0°	−5.3	−1.6	13.1
	0° to +5°	−7.3	−7.2	2.2
	±5°	−6.3	−4.4	7.7
	±10°	−2.0	−1.0	4.8
H_{sec}	−5° to 0°	9.5	26.8	24.9
	0° to +5°	−11.1	−8.5	15.8
	±5°	−0.8	9.1	20.4

The lift RMS of Cases 1 and 4 is smallest at 0° and grows on both sides (Fig. 20(d)). On Case 5, C_l' falls from 0.28 at 0° to 0.12 at −5° but rises to 0.78 at −10° and 1.56 at +10°, which exceeds the values of Cases 1 (0.93) and 4 (1.04) at that angle. Its Strouhal number falls from 0.214 at 0° to 0.138 at +10°. Case 4 has the largest fluctuations on the nose-down side (1.23 at −5° and 1.57 at −10°), where its wake at −10° changed state during the run (Section 2.9) and sheds at St = 0.062, less than half the value at 0°. In Case 5, the wall area with $y^+ > 300$ reaches 15% at +10°, compared with 5.7% at 0°. The near-wall limitation discussed in Section 5.3 is more relevant at non-zero angles of attack.

The mean flow fields at −10°, 0° and +10° (Fig. 21; near-wall reversal judged as in Section 5.1, $\xi = (x - x_{\text{LE},i})/B_0$) are consistent with the reduced streamlining advantage on the nose-up side. At 0°, the near-wall

flow on the top face of Case 5 is reversed up to $\xi = 0.62$, where it reattaches. At +10°, reversal covers the entire top face and no reattachment occurs. The wake reversed-flow height increases from 6.4 to 10.3 m. At this angle, Case 5 has top-face separation like the sharp-edged sections. At −10° the separation moves to the bottom face, which is reversed from $\xi = 0.19$ to 0.94 without reattaching, while the top face is reversed only up to $\xi = 0.17$. The top faces of Cases 1 and 4 are fully separated at 0° but reattach at both −10° and +10°. In Case 1, reattachment occurs at $\xi = 0.30$ at −10° and $\xi = 0.93$ at +10°. In Case 4, the locations are $\xi = 0.58$ at −10° and $\xi = 0.87$ at +10°. The wake is nevertheless taller than at 0°: 13.1–14.8 m compared with 11.9 m in Case 1, and 13.1–13.8 m compared with 9.2 m in Case 4. On all three sections the reversed-flow region of the wake is taller at ±10° than at 0°, in line with the higher drag.

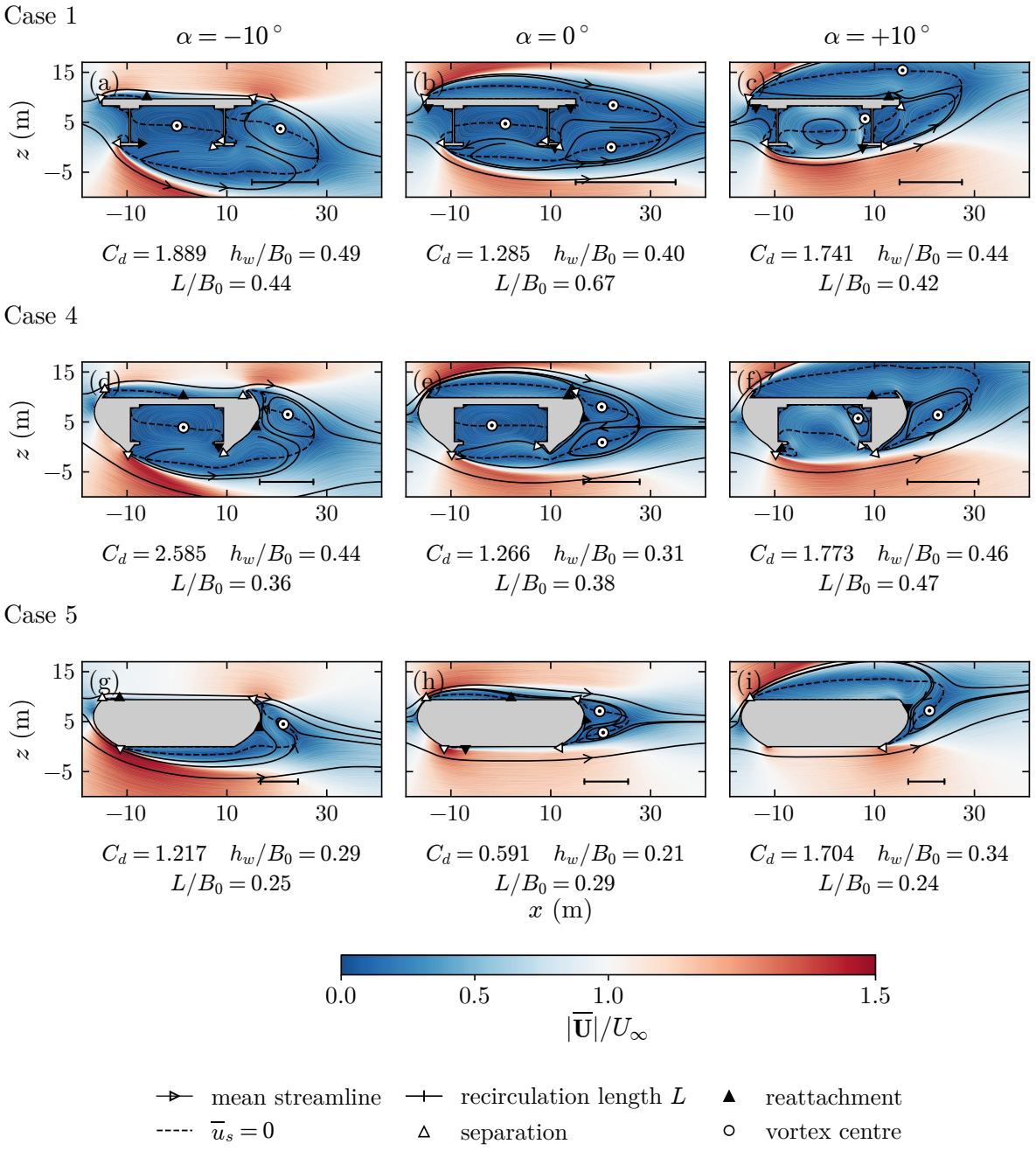


Fig. 21 Mean flow around Cases 1, 4 and 5 at $\alpha = -10°$, 0° and +10°. The sections are fixed, and the inflow direction is rotated. Averaging windows are those in Fig. 20. Colours, texture, arrows, triangles and circles follow Fig. 5. Dashed lines show where the velocity component in the inflow direction is zero. Brackets give the streamwise recirculation length L of the region where this component is negative. Rows show the sections, and columns show the angles. Values below the panels are C_d from Fig. 20, the normalised reversed-flow height h_w/B_0 and L/B_0, with B_0 = 30 m

H.3 Barrier loads and flow fields

Table 19 gives the loads of Cases 1, 4 and 5 with solid and porous barriers (Section 2.3). All six runs have force statistics over 40–160 s, containing between 38 and 59 shedding cycles. Field-averaging windows are identified separately in Fig. 22. For all six cases, the separately recorded mean drag and lift of the deck and barrier sum to the total within 1.1×10^{-11} in coefficient units. This checks the force accounting, not convergence.

Table 19 Loads with traffic barriers over 40–160 s. The row below each barrier gives the local sensitivity allowance U_{loc} for the difference between runs with and without barriers (Section 2.3). It is a non-negative allowance for that difference, not an error bar on the total load above it. An asterisk indicates a change smaller than U_{loc}. A change without an asterisk is not necessarily resolved against global-grid or model error. The moment coefficient C_m uses the reference point in Section 2.5. Share is the barrier drag as a percentage of total drag

Section	Barrier	C_d	C_l	C_m	C_l'	St	Share (%)
Case 1	none	1.284	1.388	0.869	0.141	0.138	–
	solid	1.511	1.175	0.567	0.112	0.121	7.4
	U_{loc}	0.003	0.015	0.011	0.003	<0.001	
	porous	1.423	1.015	0.901*	0.084	0.121	7.1
	U_{loc}	0.033	0.019	0.216	0.044	0.006	
Case 4	none	1.264	1.395	0.721	0.579	0.147	–
	solid	1.258	1.461	0.718*	0.556	0.147*	−0.7
	U_{loc}	0.001	0.005	0.004	0.003	<0.001	
	porous	1.244	1.535	0.734	0.539	0.148	−0.1
	U_{loc}	0.009	0.065	0.005	0.020	<0.001	
Case 5	none[a]	0.590	0.325	0.340	0.279	0.214	–
	solid	0.901	1.008	−0.458	0.649	0.170	16.0
	U_{loc}	0.012	0.143	0.009	0.029	0.002	
	none[b]	0.593	0.307	0.336	0.279	0.213	–
	porous	0.763	−0.220	0.051	0.229*	0.186	17.4
	U_{loc}	0.029	0.024	0.039	0.088	0.003	

[a] Maximum Courant number 1, as in Table 5; reference for the solid barrier. [b] Maximum Courant number 0.5 (Section 3.1.3); reference for the porous barrier.

The barriers raise the drag of the bare section by 18% (solid) and 11% (porous) and that of the streamlined section by 53% and 29%, but leave the drag of Case 4 almost unchanged (−0.5% and −1.6%). The increase on Case 5 with solid barriers lies within the 50–66% reported for decks with barriers by Scotta et al. [10] and Kusano et al. [11]; the bare section, whose drag is more than twice as large, rises much less. On Cases 1 and 5 the barrier itself carries 7% and 16–17% of the total drag. With the solid barrier it accounts for about half of the increase, and the other half arises on the deck (+0.116 in C_d on Case 1 and +0.167 on Case 5); with the porous barrier it accounts for 72% and 78% of the increase. On Case 4 the barrier stands in the lee of the deflector lip, which rises 0.3 m above it, and carries a small negative drag; the total drag of this section changes by less than 2%.

The order of the three sections in drag is the same with both barriers. With the same barrier on Cases 1 and 5, the drag reduction of Case 5 falls from 54.1% without barriers to 40.4% with solid barriers and 46.4% with porous barriers. Case 5 still gives the largest reduction by a wide margin. That of Case 4 rises from 1.5% to 16.7% and 12.6%, because the barriers add drag to Case 1 but not to Case 4. These are point-estimate ratios. The local allowances apply to differences between runs with and without barriers. They do not describe the errors in the total loads used to calculate these ratios, so propagating them as absolute-load errors would not give a supported uncertainty interval. Global-grid error in the ratios remains unquantified. The calculated advantage of Case 4 with barriers comes from the shelter of the barrier by the deflector lip and holds for this arrangement only (Section 2.3).

On Case 5 the barriers change the mean lift and moment far more than the drag, and the two barriers act in opposite directions. The solid barrier triples the lift of Case 5, from 0.325 to 1.008, and reverses the sign of its moment. The porous barrier makes the lift negative, at −0.220, and reduces the moment to 0.051. In Case 1, lift falls by 15% with the solid barrier and 27% with the porous barrier. The solid barrier lowers the moment by 35%. The porous-barrier moment change does not exceed the local allowance: its moment changes by 32% between the two barrier-grid levels. On Case 4 the lift rises by 5% and 10% and the moment changes by less than 2%. With barriers, Case 4 has the largest mean lift of the three sections. Without barriers, its lift difference from Case 1 is unresolved.

Fig. 22 shows the mean flow around Cases 1 and 5 with and without barriers. With solid barriers, a thick recirculation region covers the entire upper surface of Case 5 between the barriers. The bare section has only a thin separation bubble behind the windward edge. This flow change is consistent with the threefold mean lift. Behind Case 1 the barriers lengthen the recirculation region from $L/B_0 = 0.67$ to 0.83 (solid) and 0.92 (porous); behind Case 5 its length hardly changes with the solid barrier (0.28 against 0.29) and grows to 0.40 with the porous one.

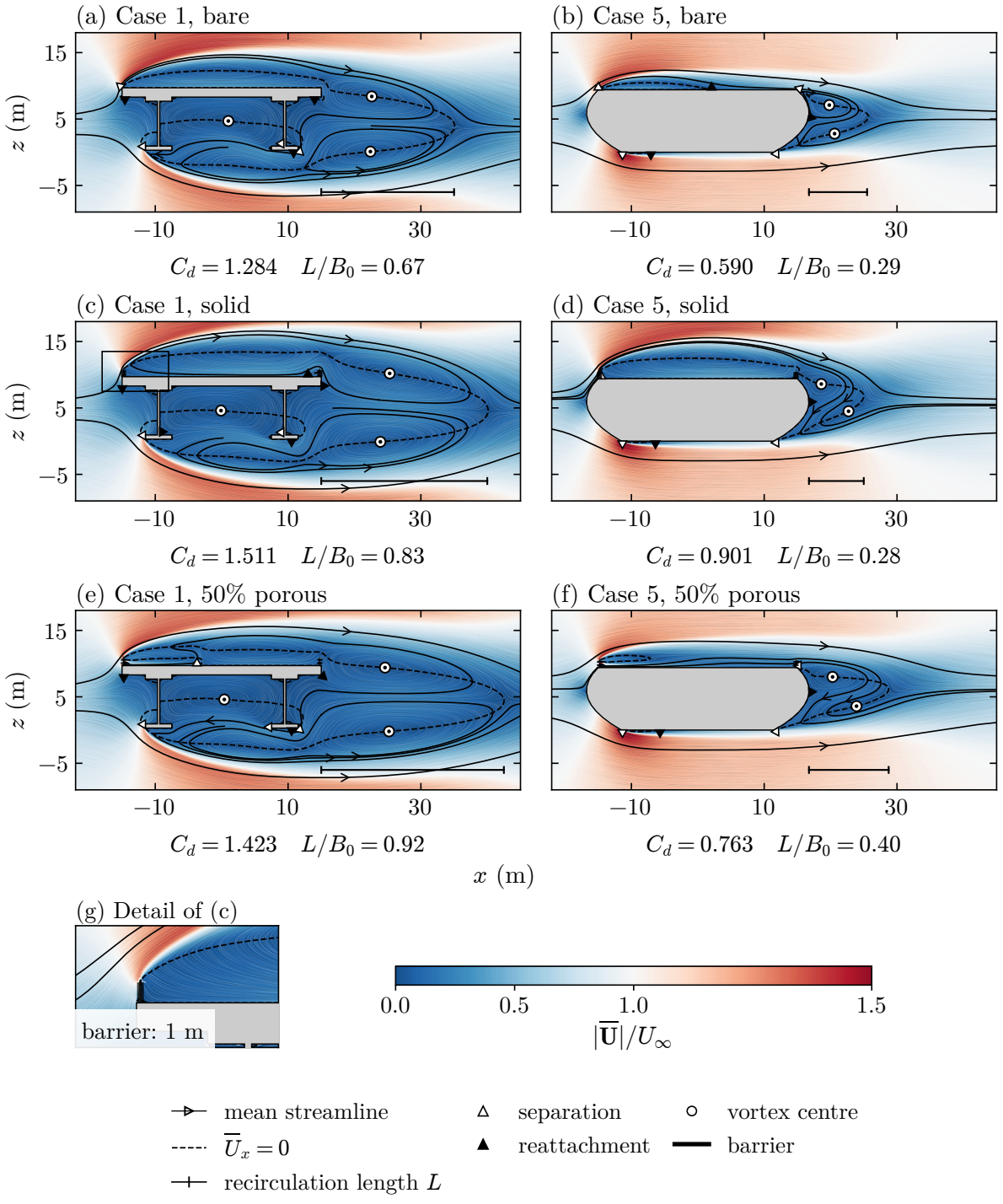


Fig. 22 Mean flow around Cases 1 and 5 without barriers and with solid or 50%-porous barriers, shown by thick lines. The averaging window is 40–160 s, except for Case 1 with the porous barrier, which uses 40–150 s. Bare sections use M2; Case 5 has a maximum Courant number of 1. Barrier runs use the finer barrier grid. The bare panels reuse the baseline fields from Fig. 5 for comparison. Colours, texture, arrows and symbols follow that figure. Brackets show the recirculation length L. Panel (g) enlarges the boxed region in (c) and shows the 1 m windward solid barrier. Values below the panels are C_d from Table 19 and L/B_0, with B_0 = 30 m. Panel (b) shows the bare field at maximum-Co 1. The maximum-Co 0.5 bare reference used for the porous-barrier force comparison is not shown

The barriers lower the Strouhal number of Case 1 by 12% with either porosity. For Case 5, the reduction is 21% with the solid barrier and 13% with the porous barrier. Case 4 changes very little, so the ordering of the sections in St is unchanged. The lift RMS of Case 1 falls by 21% and 41% and that of Case 4 by 4% and 7%. In Case 5, the solid barrier raises lift RMS by 133%, to above the value for Case 4. The change with the porous barrier does not

exceed the local allowance. The apparent reductions in lift RMS on Cases 1 and 4 cannot be claimed as resolved against global-grid error: the bare-section allowances are already much larger than these changes. For example, the Case 1 solid barrier changes C_l' by −0.029, compared with $U_{\mathrm{loc}} = 0.003$ but a bare-section global allowance of 0.360. Likewise, the Case 4 solid-barrier drag change is −0.006, compared with $U_{\mathrm{loc}} = 0.001$ and a bare-section allowance near 0.045. These changes are compared with the bare-section allowances only to show their relative size. The comparison does not estimate the error in the paired difference or assume independent errors. Resolving these small effects against global-grid error would require error cancellation that has not been demonstrated. In these computations, barriers leave the section ordering in drag and Strouhal number unchanged. Full streamlining retains its drag advantage, but the advantage falls by 8 to 14 percentage points. The mean lift and moment of the streamlined section can also change sign. The lift and moment of the bare sections do not apply unchanged after barriers are added. The changes depend on barrier porosity and deck shape, as discussed in the Introduction.

H.4 Additional flow interpretation

The factorial mechanisms are discussed in Sections 4.3.1 and 5.1. The observations below concern the baseline contrast, the deflectors and the single rounded-corner variant.

Closing the cavity from Case 1 to Case 3 lowers mean lift from 1.39 to 0.52. In the baseline pressure partition, replacing the cavity and bottom flanges with the bottom plate accounts for 0.49 of this decrease. Weaker top-face suction accounts for 0.24, and the webs and cantilevers account for 0.14. The bottom-plate mean pressure coefficient is −0.94 (−1.09 on its windward half), compared with −0.76 on the Case 1 cavity faces and −0.71 on its bottom flanges. This is the baseline partition of Section 4.2, distinct from the matched six-section partition in Appendix C. The mean field places the lower shear layer 2–3 m below the leeward bottom flange of Cases 1 and 2. It does not show persistent impingement on the cavity's downstream edge, but cannot exclude intermittent or three-dimensional cavity interactions [57].

For Case 4, the lower shear layer leaves the windward fin tip and passes about 1 m below the leeward tip. The shorter recirculation region and possible shear-layer/edge interaction may contribute to the larger lift fluctuation, but their contributions are not separated. Removing the fins lets the shear layer enter the cavity, lowers the wake height from 9.2 to 6.7 m and reduces drag by 38% (Fig. 19). The 20% decrease in lift RMS is unresolved under the adopted allowance. It cannot confirm or rule out the proposed fin-tip mechanism. Removing the lips instead allows top-face reattachment near $\xi = 0.90$ and leaves the wake height almost unchanged (9.1 m).

The reversed-flow height is 7.9 m for Case 3 and 6.3–6.5 m for GA_LE, GA_TE and Case 5. These heights alone do not explain the different drag reductions or the edge interaction. The pressure budget explains why these sections have different drag reductions (Section 4.3.1). For GD_ROUND, rounding the convex corners of Case 3 with $r = 1$ m shortens top-face reversal to $\xi = 0.04$–0.21 but extends the bottom bubble to $\xi = 0.50$. Its computed drag reduction relative to Case 3 is approximately 94% of the Case 3-to-Case 5 reduction. This comparison concerns the single tested radius and its accompanying deck-edge modification.

H.5 Exterior-skin screening calculation

We use the new exterior-skin length S_i to measure the added skin. It is the part of the outer contour of section i that does not coincide with the Case 1 contour. With a common plate thickness t and steel density $\rho_s = 8000$ kg/m^3, the added mass per metre span is $\rho_s t S_i$ in kg/m when t and S_i are in metres. Converting this quantity to t/m gives $\Delta m_i = 10^{-3}\rho_s t S_i$ for the efficiency index

$$\eta_{m,i} = \frac{R_{D,i}}{\Delta m_i}, \qquad R_{D,i} = 100\,\frac{\bar{F}_{D,1} - \bar{F}_{D,i}}{\bar{F}_{D,1}}, \tag{H2}$$

which gives the drag reduction in percentage points per tonne of steel per metre. This quantity counts new exterior contour and does not subtract parent material removed by a geometric change. For GD_ROUND, this is a measure of new skin, not the net material needed to retrofit the original deck. The index is evaluated with $t = 10$ mm; a common t scales all masses equally and does not change the ranking. The calculation does not include stiffeners, diaphragms, connections or fabrication cost. The index η_m compares drag reduction with added skin mass; it does not estimate cost. For the factorial sets the same skin lengths give the material change that corresponds to each main effect.

Table 20 compares computed drag reduction per tonne of added exterior skin per metre of span. Full streamlining gives 17.1 percentage points per t/m, with an adopted numerical allowance of ±0.34 from R_D. For Cases 2–4, none of the values is resolved from zero under the same numerical budget. The rounded variant GD_ROUND gives a point estimate of 17.2 and uses 7% less skin than Case 5. The open-bottom variant GB_OPEN gives a similar point estimate of 17.9 and uses 4% less skin than Case 5. For GD_ROUND, varying the contour-matching

tolerance from 0.01 to 5 mm changes the estimated skin length by 2.3%, versus at most 0.18% for the other sections. Structural demand and maintenance costs are outside this exterior-skin calculation.

Table 20 New exterior-skin length S_i per cross-section, added steel mass Δm_i per metre span at t = 10 mm, drag reduction R_D and efficiency index η_m in percentage points per t/m. For the variants, R_D is relative to Case 1 in Table 5. Their C_d values use a maximum Courant number of 1 and the windows in Section 2.9. The uncertainty in their R_D is 1.7–3.4 percentage points

Section	S_i (m)	Δm_i (t/m)	R_D (%)	η_m
Case 2 (Encase)	32.645	2.612	1.3	0.50
Case 3 (Enclose)	32.455	2.596	3.1	1.20
Case 4 (Deflect)	39.818	3.185	1.5	0.48
Case 5 (Streamline)	39.489	3.159	54.1	17.11
GA_LE	35.972	2.878	7.4	2.57
GA_TE	35.972	2.878	8.1	2.81
GB_OPEN_S	30.953	2.476	10.1	4.07
GB_OPEN	37.987	3.039	54.3	17.87
GC_NOLIP	33.401	2.672	15.1	5.67
GC_NOFIN	30.892	2.471	39.0	15.77
GD_ROUND	36.845	2.948	50.8	17.22

H.6 Baseline spectra and surface pressures

Fig. 23 gives the baseline lift spectra, and Fig. 24 gives the surface-pressure distributions. These data accompany the baseline comparisons in Sections 4.1 and 4.2. For the Welch spectra, each force record is linearly resampled at its median original time interval (approximately 1.040, 1.120, 1.030, 0.908 and 0.427 ms for Cases 1–5). Five Hann-windowed segments overlap by 50%; the FFT length equals the segment length, with no zero padding. The segment durations give frequency-bin spacings of about 0.025 Hz (0.020 Hz for Case 2). We refine the peak location by three-point interpolation of the logarithmic spectrum. Neither the interpolated peak location nor the bin spacing provides an independent estimate of frequency uncertainty.

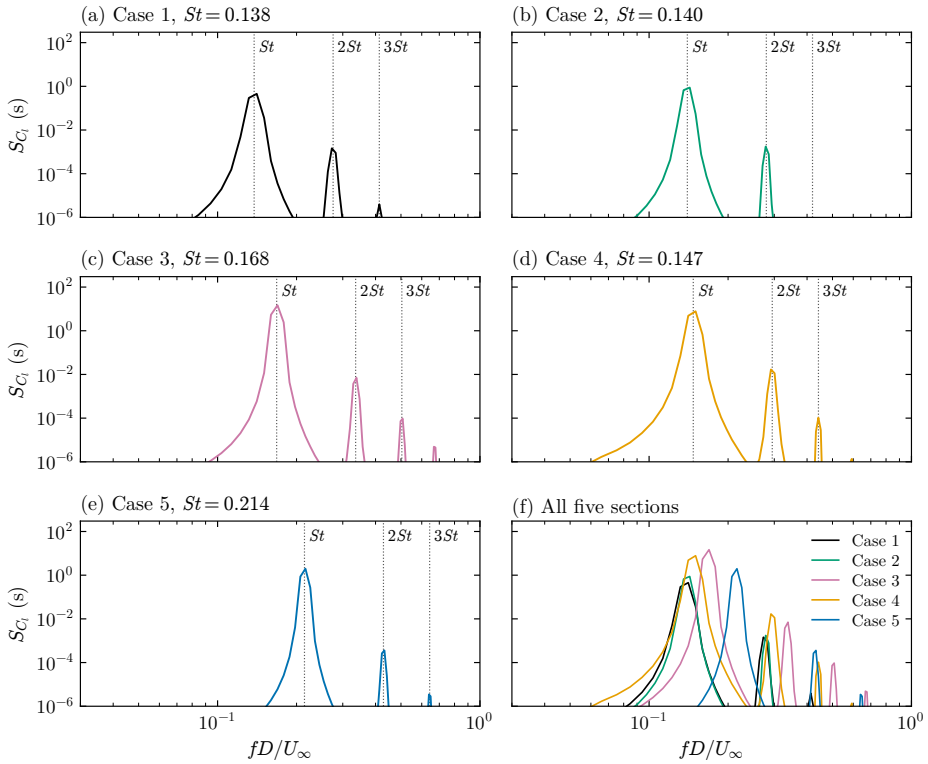


Fig. 23 Welch spectra of the lift coefficient for the five sections on M2, using the windows in Table 5. Each spectrum uses five Hann-windowed segments with 50% overlap. Segment duration is about 40 s, or 50 s for Case 2. Dotted lines show the Strouhal number from Table 5 and its second and third harmonics. Panel (f) shows all five spectra together

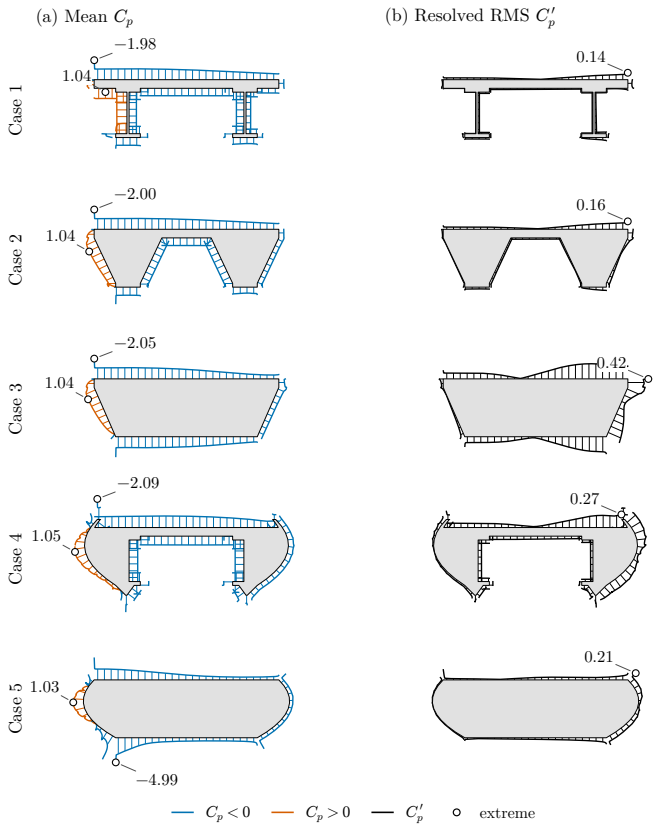


Fig. 24 Mean (a) and root-mean-square (b) surface-pressure coefficients for the five sections on M2 over 40–160 s; Case 5 uses a maximum Courant number of 1. Values are drawn along the outward normal. The mean coefficient C_P is relative to the outlet pressure and uses a display scale of 1.6 m per unit $|C_P|$. Blue shows $C_P < 0$, and orange shows $C_P > 0$. The scale for C'_p is 8 m per unit. Circles show extreme values. The plotted mean is clipped at $|C_P| = 2.5$, affecting only three faces at the windward lower knuckle of Case 5, where C_P reaches -4.99. The coefficient C'_p contains only resolved fluctuations. The Case 2 pressure field uses 40–160 s, unlike the 100–250 s force window in Table 5

References

[1] Y. Kubo, K. Kimura, K. Sadashima, Y. Okamoto, E. Yamaguchi, K. Kato, Aerodynamic performance of improved shallow π shape bridge deck. J. Wind Eng. Ind. Aerodyn. **90**, 2113–2125 (2002). https://doi.org/10.1016/s0167-6105(02)00328-8

[2] H. Bai, R. Li, G. Xu, A. Kareem, Aerodynamic performance of Π-shaped composite deck cable-stayed bridges including VIV mitigation measures. J. Wind Eng. Ind. Aerodyn. **208**, 104451 (2021). https://doi.org/10.1016/j.jweia.2020.104451

[3] J. Li, P. Wu, J. Hao, H. Pan, Experimental and numerical studies on the two "Lock-in" regions characteristic of vertical vortex-induced vibration of Π-shaped composite bridge deck. J. Wind Eng. Ind. Aerodyn. **228**, 105122 (2022). https://doi.org/10.1016/j.jweia.2022.105122

[4] A. Larsen, J.H. Walther, Aeroelastic analysis of bridge girder sections based on discrete vortex simulations. J. Wind Eng. Ind. Aerodyn. **67–68**, 253–265 (1997). https://doi.org/10.1016/s0167-6105(97)00077-9

[5] M.W. Sarwar, T. Ishihara, Numerical study on suppression of vortex-induced vibrations of box girder bridge section by aerodynamic countermeasures. J. Wind Eng. Ind. Aerodyn. **98**, 701–711 (2010). https://doi.org/10.1016/j.jweia.2010.06.001

[6] L. Huang, Q. Wang, H. Liao, Effective wind fairing combination aerodynamic measures against vortex-induced vibrations of Π-shaped composite bridge decks. Phys. Fluids **37**, 037174 (2025). https://doi.org/10.1063/5.0262948

[7] W.A. Mair, Reduction of base drag by boat-tailed afterbodies in low-speed flow. Aeronaut. Q. **20**, 307–320 (1969). https://doi.org/10.1017/S0001925900005126

[8] A. Mariotti, G. Buresti, M.V. Salvetti, Separation delay through contoured transverse grooves on a 2D boat-tailed bluff body: Effects on drag reduction and wake flow features. Eur. J. Mech. B/Fluids **74**, 351–362 (2019). https://doi.org/10.1016/j.euromechflu.2018.09.009

[9] S. Tesfaye, I. Kavrakov, G. Morgenthal, Numerical investigation of the nonlinear interaction between the sinusoidal motion-induced and gust-induced forces acting on bridge decks. J. Fluids Struct. **113**, 103680 (2022). https://doi.org/10.1016/j.jfluidstructs.2022.103680

[10] R. Scotta, M. Lazzari, E. Stecca, J. Cotela, R. Rossi, Numerical wind tunnel for aerodynamic and aeroelastic characterization of bridge deck sections. Comput. Struct. **167**, 96–114 (2016). https://doi.org/10.1016/j.compstruc.2016.01.012

[11] I. Kusano, J.B. Jakobsen, J.Th. Snæbjörnsson, CFD simulations of a suspension bridge deck for different deck shapes with railings and vortex mitigating devices. IOP Conf. Ser. Mater. Sci. Eng. **700**, 012003 (2019). https://doi.org/10.1088/1757-899x/700/1/012003

[12] B. Nicese, A.M. Marra, G. Bartoli, C. Mannini, VIV mechanisms of a non-streamlined bridge deck equipped with traffic barriers. J. Fluids Struct. **132**, 104195 (2025). https://doi.org/10.1016/j.jfluidstructs.2024.104195

[13] E. López-Nuñez, M. Ogueta-Gutiérrez, O. Gómez-Ortega, R. Manzanares-Bercial, E. Roibás-Millán, S. Franchini, Effect of wind barriers on the aeroelastic instabilities of a hinged-deck cross-section cable-stayed bridge. Eng. Struct. **287**, 116112 (2023). https://doi.org/10.1016/j.engstruct.2023.116112

[14] G. Yao, Y. Chen, Y. Yang, Y. Zheng, L. Wu, H. Du, Research on mechanism of vortex-induced vibration railing effect of double-deck large-span suspension bridge. Appl. Sci. **13**, 9314 (2023). https://doi.org/10.3390/app13169314

[15] T. Ei, K. Noguchi, H. Matsumiya, S. Hara, T. Yagi, Effects of discrete fairings on torsional aerodynamic vibrations of a bridge deck. J. Wind Eng. Ind. Aerodyn. **268**, 106272 (2026). https://doi.org/10.1016/j.jweia.2025.106272

[16] J. Zheng, G. Fang, Z. Wang, L. Zhao, Y. Ge, Shape optimization of closed-box girder considering dynamic and aerodynamic effects on flutter: A CFD-enabled and Kriging surrogate-based strategy. Eng. Appl. Comput. Fluid Mech. **17**, 2191693 (2023). https://doi.org/10.1080/19942060.2023.2191693

[17] T. Abbas, I. Kavrakov, G. Morgenthal, T. Lahmer, Framework for a simulation-based aerodynamic shape optimization of bridge decks for different limit state phenomena. arXiv:2203.14414 (2022). https://doi.org/10.48550/arXiv.2203.14414

[18] M. Cid Montoya, H. Bai, M. Ye, Shaping bridge decks for VIV mitigation: A wind tunnel data-driven adaptive surrogate-based optimization method. J. Wind Eng. Ind. Aerodyn. **242**, 105568 (2023). https://doi.org/10.1016/j.jweia.2023.105568

[19] S. Verma, M. Cid Montoya, A. Mishra, Shape- and frequency-dependent self-excited forces emulation for the aero-structural design of bluff deck bridges. J. Wind Eng. Ind. Aerodyn. **252**, 105769 (2024). https://doi.org/10.1016/j.jweia.2024.105769

[20] S. Verma, M. Cid Montoya, A. Mishra, Aero-structural design of bridge decks under synoptic and non-synoptic winds via aeroelastic surrogates comprising shape, reduced velocity, and mean angle of attack. J. Wind Eng. Ind. Aerodyn. **265**, 106133 (2025). https://doi.org/10.1016/j.jweia.2025.106133

[21] M.E.O. Elhassan, L.-D. Zhu, W. Alhaddad, Z. Tan, Surrogate modeling for aerodynamic static instability of central-slotted box decks using machine learning approaches. Adv. Struct. Eng. **27**, 2271–2288 (2024). https://doi.org/10.1177/13694332241267901

[22] H. Liu, B. Chen, Y. Han, P. Hu, C.S. Cai, L. Wang, Aerodynamic shape optimization of Π-shaped composite bridge deck with wind fairing based on WOA-GRNN surrogate model. China J. Highw. Transp. **36**, 76–86 (2023). https://doi.org/10.19721/j.cnki.1001-7372.2023.08.008

[23] A. Larsen, A. Wall, Shaping of bridge box girders to avoid vortex shedding response. J. Wind Eng. Ind. Aerodyn. **104–106**, 159–165 (2012). https://doi.org/10.1016/j.jweia.2012.04.018

[24] F.R. Menter, Two-equation eddy-viscosity turbulence models for engineering applications. AIAA J. **32**, 1598–1605 (1994). https://doi.org/10.2514/3.12149

[25] F. Nieto, D.M. Hargreaves, J.S. Owen, S. Hernández, On the applicability of 2D URANS and SST k–ω turbulence model to the fluid–structure interaction of rectangular cylinders. Eng. Appl. Comput. Fluid Mech. **9**, 157–173 (2015). https://doi.org/10.1080/19942060.2015.1004817

[26] M. Đuranović, A. Dempsey, C. Meskell, Computational fluid dynamics as an early aerodynamic design tool for a typical bluff bridge deck. Proc. Inst. Civ. Eng. Bridge Eng. **179**, 127–152 (2026). https://doi.org/10.1680/jbren.24.00023

[27] M.N. Haque, H. Katsuchi, H. Yamada, M. Nishio, Flow field analysis of a pentagonal-shaped bridge deck by unsteady RANS. Eng. Appl. Comput. Fluid Mech. **10**, 1–16 (2016). https://doi.org/10.1080/19942060.2015.1099569

[28] A. Chiarini, M. Quadrio, The importance of corner sharpness in the BARC test case: A numerical study. Wind Struct. **34**, 43–58 (2022). https://doi.org/10.12989/was.2022.34.1.043

[29] H.-Y. Li, Y.-L. Xu, H.-L. Liao, L. Huang, Q. Wang, Digital twin-driven method for determining wind force coefficients of a bridge deck section. Eng. Appl. Comput. Fluid Mech. **19**, 2501389 (2025). https://doi.org/10.1080/19942060.2025.2501389

[30] A.J. Álvarez, F. Nieto, Vortex induced vibration analysis of a twin-box bridge deck by means of 3D LES simulations. J. Wind Eng. Ind. Aerodyn. **258**, 106015 (2025). https://doi.org/10.1016/j.jweia.2025.106015

[31] L. Bruno, D. Oberto, Effects of cell quality in grid boundary layer on the simulated flow around a square cylinder. Comput. Fluids **238**, 105351 (2022). https://doi.org/10.1016/j.compfluid.2022.105351

[32] D. Rocchi, T. Argentini, M. Sbrosi, Pressure distribution and global forces on a bridge deck section: Experimental and CFD analysis of static aerodynamic forces. J. Bridge Eng. **20**, 04014097 (2015). https://doi.org/10.1061/(asce)be.1943-5592.0000695

[33] A. Larsen, Aerodynamic aspects of the final design of the 1624 m suspension bridge across the Great Belt. J. Wind Eng. Ind. Aerodyn. **48**, 261–285 (1993). https://doi.org/10.1016/0167-6105(93)90141-a

[34] G. Schewe, A. Larsen, Reynolds number effects in the flow around a bluff bridge deck cross section. J. Wind Eng. Ind. Aerodyn. **74–76**, 829–838 (1998). https://doi.org/10.1016/s0167-6105(98)00075-0

[35] L. Bruno, M.V. Salvetti, F. Ricciardelli, Benchmark on the aerodynamics of a rectangular 5:1 cylinder: An overview after the first four years of activity. J. Wind Eng. Ind. Aerodyn. **126**, 87–106 (2014). https://doi.org/10.1016/j.jweia.2014.01.005

[36] F.R. Menter, M. Kuntz, R. Langtry, Ten years of industrial experience with the SST turbulence model. In *Turbulence, Heat and Mass Transfer 4*, ed. by K. Hanjalić, Y. Nagano, M. Tummers (Begell House, 2003), pp. 625–632.

[37] C. Mannini, A. Šoda, G. Schewe, Unsteady RANS modelling of flow past a rectangular cylinder: Investigation of Reynolds number effects. Comput. Fluids **39**, 1609–1624 (2010). https://doi.org/10.1016/j.compfluid.2010.05.014

[38] G. Iaccarino, A. Ooi, P.A. Durbin, M. Behnia, Reynolds averaged simulation of unsteady separated flow. Int. J. Heat Fluid Flow **24**, 147–156 (2003). https://doi.org/10.1016/s0142-727x(02)00210-2

[39] P.R. Spalart, C.L. Rumsey, Effective inflow conditions for turbulence models in aerodynamic calculations. AIAA J. **45**, 2544–2553 (2007). https://doi.org/10.2514/1.29373

[40] P.D. Welch, The use of fast Fourier transform for the estimation of power spectra: A method based on time averaging over short, modified periodograms. IEEE Trans. Audio Electroacoust. **15**, 70–73 (1967). https://doi.org/10.1109/tau.1967.1161901

[41] A. Roshko, Perspectives on bluff body aerodynamics. J. Wind Eng. Ind. Aerodyn. **49**, 79–100 (1993). https://doi.org/10.1016/0167-6105(93)90007-b

[42] H.G. Weller, G. Tabor, H. Jasak, C. Fureby, A tensorial approach to computational continuum mechanics using object-oriented techniques. Comput. Phys. **12**, 620–631 (1998). https://doi.org/10.1063/1.168744

[43] J. Franke, A. Hellsten, H. Schlünzen, B. Carissimo (eds.), *Best practice guideline for the CFD simulation of flows in the urban environment*. COST Action 732 (COST European Cooperation in Science and Technology, 2007).

[44] B.E. Launder, D.B. Spalding, The numerical computation of turbulent flows. Comput. Methods Appl. Mech. Eng. **3**, 269–289 (1974). https://doi.org/10.1016/0045-7825(74)90029-2

[45] I.B. Celik, U. Ghia, P.J. Roache, C.J. Freitas, H. Coleman, P.E. Raad, Procedure for estimation and reporting of uncertainty due to discretization in CFD applications. J. Fluids Eng. **130**, 078001 (2008). https://doi.org/10.1115/1.2960953

[46] AIAA Computational Fluid Dynamics Committee, *Guide for the verification and validation of computational fluid dynamics simulations*, AIAA G-077-1998(2002) (American Institute of Aeronautics and Astronautics, Reston, VA, 1998). https://doi.org/10.2514/4.472855

[47] W.L. Oberkampf, T.G. Trucano, Verification and validation in computational fluid dynamics. Prog. Aerosp. Sci. **38**, 209–272 (2002). https://doi.org/10.1016/s0376-0421(02)00005-2

[48] A. Roshko, *On the drag and shedding frequency of two-dimensional bluff bodies* (NACA Technical Note 3169). National Advisory Committee for Aeronautics (1954). https://ntrs.nasa.gov/citations/19930083869

[49] L. Bruno, N. Coste, D. Fransos, Simulated flow around a rectangular 5:1 cylinder: Spanwise discretisation effects and emerging flow features. J. Wind Eng. Ind. Aerodyn. **104–106**, 203–215 (2012). https://doi.org/10.1016/j.jweia.2012.03.018

[50] C. Mannini, A. Šoda, G. Schewe, Numerical investigation on the three-dimensional unsteady flow past a 5:1 rectangular cylinder. J. Wind Eng. Ind. Aerodyn. **99**, 469–482 (2011). https://doi.org/10.1016/j.jweia.2010.12.016

[51] Y. Nakamura, Y. Ohya, The effects of turbulence on the mean flow past two-dimensional rectangular cylinders. J. Fluid Mech. **149**, 255–273 (1984). https://doi.org/10.1017/s0022112084002640

[52] Highways England, *CD 377 Requirements for road restraint systems* (Revision 4, 28 January 2021; Design Manual for Roads and Bridges). Highways England (2021).

[53] S.V. Patankar, D.B. Spalding, A calculation procedure for heat, mass and momentum transfer in three-dimensional parabolic flows. Int. J. Heat Mass Transf. **15**, 1787–1806 (1972). https://doi.org/10.1016/0017-9310(72)90054-3

[54] T.-H. Shih, W.W. Liou, A. Shabbir, Z. Yang, J. Zhu, A new k–ε eddy viscosity model for high Reynolds number turbulent flows. Comput. Fluids **24**, 227–238 (1995). https://doi.org/10.1016/0045-7930(94)00032-t

[55] K. Shimada, T. Ishihara, Application of a modified k–ε model to the prediction of aerodynamic characteristics of rectangular cross-section cylinders. J. Fluids Struct. **16**, 465–485 (2002). https://doi.org/10.1006/jfls.2001.0433

[56] G. Schewe, Reynolds-number-effects in flow around a rectangular cylinder with aspect ratio 1:5. J. Fluids Struct. **39**, 15–26 (2013). https://doi.org/10.1016/j.jfluidstructs.2013.02.013

[57] D. Rockwell, E. Naudascher, Review: Self-sustaining oscillations of flow past cavities. J. Fluids Eng. **100**, 152–165 (1978). https://doi.org/10.1115/1.3448624